

# Remote sensing, planform, and sedimentological analysis of the Plain of Tineh, Egypt for the remains of the defunct Pelusiac River

---

A Thesis  
Presented to  
the faculty of the Department of Earth and Atmospheric Sciences  
University of Houston

---

In Partial Fulfillment  
of the Requirements for the Degree  
Masters of Science

---

By:  
Jessica Quintanar  
May 2013

# Remote sensing, planform, and sedimentological analysis of the Plain of Tineh, Egypt for the remains of the defunct Pelusiac River

---

Jessica Quintanar

APPROVED:

---

Dr. Shuhab Khan, Advisor

---

Dr. Janok P. Bhattacharya, Committee  
Member

---

Dr. Allison Kennedy Thurmond,  
Committee Member

---

Dr. Dan Wells, Interim Dean, College  
of Natural Sciences and Mathematics

## **DEDICATION**

I would like to thank and dedicate this work to my family. My parents Francisco and Maria Quintanar have always supported my efforts to extend my education in whatever direction I happened to follow regardless of how farfetched it may have seemed at the time. I would also like to dedicate this to my brother Tony for helping to keep me grounded while managing to encourage me to strive forward.

March 2013

## **ACKNOWLEDGEMENTS**

I would like to extend my thanks to my committee members, Shuhab Khan, Janok Bhattacharya, and Allison Kennedy Thurmond for their aid and support throughout the progression of this project. In particular, I would like to especially thank Dr. Khan for his unending patience and support, not only academic but as a true advisor. He opened the doors to a wider world throughout my studies by encouraging me to question, yet candidly answered any questions posed to him regardless of their apparent merit. Thank you.

I would also like to thank our native Egyptian guides and colleagues, Dr. Zalat and particularly Dr. Sobhy, whose guidance was invaluable throughout the completion of the field work. Also Dr. Julia Wellner at the University of Houston for her aid with laser particle analysis, Dr. Rosalie Maddocks for her brief, yet enlightening lecture on mollusk identification, and Dr. William Dupre for answering many lengthy and sometimes convoluted questions. Lastly, I would like to give a special thanks to the GeoRS team at the University of Houston; Zheng Huang, Ayca Karacay, Yahaya Abubakar, Ismail Abir, Kivac Biber, Kevin Schmidt, Xu Han, and Unal Okyay. I couldn't think of another group I would so enjoy spending time with in such a small room! Thanks.

March 2013

Remote sensing, planform, and sedimentological  
analysis of the Plain of Tineh, Egypt for the  
remains of the defunct Pelusiac River

---

An Abstract of a Thesis

Presented to

the faculty of the Department of Earth and Atmospheric Sciences

University of Houston

---

In Partial Fulfillment

of the Requirements for the Degree

Masters of Science

---

By:

Jessica Quintanar

May 2013

## **ABSTRACT**

The Pelusiac Branch was a distributary river in the Nile Delta that split off the main trunk of the Nile River as it flowed toward the Mediterranean. At approximately 25 A.D., it was choked by sand and silt deposits from prograding beach accretion processes. The lower course of the river and its bifurcation point from the trunk of the Nile, have been hypothesized based on ancient texts and maps, as well as previous research with inconsistent results. Previous studies partly mapped the lower course of the Pelusiac River in the Plain of Tineh, east of the Suez Canal but, rapid urbanization related to the inauguration of the Peace Canal mega-irrigation project has covered any trace of the linear feature reported by previous studies.

Remote sensing methods were employed in this study to locate and accurately map the course of the defunct Pelusiac River within the Plain of Tineh. Multispectral remote sensing in the form of GeoEye-1 and Landsat, and radar datasets including the TerraSAR-X, PALSAR, and RADARSAT platforms were implemented. Remote sensing analysis identified a linear feature that is 135m wide at its maximum and approximately 13km long. It extends from the Pelusium ruins to the Suez Canal, just north of the Peace Canal. The remotely located linear feature corresponds to the path of the Pelusiac River during Roman times. Planform geomorphology was applied to determine the hydrological regime and paleo-discharge of the river prior to becoming defunct. Planform analysis derived a bankfull paleo-discharge value of  $\sim 5700 \text{ m}^3 \text{ s}^{-1}$  and an average discharge of  $650 \text{ m}^3 \text{ s}^{-1}$  using the reach average for the interpreted Pelusiac River. The

derived values show a river distributary similar in discharge to the modern dammed Damietta River. Field work completed in April 2012 derived four sedimentary lithofacies of the upper formation on the plain. Diatom and fossil mollusk samples were also identified and support coastal beach and lagoonal environments of deposition. Measured sections and a transect oblique to the shoreline, were also constructed to portray the paleogeography of the Mediterranean coastline in the Plain of Tineh at ~25 A.D and indicate that the sampled study area is the downdrift margin of an asymmetric delta with barrier lagoon systems.

**TABLE OF CONTENTS**

**ACKNOWLEDGEMENTS ..... iii**

**ABSTRACT..... VI**

**TABLE OF CONTENTS ..... VIII**

**LIST OF FIGURES .....X**

**LIST OF TABLES ..... XIV**

**Chapter 1: Introduction and Background.....1**

**1.1The Nile Delta.....2**

**1.2 Defunct Distributaries and the Pelusiac Branch.....4**

**1.3 Previous Studies in the Plain of Tineh.....8**

**1.4 Objectives.....10**

**1.5 Geologic Setting.....11**

**1.6 Study Area.....14**

**Chapter 2: Remote Sensing.....17**

**2.1 Remote Sensing Analysis.....18**

**2.1.1 Remote Sensing Methods.....18**

**2.1.2 Multispectral Remote Sensing Results.....20**

**2.1.3 RADAR Results.....31**

**2.1.4 Remote Sensing Interpretations.....35**

**2.2 Planform ANALYSIS.....41**

**2.2.1 Planform Geometry.....41**

**2.2.2 Planform Measurement Methods.....44**

**2.2.3 Calculated Planform Results.....45**

**2.3 Discussion.....54**

**Chapter 3: Stratigraphy and Sedimentology .....60**

<b>3.1 Methods.....</b>	<b>61</b>
<b>3.2 Stratigraphic Analysis.....</b>	<b>63</b>
<b>3.3 Lithofacies Analysis.....</b>	<b>87</b>
<b>3.4 Bivariate Plots for Grain Size Analysis.....</b>	<b>95</b>
<b>3.5 Shoreline Oblique Transect.....</b>	<b>99</b>
<b>3.6 Discussion.....</b>	<b>100</b>
<b>Chapter 4: Conclusion.....</b>	<b>109</b>
<b>REFERENCES .....</b>	<b>112</b>
<b>APPENDIX .....</b>	<b>117</b>

## LIST OF FIGURES

<b>Figure 1.1 The Nile Delta as observed from satellite imagery in 2010.....</b>	<b>3</b>
<b>Figure 1.2 The Nile River Basin. The Nile River flows through 10 countries for over 6,650 km before discharging into the Mediterranean Sea.....</b>	<b>5</b>
<b>Figure 1.3 Map of the Nile Delta showing past and present river branches during the last 10,000 years (Said, 1981) .....</b>	<b>7</b>
<b>Figure 1.4 Previous studies mapped Pelusiac river avulsion in the Plain of Tineh.....</b>	<b>9</b>
<b>Figure 1.5 Quaternary formations of the Nile Delta during the Quaternary (Modified after Rizzini et al. 1978 and Said, 1981).....</b>	<b>10</b>
<b>Figure 1.6 Geologic ages for sediments in the Plain of Tineh .....</b>	<b>12</b>
<b>Figure 1.7 The main structural elements in the Plain of Tineh, northeast Nile Delta Egypt. 13</b>	
<b>Figure 1.8 Map of the study area in relation to the Nile Delta in Egypt.....</b>	<b>14</b>
<b>Figure 1.9 Collected GPS points in the field for the northeastern segment of the study area .....</b>	<b>15</b>
<b>Figure 2.1 Plain of Tineh showing major feature divisions including the extent of the strandplain, delta plain, beach and desert.....</b>	<b>21</b>
<b>Figure 2.2 Landsat TM in Band 3 Grayscale showing location and zoomed-in image of a linear feature extending from Tel el Farama in the Plain of Tineh, Nile Delta Egypt. Landsat TM Band 3 Grayscale. Data acquired November 11, 1998 .....</b>	<b>24</b>
<b>Figure 2.3 A: A linear feature was observed in the Nile Delta east of the Suez Canal that was interpreted as the lower end of the Roman Pelusiac Branch and extends for approximately 20km. Landsat TM, RGB 3-2-1 Data acquired Sept. 20, 1984 .....</b>	<b>25</b>
<b>Figure 2.4 The Plain of Tineh in Landsat TM portrayed in band combination 465 and an equalization filter. The combination helps to denote differences in the observable lithology of the plain .....</b>	<b>29</b>

<b>Figure 2.5 A near pristine Plain of Tineh is shown with labeled major geological features previously unobserved in later datasets. Multi-Spectral Scanner 1975 Band 4 Grayscale .....</b>	<b>30</b>
<b>Figure 2.6 PALSAR image subset of the Plain of Tineh .....</b>	<b>32</b>
<b>Figure 2.7 Radarsat- HH polarization of the Plain of Tineh, Egypt .....</b>	<b>33</b>
<b>Figure 2.8 The Pelusium ruin area in the Plain of Tineh as observed from the high –resolution TerraSAR-X satellite .....</b>	<b>35</b>
<b>Figure 2.9 Interpreted fluvial geomorphology for the Pelusiac River in the Plain of Tineh. ....</b>	<b>38</b>
<b>Figure 2.10 Types of principal river patterns seen in planform view .....</b>	<b>42</b>
<b>Figure 2.11 An idealized meander in planform view.....</b>	<b>43</b>
<b>Figure 2.12 Overview of the study area showing chosen meander belts.....</b>	<b>46</b>
<b>Figure 2.13 The shallow water table as observed in the field .....</b>	<b>52</b>
<b>Figure 3.1 Location of measured section CHA. The section was measured at the termination of an exposed length of an irrigation canal flowing west to east in the Plain of Tineh .....</b>	<b>64</b>
<b>Figure 3.2 Stratigraphic columnar section for the location CHA along an irrigation canal running parallel to the Al Kantara Shark- Al Arish road .....</b>	<b>65</b>
<b>Figure 3.3 Field photographs taken at section CHA .....</b>	<b>66</b>
<b>Figure 3.4 Particle size distribution by volume is shown graphically for sample CHA-1 and CHA-2. Statistical derivations including weighted means and graphic mean, standard deviation and skewness and kurtosis values displayed beneath their respective graphs.....</b>	<b>67</b>
<b>Figure 3.5 Location of measured sections CHB and CHC along an irrigation canal running almost parallel to the Al Kantara Shark- Al Arish Road.....</b>	<b>69</b>
<b>Figure 3.6 A stratigraphic section was created for the measured section in location CHB. The section contains Facies B1 and B2 which intergrades in the middle of the section .....</b>	<b>70</b>

<b>Figure 3.7</b>	<b>Field photographs of section CHB .....</b>	<b>72</b>
<b>Figure 3.8</b>	<b>Gastropod and bivalve samples collected from fossiliferous sands in the measured sections along an irrigation canal parallel to the Mediterranean shoreline during 25 AD .....</b>	<b>74</b>
<b>Figure 3.9</b>	<b>Stratigraphic columnar section for the location CHC data collected in the field. The section shows the abrupt change in facies between sandy Facies C and the shelly silts of Facies D.....</b>	<b>76</b>
<b>Figure 3.10</b>	<b>Field photographs of section CHC .....</b>	<b>78</b>
<b>Figure 3.11</b>	<b>Location of the westernmost section CHD along an irrigation canal parallel to Al Kantara Shark- Al Arish Road .....</b>	<b>79</b>
<b>Figure 3.12</b>	<b>Constructed stratigraphic section of measured location CHD. The section consisted of beds belonging to Facies D of lagoon deposits .....</b>	<b>81</b>
<b>Figure 3.13</b>	<b>Field photographs of section CHD .....</b>	<b>82</b>
<b>Figure 3.14</b>	<b>Three different taxa of diatoms commonly found within samples of section CHD .....</b>	<b>83</b>
<b>Figure 3.15</b>	<b>Location of TEF samples in relation to measured sections CHA-CHD near the Pelusium Ruins in the northeastern Plain of Tineh .....</b>	<b>86</b>
<b>Figure 3.16</b>	<b>Field photographs taken at location TEF .....</b>	<b>87</b>
<b>Figure 3.17</b>	<b>Convolute bedding in a sandy bed of Facies C .....</b>	<b>92</b>
<b>Figure 3.18</b>	<b>Foreshore laminated sands of Facies C showing parallel lamination, textural variation, and heavy mineral laminae in well-sorted, fine- to medium-grained sand .....</b>	<b>94</b>
<b>Figure 3.19</b>	<b>Transition between Facies C and Facies D that were interpreted as beachface and lagoon deposits, respectively .....</b>	<b>95</b>
<b>Figure 3.20</b>	<b>Bivariate plots created to describe sedimentological characteristics of the interpreted environments of deposition including tidal flat, beachface, and lagoon using the collected samples from the measured sections .....</b>	<b>97</b>
<b>Figure 3.21</b>	<b>Shoreline parallel transect observed along the interpreted Roman coastline of the Mediterranean around 25 AD .....</b>	<b>102</b>

**Figure 3.22 3D Block diagram of an asymmetric wave-influenced delta ....104**

**Figure 3.23 The interpreted progradational shoreline sedimentary sequence for the study area is shown with the location of the measured sections .....105**

**Figure 3.24 Sketch showing the Pelusiac distributary river deflecting east at the asymmetric delta due to decreasing fluvial sediment discharge and a strong net longshore current .....106**

**Figure 3.25 Sketch showing the paleogeography of the Plain of Tineh after the Pelusiac Branch mouth silted up and the river went defunct .....108**

## LIST OF TABLES

<b>Table 2.1 Channel dimension estimations for the Pelusiac paleomeanders from remote sensing analysis .....</b>	<b>48</b>
<b>Table 2.2 Channel dimension estimations for ten meanders chosen from the terminal Damietta distributary branch and measured at their 2012 dimensions for comparison to the Pelusiac paleomeanders. ....</b>	<b>49</b>
<b>Table 2.3 The measured and calculated planform characters for the chosen Damietta meanders in 2012 and the Pelusiac river paleomeanders from Landsat imagery. Parameter values are averaged based on measurements at various meanders from Tables 2.1 and 2.2 .....</b>	<b>51</b>
<b>Table 2.4 Paleo-discharge was calculated for the Pelusiac paleomeanders and the Damietta meanders chosen for comparison of results. The discharge estimates for both locations are presented in <math>m^3s^{-1}</math> .....</b>	<b>52</b>
<b>Table 2.5 Discharge estimates for the present Damietta and defunct Pelusiac paleomeanders using reach average channel dimensions ....</b>	<b>53</b>
<b>Table 3.1 Facies names, their respective lithologies and present sedimentary structures, if any, present in the study area .....</b>	<b>89</b>

# **Chapter 1: Introduction and Background**

The Nile Delta in Egypt is traversed by the Nile Rosetta and Damietta distributaries as they flow north to the Mediterranean Sea. During the Quaternary, at least seven distributaries have been acknowledged as consecutively flowing, major branches of the Nile (Abdel-Kader, 1982). The demise of the other distributaries in the delta is not well understood, but has been theorized to be a combination of tectonics, climate, and human intervention (Said, 1981). The importance of the river and fertile delta, in the otherwise arid country, explain why the population concentration along the Nile River's banks has made the waterway and its distributaries a focal point for archeology, hydrology and geologic studies (Fig. 1.1) (Frihy, 1996; Nixon, 2004). Identification of the river's defunct distributaries will further geologic understanding of one of the most densely populated agricultural areas in the world. Their course can also be applied as a focus for future archeological studies in the region. Recently, rapid growth and urbanization in Egypt, particularly the northeastern Nile delta, continue to modify the landscape of the delta plain. Identification and further study of the course of the defunct Pelusiac Branch is a priority, as land reclamation and urbanization continues to expand into the Sinai Peninsula east of the Suez Canal.

## **1.1 The Nile Delta**

The Nile River is the longest river in the world, flowing 6,829 km from its headwaters in the south of Africa to the Mediterranean Sea in the north (Figure 1.2). The river is fed by the Blue and White Nile rivers and drains an area of approximately

## THE NILE DELTA



Figure 1.1: The Nile Delta located in the north of Egypt is shown from satellite imagery. The Nile River is the most important fresh water source in Egypt. The Nile bifurcates after passing through the city of Cairo to the south of the delta. The two main distributary branches empty into the Mediterranean Sea to the north at the Rosetta and Damietta promontories, respectively. Port Said, the end point for the Suez Canal is located in the north-easternmost part of the delta. (Map created using ESRI ArcGIS 10 from GeoEye imagery.)

3,400,000 km<sup>2</sup> (Coleman, 1981; Wright and Coleman, 1973). The Nile enters Egypt at its southern border near Wadi Halfa and flows due north before bifurcating north of Cairo into the Rosetta and Damietta branches.

The Nile Delta area begins near Cairo and extends both west and east as it forms the Greek letter delta ( $\Delta$ ) shape that is bounded by the Mediterranean Sea. The delta is large, with an area of over 22,000 km<sup>2</sup> (Wright and Coleman, 1973). The Nile Delta is a wave-dominated delta system as classified by Galloway (1975). Although the effects of tide and river influence are minimal today, the influence of the Nile River was greater in the past. The changes are due in large part to changing climate, although some is accredited to increasing human modification of the river. The damming of the Nile at the Aswan High Dam in Aswan, Egypt has severely decreased the discharge of sediment reaching the Mediterranean. Demands for water for irrigation in the manufacturing and agricultural sector, has further diminished the flow of Nile water into the sea. Sediment compaction, coastal loading and high rates of subsidence and low minimal sediment discharge suggest a decline ushering the destructional phase for the delta (Stanley, 1988).

## **1.2 Defunct Distributaries and the Pelusiac Branch**

The precursor to the modern Nile River, the Neo-Nile, flowed from the Late Pleistocene into the Holocene. The Neo-Nile was a larger river in comparison to the modern Nile, feeding at least seven distributaries within the delta. Historical texts including “The Histories” by Herodotus in the 5th century B.C. have referenced the

# THE NILE RIVER



Figure 1.2: The Nile River flows through Ethiopia, Sudan, Egypt, Uganda, Democratic Republic of the Congo, Kenya, Tanzania, Rwanda, Burundi and South Sudan for over 6,650 km before emptying into the Mediterranean Sea. Map created using ESRI ArcGIS 10.

existence of these seven major distributaries in the Nile Delta, including the easternmost Pelusiac Branch (Abdel-Kader, 1982).

Figure 1.3 shows a generalized flow path for seven paleochannels in the Nile Delta. From the west, they are the Canopic, Bolbitine (modern Rosetta), Sebbenytic, Pathmytic (modern Damietta), Mendesian, Tanitic, and Pelusiac (Baynes, 1988). Of the seven branches paleochannels,, only the Damietta and Rosetta presently flow to the Mediterranean Sea. The other branches have become defunct or deteriorated into the network of irrigation canals in the delta (Baynes, 1988).

The defunct Pelusiac Branch was an important navigable waterway that extended trade to the east. (Sneh and Weissbrod, 1973). As late as the 12th century, Tell el Farama (ancient Pelusium), located on the mouth of the Pelusiac Branch, was considered the “gateway to the east” since trade heading to the Asian kingdoms passed through the city on its way to Sinai and Asia (Sneh and Weissbrod, 1973). It flowed northeast past the modern-day Suez Canal, into the Mediterranean. The shoreline retreated during the time of the Neo-Nile and various avulsions took place in the Plain of Tineh before it went defunct (Stanley et al., 2008).

Longshore accretion processes created the present day strandplain on the northeastern side of the Nile Delta and are credited with silting-up the Pelusiac River mouth. Carbon 14 dating of mollusks collected in the youngest ridge within the

### Nile Delta- Defunct Distributaries of the Nile

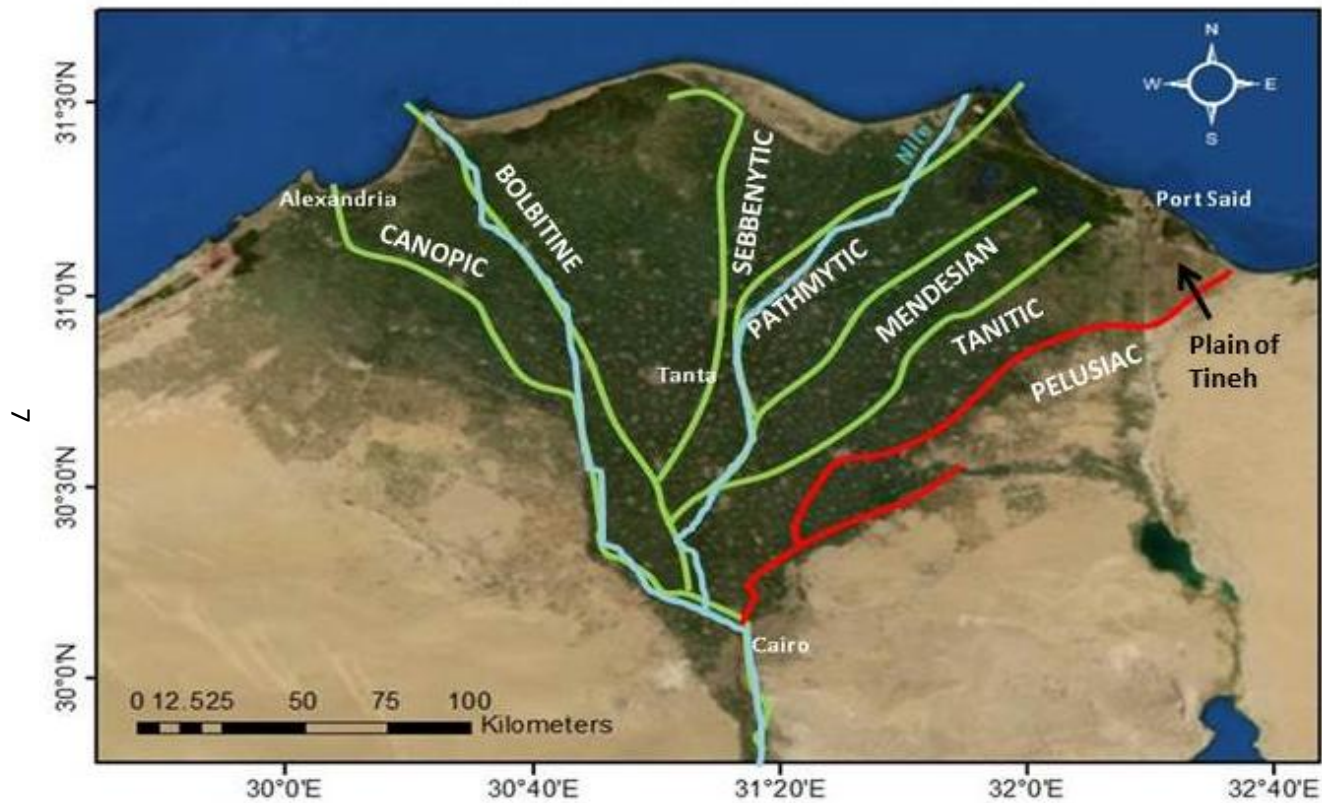


Figure 1.3: Map of the Nile Delta showing past and present river branches during the Quaternary (in green and red). Only the modern Rosetta and Damietta branches reach the Mediterranean today (in light blue). The Pelusiac is the easternmost branch and emptied into the Mediterranean past the modern day Pelusium ruins. It is shown in red above. River path information after Said (1981). Background map created using ESRI ArcGIS 10.

strandplain, suggest the river ceased flow around 25 A.D. (Sneh and Weissbrod, 1973).

Goodfriend and Stanley (1999) suggested that the Pelusiac may have continued to flow as late as mid-800 A.D., but ruins older than Roman design have not been found in the strandplain area.

### **1.3 Previous studies in Plain of Tineh**

Sneh and Weissbrod (1973) mapped the lower course of the Pelusiac by a combination of field work and aerial photography. They observed a depression 80-100m wide and several centimeters in depth across the deltaic plain south of the strandplain. The depression was interpreted as the main branch of the Pelusiac. Figure 1.4 illustrates the location of this and other river flow paths interpreted within the Plain of Tineh in various studies. The Sneh and Weissbrod (1973) feature was mapped east of the Suez Canal to Tell el Farama (Pelusium ruins), for 23 km. The study also mapped two small branches flowing due north from their main interpreted branch (Sneh and Weissbrod, 1973).

A later study by Hoffmeier and Abd El-Maksoud, (2003) focused on Tell el Borg, a fort on the military road, “The ways of Horus,” connecting Egypt to the Levant during pharaonic times. As a result of the archeology study, two branches were interpreted as an older, prior avulsion of the Pelusiac flowing into a paleo-lake connecting to the Mediterranean Sea around 2000-1000 B.Cu. (Hoffmeier and Abd El-Maksoud, 2003; Stanley et al. 2008). These are shown in Figure 1.4 in purple. The avulsion emptying into the interpreted Roman Mediterranean coastline was a result of the coastline regressing as

## Previous Studies- Plain of Tineh, Egypt

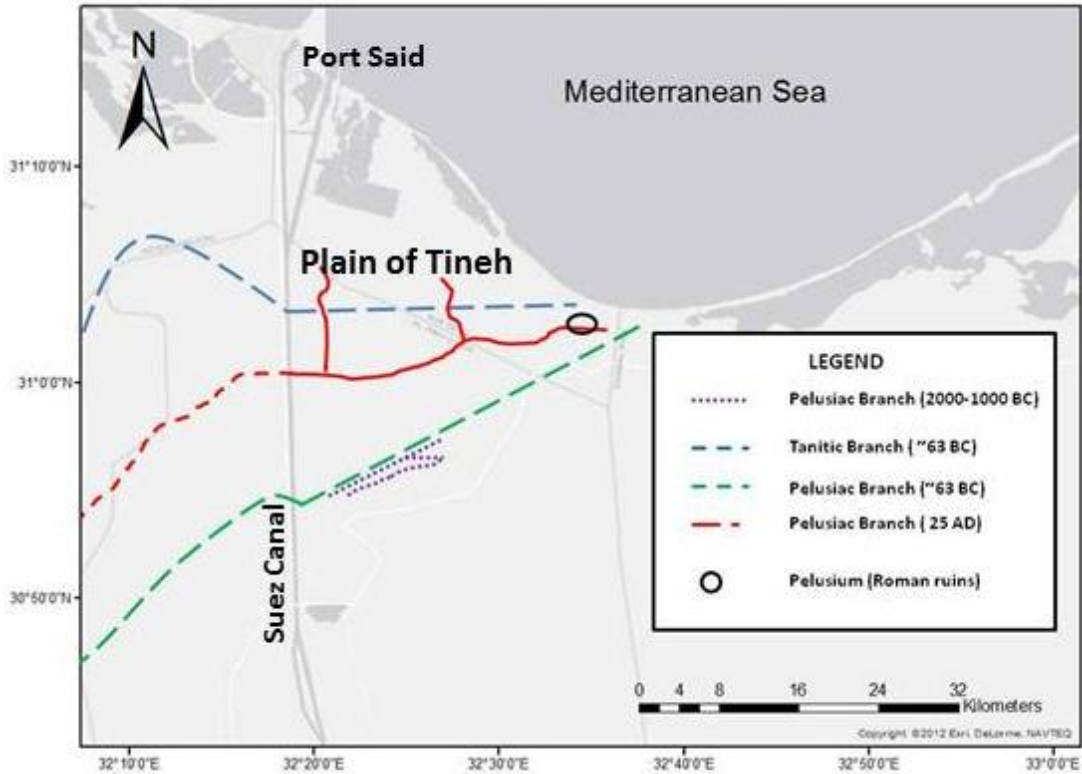


Figure 1.4: Various river paths attributed to the Pelusiac and Tanitic distributaries have been cited as flowing through the Plain of Tineh. The path of the Pelusiac circa 2000-1000 BC was reported by Hoffmeier and Abd- El Maksoud (2003) and tentatively dated by Stanley et al. (2008). The Tanitic and Pelusiac rivers at ~63 BC were mapped by Strabo (63 BC) and reported by Said (1981). Solid lines represent definitive vs. interpreted river paths (dashed). The Pelusiac branch which likely went defunct around 25 AD was presented by Sneh and Weissbrod (1973). Map created using ESRI ArcGIS 10.

the Nile delta grew (Hoffmeier and Abd El-Maksoud, 2003). The interpreted Pelusiac channel passed through the Tell el Borg dig site and consisted of dark Nilotic soils, shells found in the Nile River and pottery shards dated to the New Kingdom (Figure 1.4).

Historical maps authored by Herodotus (484-425 B.C) and later, Strabo (63 B.C.) portray the Pelusium Branch and even the Tanitic Branch flowing through the Plain of Tineh during the Late Holocene (Abdel-Kader, 1982; Said, 1981; Stanley et al., 2008).

These earlier works are inconsistent though, due to the limitations of the time. But, they suggest at least two of the Pelusiac River's avulsions are located on the northeastern extent of the delta and possibly the Tanitic distributary as well. These river paths are also shown in Figure 1.4.

**Quaternary Formations in the Nile Delta**

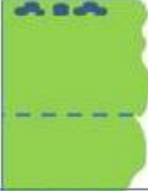
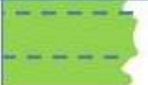
Age	Formation	Avg. Thickness	Lithology	River
Quaternary 3	Bilgas	50m		Neonile
Quaternary 2	Mit Ghamr	700m		Prenile
Quaternary 1	El Wastani	300m		Protonile

Figure 1.5: Columnar sections of subsurface deposits of the Nile Delta during the Quaternary. Modified after Rizzini et al. 1978 and Said, 1981.

## Objectives

The purpose of this study is to gain a more comprehensive understanding of the Pelusiac branch in the Plain of Tineh. The main objectives were to:

1. Image the Pelusiac branch using available remote sensing platforms and verify proposed flow paths of avulsions by locating physical linear features
2. Derive paleo-discharge estimations for the defunct Pelusiac using geomorphology and planform parameters and their associated relationships

3. Analyze sedimentology and stratigraphy along interpreted Mediterranean shoreline at 25A.D. from field data

## **1.5 Geologic Setting**

The Nile Delta saw three different main avulsions during the last 1.6 MY. These were the older Proto-Nile, the Pre-Nile and the Neo-Nile prior to the modern Nile River flowing today (Rizzini et al. 1978; Said, 1981). Figure 1.5 shows the Quaternary formations in the Nile Delta and related Nile River avulsion event. The modern Nile Delta reached its current configuration approximately 10,000 years ago (Rizzini et al., 1978). The delta plain and strandplain in the Plain of Tineh consist of Holocene age sediments as shown in Figure 1.6. The Nile Delta has been tectonically inactive throughout the Quaternary with the exception of small-scale earthquakes along the existing minor fault lines. The main structural feature on the plain is the Pelusium Line Fault (Figure 1.7). The Pelusium Line is a transcontinental shear trending northeast to southwest. Although the feature is considered active, there has been no appreciable movement in modern times (Said, 1981). The Pelusiac Line extends from the Levant southwest, to the southeastern part of the Mediterranean and northwest part of Sinai until it ends on the eastern extent of the Nile delta (Stanley et al., 2008).

## **1.6 Study Area**

The focus of this study lies in the easternmost part of the Nile River delta in Egypt in the Plain of Tineh at coordinates 31°15'0"N, 32°15'0"E (Figure 1.8). East of Port Said

## PLAIN OF TINEH Geology

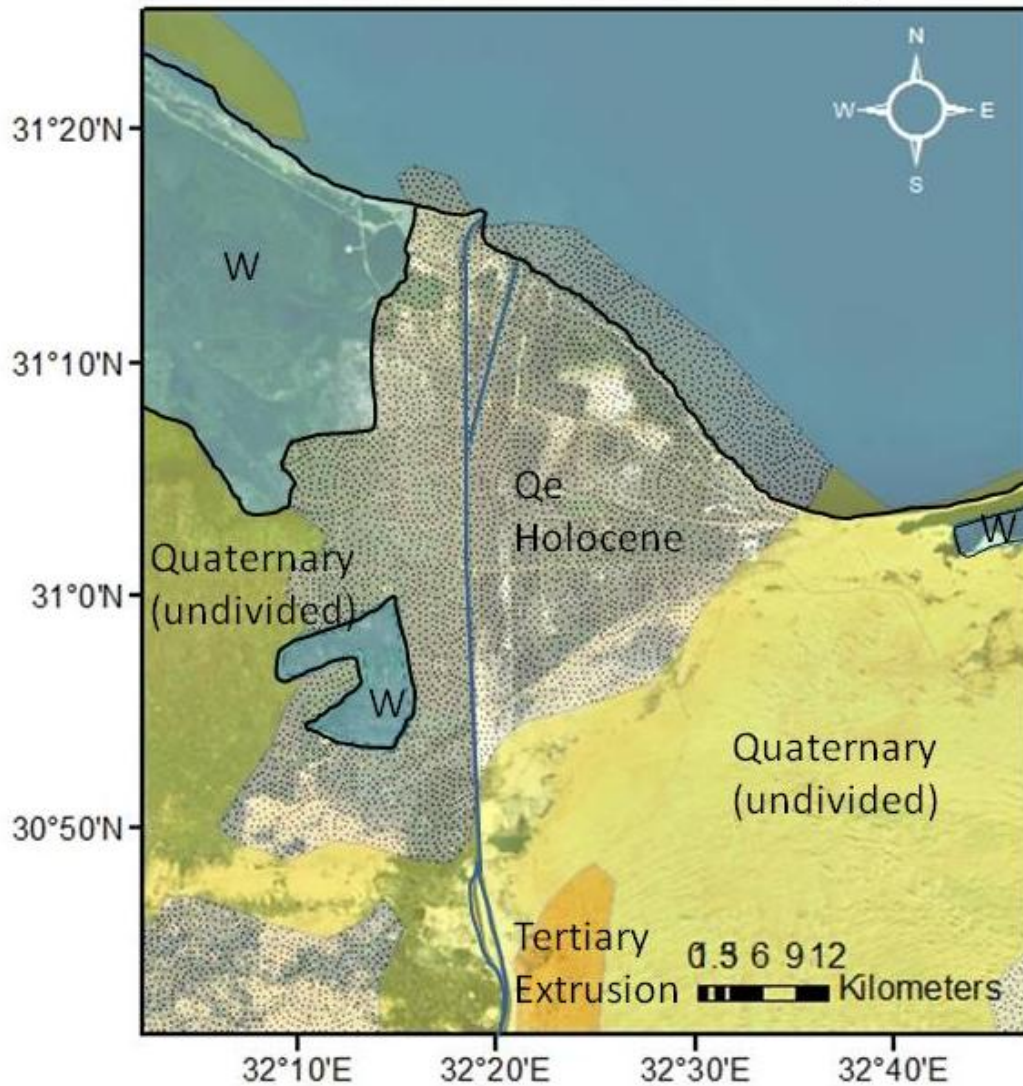


Figure 1.6: The Plain of Tineh geology ages for sediments are shown . The majority of sediments are Quaternary with some younger delta plain and the strandplain sediments belonging to the Holocene. The letter W shows locations with bodies of water. Map created in ArcGIS 10.

## Hillshade Analysis and Structural Elements

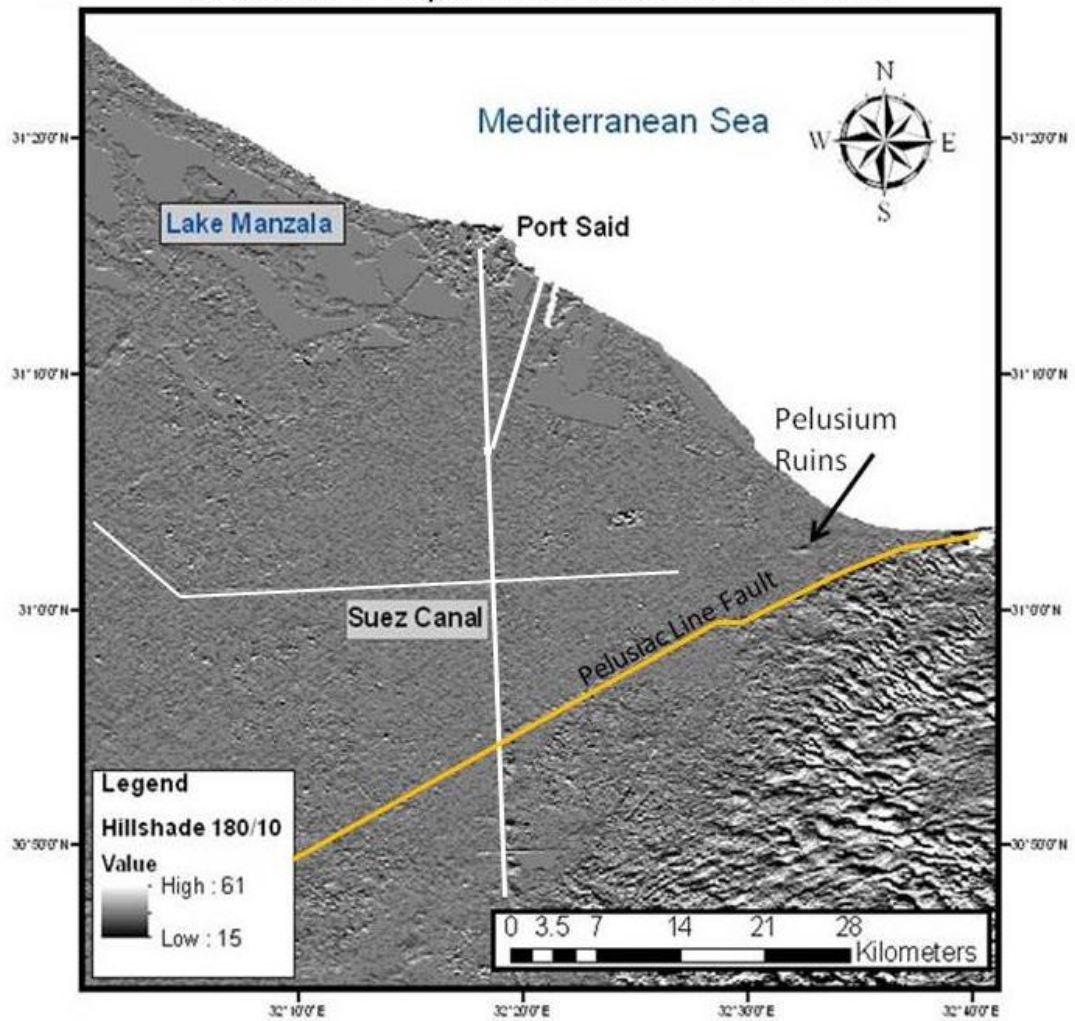


Figure 1.7: The main structural element in the Plain of Tineh, northeast Nile Delta Egypt. The Pelusiac Line Fault is a major transcontinental shear that trends northeast-southwest and has shown no appreciable movement in modern times (Neev, 1977). Hillshade analysis was applied to a DEM for delineation of structural features in the plain. Main canals are shown in white. Map created in ArcGIS 10.

lies the strandplain that defines the modern day coast of the Mediterranean (Coutellier and Stanley, 1987). The strandplain contains a series of low accretionary ridges. The wide deltaic plain extending through most of the southern part of the delta ranges from 1-2m above sea level south of the strandplain. It comprises muddy, deltaic deposits covered by a salt crust. The width of the strandplain varies from 1km in the east to 12.5 km in the west (Sneh and Weissbrod, 1973). To the southeast, NE-SW trending, linear dunes and coastal ridges are located south of Tell el Farama. The ridges parallel the trace of the

### Study Area- Plain of Tineh



Figure 1.8: Map of the study area in relation to the Nile Delta in Egypt. The red rectangle shows the study area. The delta plain east of the Suez Canal is called the Plain of Tineh. The City of Port Said is shown as well as protected archeological sites. Map created using ArcGIS 10.

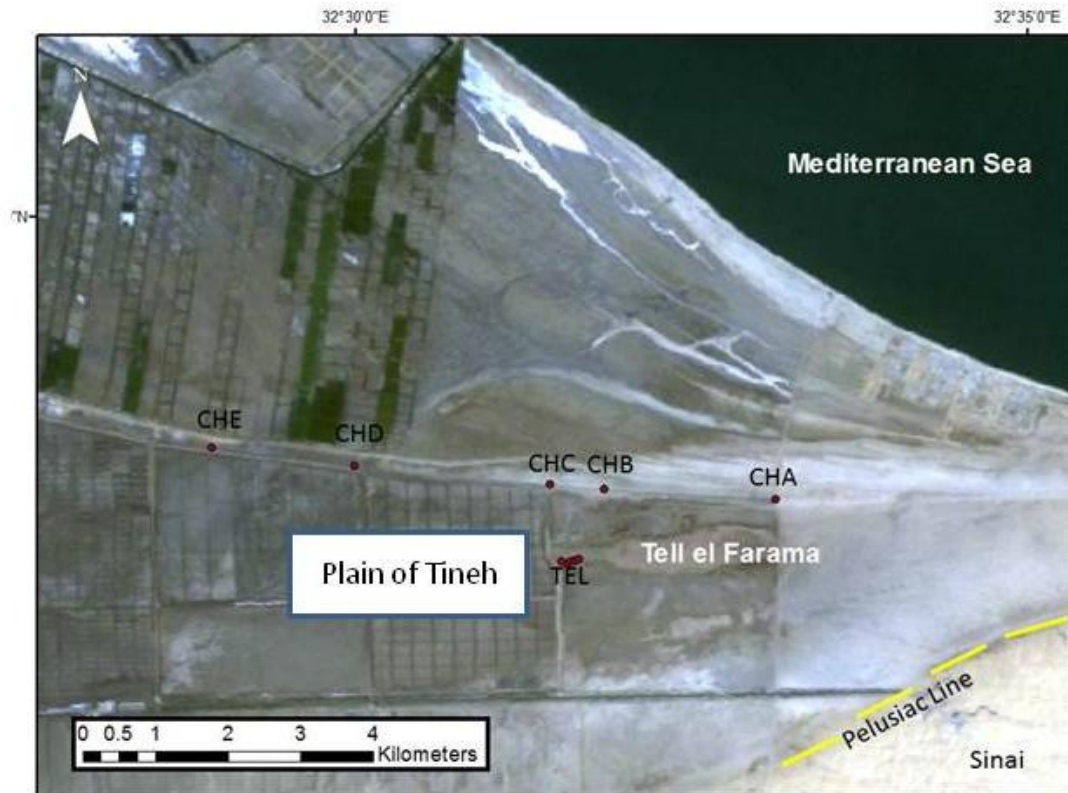


Figure 1.9: Location of field work sites within the Plain of Tineh. Red points correspond to stops where outcrops were measured and their corresponding section names. Landsat TM 1998, RGB 321.

#### Pelusiac Line transform fault.

Areas west of the Suez Canal area have been heavily cultivated for thousands of years, and most relict distributary channels have been incorporated into the irrigation canals. Although, the Plain of Tineh is currently cultivated, the changes in the plain are recent. This allowed for a greater probability of success in geologic studies, since the area has only been developed since the 1990s. The remote sensing analysis part of this study reviewed optical and radar products of the entire Plain of Tineh. Field work conducted in April of 2012, collected data along an irrigation canal to the east of the Pelusium and Tel

el Farama ruins. Figure 1.9 shows the area with locations of collected GPS points for the collected samples and measured sections discussed in the sedimentology chapter.

# **Chapter 2:**

# **Remote Sensing**

Remote sensing methods were applied to meet two different objectives. The first was to locate any remaining traces of the Pelusiac Branch beneath the agricultural cover in the Plain of Tineh. The second was to use the linear trace results for morphological analysis of the planform parameters. The process and results of meeting both objectives will be discussed in two separate sections; first, remote sensing analysis and then planform geometry analysis.

## **2.1 Remote Sensing Analysis**

In this study, optical and radar remote sensing data were implemented to image possible river traces of Pelusiac river avulsions located in the study area.

### **2.1.1 Remote Sensing Methods**

**Datasets-** Analyzed data included the recent high-resolution GeoEYE satellite imagery available through ESRI and SPOT imagery from Google Earth for 2012. Landsat Thematic Mapper (TM) and Landsat Multispectral Scanner System (MSS) datasets were also employed for in-depth analysis. The Landsat TM imagery used in this study was collected on November 11, 1998 and September 20, 1984. Available scenes cover swaths of 185 X 170 km at resolutions of up to 30m. The Landsat program uses a satellite platform to acquire multispectral optical data of Earth. The program has continuously collected data with a series of satellites—Landsat 1 (launched 1972) through Landsat 7 launched in 1999. (Lillesand et al., 2004). The Landsat MSS scene used in the study was collected in 1975 to show the Plain of Tineh prior to the agricultural development begun in the latter part of the decade. The Landsat MSS and TM data was used to detect land classes and changes in land cover and to discern visible linear traces at the surface.

The radar datasets were acquired from three different platforms in order to get a range of dates and resolution capabilities. These included PALSAR, RADARSAT-1, and TerraSAR-X data products. High-resolution German observation satellite, TerraSAR-X, was launched on June 15, 2007. Its active phased array X-band SAR antenna collects data products at resolutions of 18, 3, or 1m. Analyzed products included the SpotLight (1m resolution) and StripMap (up to 3m resolution and larger scene size). The higher resolution SpotLight product was able to resolve the ruin boundaries with greater detail in comparison to the PALSAR imagery.

PALSAR-The Phased Array L-band Synthetic Aperture Radar (PALSAR), has the capability to map the shallow subsurface with up to 10m resolution in fine resolution mode. PALSAR can operate in three modes—fine resolution, ScanSAR, and Polarimetric. In the fine resolution mode it can collect either single or dual polarization images (Lillesand et al., 2004). PALSAR is aboard the ALOS Japanese satellite launched in 2006 and provides continuous radar global data in mostly fine resolution and ScanSAR modes (Lillesand et al., 2004, Rosenqvist et al., 2004). The PALSAR dataset used was obtained in fine resolution mode with HH polarization.

The RADARSAT-1 satellite collects radar data in the C-band. It controls the measuring radar beam within a range of 5000 km to collect datasets at varying parameters. Resolution may range from 8-100 m and swaths may include up to 500 km in overall width. SIR-C satellite coverage for the region focused on the Suez Canal, and did not have enough coverage over the Plain of Tineh to provide a working radar dataset for

the study area. These datasets were not pursued further than a basic analysis of the available data along the immediate area of the Suez Canal.

**Image Processing-** The objective in the digital image processing phase was to discern differences as possible pinpoint markers. Lithology, soil moisture, and vegetation were of particular interest. Multiple image manipulation tools were applied using the ENVI interface including contrast stretches, density slicing, and band ratios. These band combinations were displayed as Red-Green-Blue (RGB), respectively. The image enhancement methods with the best results were exported from ENVI into ArcMap for finalization and addition of map elements.

### **2.1.2 Multispectral Remote Sensing Results**

The modern Plain of Tineh is shown in Figures 1.8 and 2.1 using GeoEye imagery, respectively. It is separated into four main regions: the beach, strandplain, delta plain, and desert. The area east of the Suez Canal is marked by rectangular fields and linear canals extending into the Sinai desert to the east. The Peace Canal flows in an east and west perpendicular to the Suez Canal. Apart from the desert dunes to the southeast, the most prominent features in the plain are the agricultural plots. These show up in Figure 2.1 as light green to dark blue rectangles. The darker reflections suggest that these are flooded. The optical imagery from the satellite clearly shows marked differentiation between the plain in lighter greens and the yellow sands of the dune fields to the

## PLAIN OF TINEH- Present

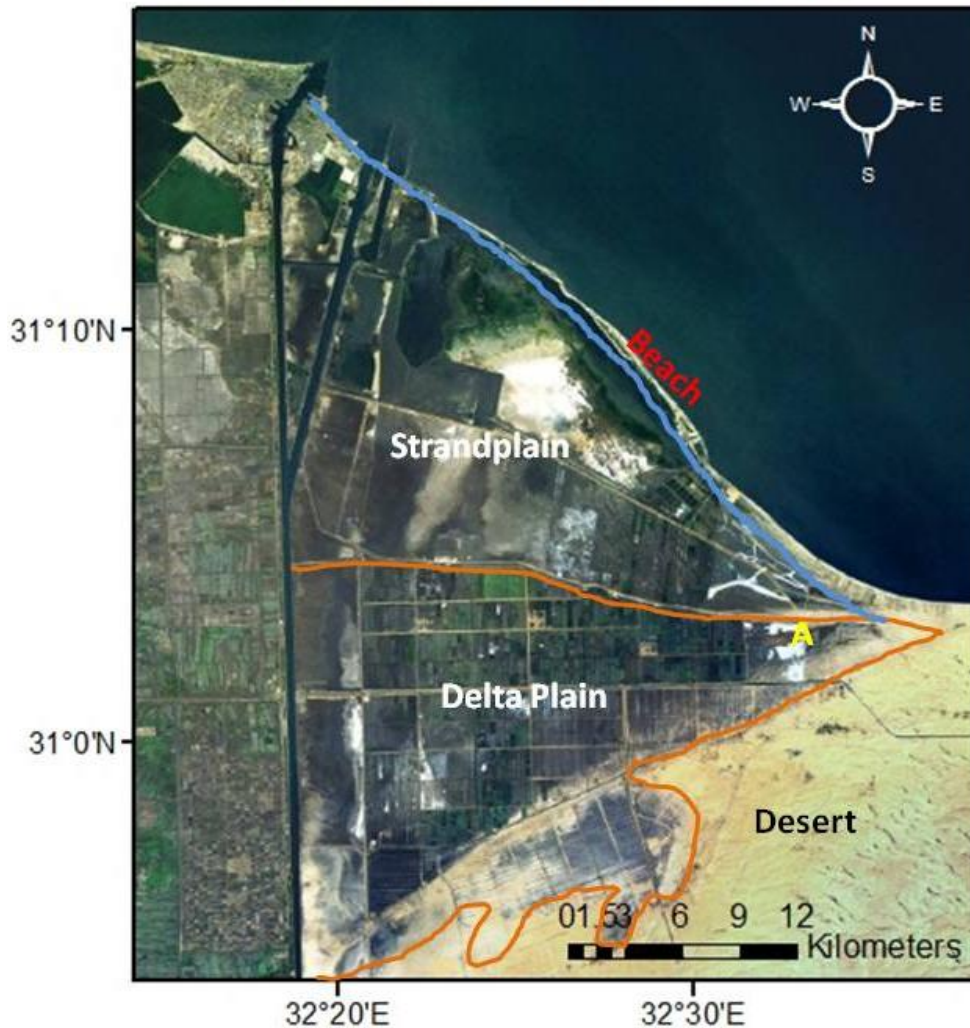


Figure 2.1: Plain of Tineh showing major feature divisions including delta plain, strandplain and beach deposits. The location of Ancient Pelusium is shown by the yellow 'A'. The blue line shows the boundary between the beach and strandplain. The orange line marks the boundaries of the delta plain.

southeast. Some of the dune crests are better delineated due to darker reflections from anchoring vegetation. The land surrounding the Tel el Farama and ancient Pelusium ruins is not urbanized. It is also surrounded by salt crusts with a very bright (white), strong reflection. Sabkhas also surround the local high upon which the ruins are located toward the west and may be differentiated from the surrounding plain by their darker coloration.

It is in direct contrast to the salt crust to the east. El Malaha lagoon is located in the north, two kilometers east of the Suez Canal. Extensive salt crusts cover its banks on the landward side of the lake. Salt may also be observed along the Suez Canal. Although the GeoEye imagery has high resolution, the agricultural gridding precludes observation of any linear features that might pertain to prior avulsions of the Pelusiac Branch. The area was analyzed carefully, but the majority of the fields were either inundated (dark blue reflection) or lay fallow (light greens or yellows) but had been worked in the past. Natural linear traces were not observed within the plain at all.

**Landsat TM, 1998-** Figure 2.2 shows the November 11, 1998 Landsat TM data. Different image processing routines were applied for both optical and radar datasets. Before enhancements were applied, datasets were first subset to cover the Plain of Tineh study area. Vegetation is very limited for the study area. The system of irrigation canals and road infrastructure is well defined on band 3 grayscale.

Figure 2.2 shows the Plain of Tineh study area from Landsat TM in grayscale Band 3. The strandplain (marked in Figure 2.1) contains large areas covered in salt crusts (bright white reflectance) to the south of the El Malaha lagoon (dark blue-black feature). The imagery shows it to be very shallow. Although the salt crusts are also observed in true color bands RGB 3-2-1, their extent is much more easily seen in grayscale band 3 as shown in Figure 2.2. In comparison to the GeoEye imagery, El Malaha is much decreased in size compared to over a decade ago. A third of its area, including the salt flat boundaries, has been reclaimed for agriculture and flooded as shown in the dataset in the intervening years. Another area of high salt concentration is immediately east of the Suez

Canal. This area is part of the delta plain, but the level of in-situ sediments is questionable due to their relative short distance from the Suez Canal. These areas remain bare of vegetation even today. To the east of El Malaha lagoon, accretionary ridges are easily picked-out. They consist of darker sands, outlined by salt crusts collected at the bases of the features. These ridges are most clear in the northeast corner of the strandplain in the Landsat 1998 image.

The strandplain is separated from the delta plain by the interpreted Mediterranean shoreline from Roman times (Figure 2.1). The delta plain is different in that it lacks accretionary ridges and appears to consist of different lithology from the strandplain as shown by the differences in reflectance in band 3. Figure 2.2 shows the sets of road infrastructure crisscrossing the delta plain. It appears as a grid stretching across the plain that divides the area into agricultural plots. Although the road infrastructure limits the visibility of the delta plain a linear feature is present running in an east to northwest direction. It begins at the Pelusium ruins and crosses the gridded plain in the direction of the Suez Canal (blue line in Figure 2.2). The feature is appreciated best on Band 3 and is shown in grayscale in Figure 2.2. The linear feature has dark colored boundaries, while the inside of the feature shows up as a lighter grey color, similar to that observed on the oval of the Pelusium ruins. Figure 2.3 shows the Landsat 1998 image using Zoom 4X in section B on the area west of the Pelusium ruins. This area clearly shows the linear feature, its channel width and the substrate differences in comparison to the rest of the plain. The feature can no longer be clearly discerned approximately 12 km from the Suez Canal.

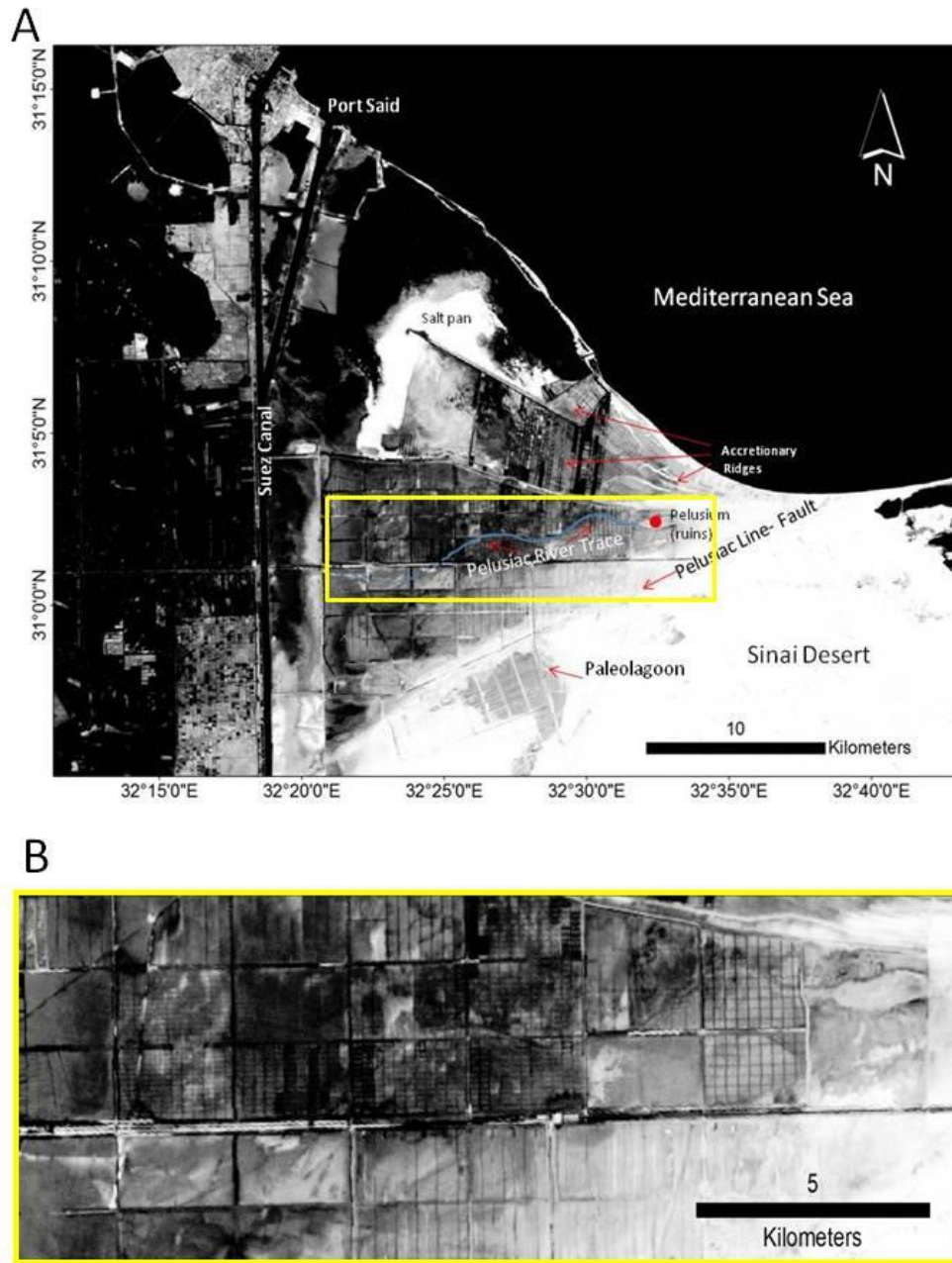


Figure 2.2: A: Landsat TM in Band 3 Grayscale showing location of zoomed in image shown in B in the Plain of Tineh, Nile Delta Egypt. B: The image displays a linear feature extending from the Tel el Farama (Pelusium) ruins, toward the west for 13km in the direction of the Suez Canal. The feature is then lost as it crosses the Peace Canal running east to west. Landsat TM Band 3 Grayscale. Data acquired November 11, 1998 Zoom 4X



Figure 2.3: A: A linear feature (number 5) was observed in the Nile Delta east of the Suez Canal that was interpreted as the lower end of the Roman Pelusiatic Branch. B: Although the main trace was observed for approximately 20km, the two smaller branching streams (Sneh and Weissbrod, 1973) were not observed. 1: Lagoon and salt crusts. 2: Ridges. 3: Suez Canal. 4: Pelusium ruins. 5: Linear trace. 6: 2<sup>nd</sup> Linear trace. . Data acquired September, 20, 1984. A: Landsat TM Bands 3-2-1 displayed as RGB. B: Landsat TM Bands 3-2-1 displayed as RGB. 4X Zoom. Data acquired Sept. 20, 1984

The delta plain is separated from the Sinai desert by a structural feature, the Pelusiac Fault. It can be observed on the Landsat 1998 image by the sharp contrast between the darker sediments of the delta plain in comparison to the very light colored sands of the desert. On the Digital Elevation Model (DEM) of the area, a sharp contrast in elevation is also present with the desert area being up to 14 meters above the delta plain. Dune crests are clearly shown in the other Landsat bands including in true color combination 3-2-1, but are not easily discerned in band 3.

Band 3 does portray a dark rounded feature south of the Pelusiac Line within the desert area. Circular in shape with a ribbon trailing to the southwest, the feature shows-up in Landsat band 3 the same as the delta plain sediments in color. This suggests identical lithologies between the delta plain and the paleolagoon region. Although the paleolagoon boundaries are clearly delineated, linear traces like the one distinguished in the delta plain, were not observed using the optical remote sensing images of the Landsat satellite.

**1984-** Landsat TM data acquired September 20, 1984 is shown in Figure 2.3. The Landsat images provide 7 bands that allow for multiple band combinations to be created and displayed in RGB. Band combinations were utilized for differentiation of features on the delta. Individual bands were also analyzed and proved more useful than the band combinations. But, the latter were better for lithology differentiation. In part A of Figure 2.3, the strandplain features are delineated more clearly using RGB 3-2-1 and a contrast stretch. El Malaha lagoon is shown at location 1 and does not show appreciable change in comparison to 1998 but the extent of the salt crust is greater in 1984. To the east of El Malaha, the accretionary ridge system can be clearly observed at location 2 from the

boundary of the lagoon to the end of the strandplain sediments. In this Landsat TM image shown in RGB 3-2-1, the area between ridges stands out as light, tan-colored to white, linear features. The delta plain is shown in varying shades of brown with vertical linear features trending southwest to northeast. These lines were found to be in the same location as many of the main road and canal infrastructure seen in Figure 2.2 from the 1998 imagery. Apart from the linear “infrastructure” roads, the plain is clearly observed, without vegetation or urban cover. At location 3 in Figure 2.3, salt crusts formed from saturation and subsequent evaporation of moisture cover the area immediately to the east of the Suez Canal. Unlike in the 1998 imagery, the salt crust stretches farther into the delta plain in 1984. The crust is bounded by very straight, black linear structures trending NNW/SSE. Possibly roads replaced by the new infrastructure. In location 4 on Figure 2.3, the dark brown oval observed is part of the Pelusium ruins. The oval is connected to the same linear trace observed on the 1998 Landsat imagery of Figures 2.2 and 2.3. The linear river trace can be followed for a greater distance in comparison to later imagery. The trace stretches from the Pelusium ruins all the way to the salt crust road boundary discussed earlier at location 3. The river trace shows color differences in the RGB 3-2-1 representation due to the dissimilarities of the infilling versus the adjacent material of the plain sediments. Figure 2.3, part B shows the linear feature magnified 4X. Although the river channel was more easily distinguished in the Landsat 1998 image, in the 1984 product, the trace can be followed for a longer distance with a greater amount of clarity and resolution. Location 7 on Figure 2.3 shows the sharp contrast between the delta plain sediments and desert outlining the boundaries of a paleolagoon. The north arm of the

lagoon is separated from the delta plain by a thin strip of sand desert body. The paleolagoon arm consists of the same sediments as the main lagoon body and the delta plain as shown in Figure 2.4 as well.

The boundaries of the features discussed are more noticeable using Band combination 4-6-5 displayed as RGB in Figure 2.4. Useful combinations for Landsat bands included RGB 543, 742, 754, 465, 654, and 632. Combinations 465 and 654 were the most valuable in differentiating between delta elements when coupled with equalization enhancement stretches. The colors in the image portray the different lithologies in the Plain of Tineh. The bright green and blues adjacent to the Suez Canal are sediments reworked during the construction of the canal and many are spoil piles.

Adjacent to this area are the salt crusts shown in bright red separated from the rest of the delta plain by a road showing as a bright green linear feature. The reds indicate high salinity in the form of the salt crusts. Red areas may also be observed along the southern shores of El Malaha lagoon. The lagoon itself and the Mediterranean Sea reflect dark black colors. The beaches of the strandplain are shown in a dark purple color while the dune sands are shown in violet suggesting a difference in composition from the Sinai desert to the accreted beaches. The Pelusium ruins show as a bright aqua blue color as does the pristine plain area immediately to the east of the ruins. The rest of the delta plain is a combination of areas with high salinity, delta sediments and sand covers, but the band combination greater clarity when analyzing the study area lithology.

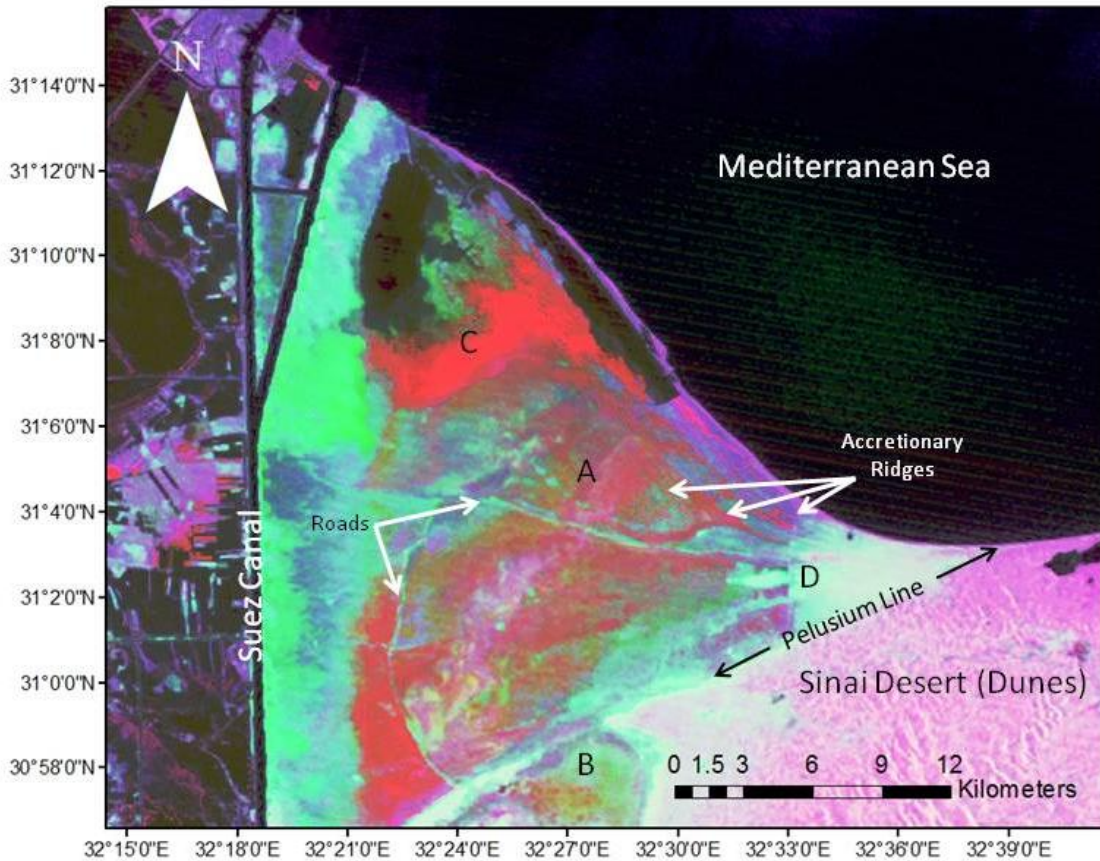


Figure 2.4: The Plain of Tineh using band combination 465 and an equalization filter. The combination helps to denote differences in the observable lithology of the plain. A. Accretionary ridges. B: Paleolagoon (originally and intradistributary bay). C: Salt crust. D: Pelusium ruins. Data acquired Sept. 20, 1984. Landsat TM. Bands 4-6-5 displayed as RGB.

The Landsat 1984 images also showed the linear trace extending from the Pelusium ruins (Figure 2.4). In the 1984 dataset, the feature begins near the old road features near the reworked edges of the Suez Canal all the way to the Pelusium ruins. The accretionary ridges are also more clearly seen and followed throughout the strandplain to the edges of El Malaha lagoon. The accretionary ridges are not as well defined as in the grayscale band 3, but the dune crests to the southwest were clearly delineated.

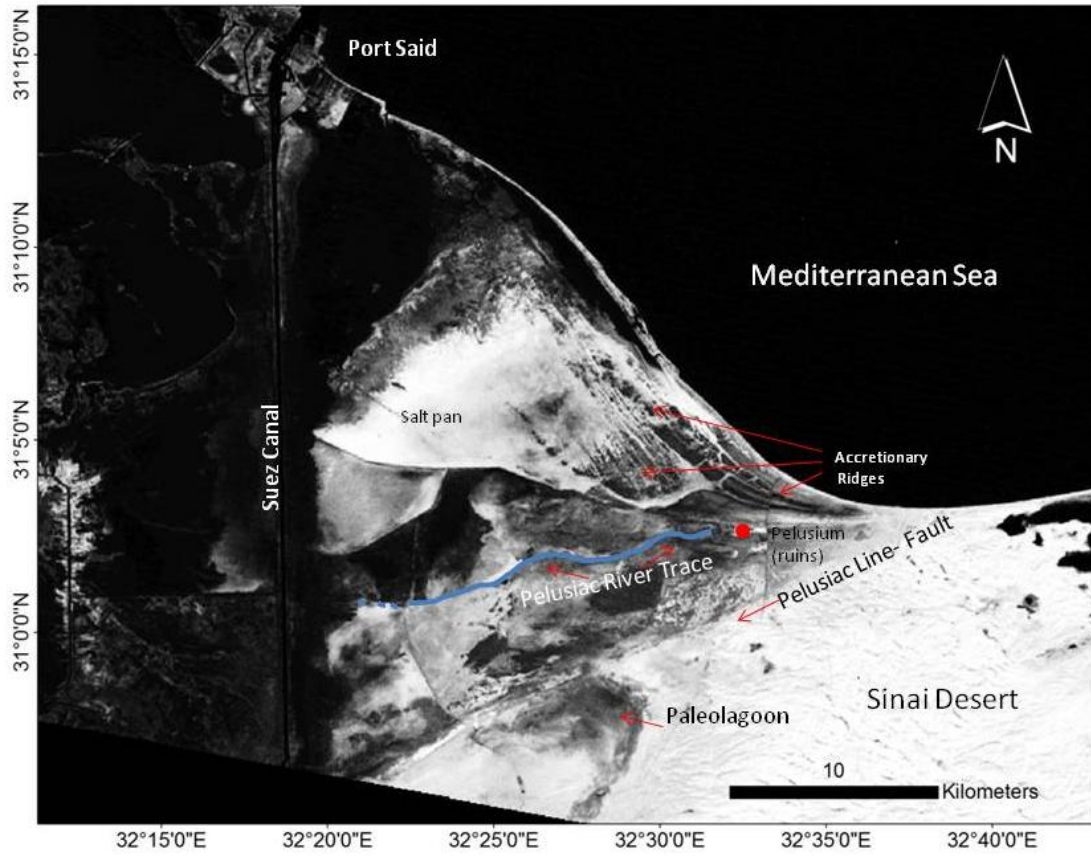


Figure 2.5: Plain of Tineh showing major geological features. The location of Ancient Pelusium is shown in red. The image delineates the Roman Pelusiac trace for over 13km, 4km further west than Landsat imagery from the late 90s after the Peace Canal was completed as shown below. The older New Kingdom trace of Pelusiac was not observed in the area west of the paleolagoon. Multi- Spectral Scanner 1975 Band 4 Grayscale

**1975-** An older Landsat Multi- Spectral Scanner product from 1975 was acquired and analyzed. Figure 2.5 portrays the image product in Band 4 Grayscale. In relation to the linear traces of the Pelusiac river channels, the 1975 imagery was not very useful over the Landsat 1984 products. The linear trace of the roman path of the Pelusiac may be followed from the Pelusium ruins to the road east of the Suez Canal for a length of 13km, but the Landsat 1984 imagery was clearer with a higher resolution. The MSS imagery does portray the changes to the plain in the decade between the MSS 1975 and Landsat

1984 imagery. This is particularly true when comparing the datasets for changes to the extent of El Malaha lagoon. Its area has been greatly decreased. The extent of salt crusts on the plain is also greater in the 1975 dataset. The salt crusts are located not only on the shores of El Malaha, but also on cover a wider area on the delta plain. The wide sheet extending from El Malaha covers over a third of the strandplain. The paleolagoon was clearly delineated in Figure 2.5, but river channel traces were not observed in the earlier image either.

### **2.1.3 RADAR Results**

The PALSAR image was subset since the majority of the plain was agriculturally developed. The focus was narrowed down to the area surrounding the Pelusiac ruins, since analysis of the Landsat products showed a promising linear trace extending from the ruins, into the delta plain. The PALSAR image was captured in HH polarization and filtering was applied to reduce noise after subsetting. The resulting image showed the outline of the Pelusium ruins as a large rectangle outlined in white. It is surrounded by other smaller features also in white with the main square walls delineated in white on the darker plain (Letter A in Figure 2.6). Immediately north of the Pelusium ruins is a light colored area about a kilometer long. This is a sabkha feature and has a lower elevation than the surrounding substrate where water accumulates. It in turn forms a hardened polygon crust on the surface. The Tell el Farama ruins are also visible east of the Pelusium ruins. The rest of the untouched delta plain lacks appreciable differences in substrate. To the west of the Pelusium ruins (Letter B in Figure 2.6) lie very geometric plots related to agriculture of the Plain of Tineh. Although individual ridges can be seen

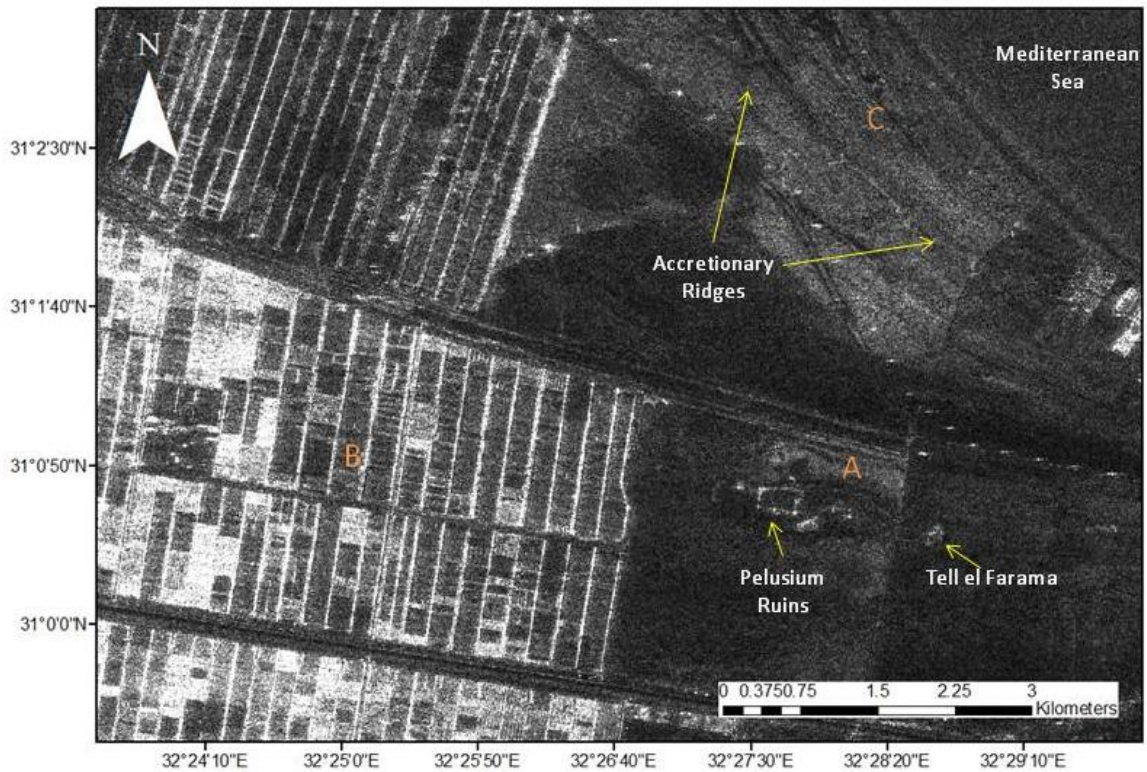


Figure 2.6: PALSAR image subset of the Plain of Tineh. The Pelusium ruins (A) and extensive agricultural fields (B) are clearly observed. Although the accretionary ridges (C) may be distinguished in the strandplain, they are not well delineated using radar imagery.

as dark lines crossing the lighter strandplain, they are soon lost while traversing through darker patches of strandplain sands.

**RADARSAT-1:** A subset of the dataset from RADARSAT-1 satellite was utilized in this study (Figure 2.7). The RADARSAT dataset was of lower resolution in comparison to the PALSAR data product (Figure 2.6). Although the road and field infrastructure grid was already in place at the time the RADARSAT dataset was collected, the farms had not yet been put in use. The accretionary ridges in the northeast part of the strandplain are clearly marked in dark colors in comparison to the grey spotted plain. South of this area at the Pelusium ruins (Letter A in Figure 2.7), the ruins themselves cannot be seen as they

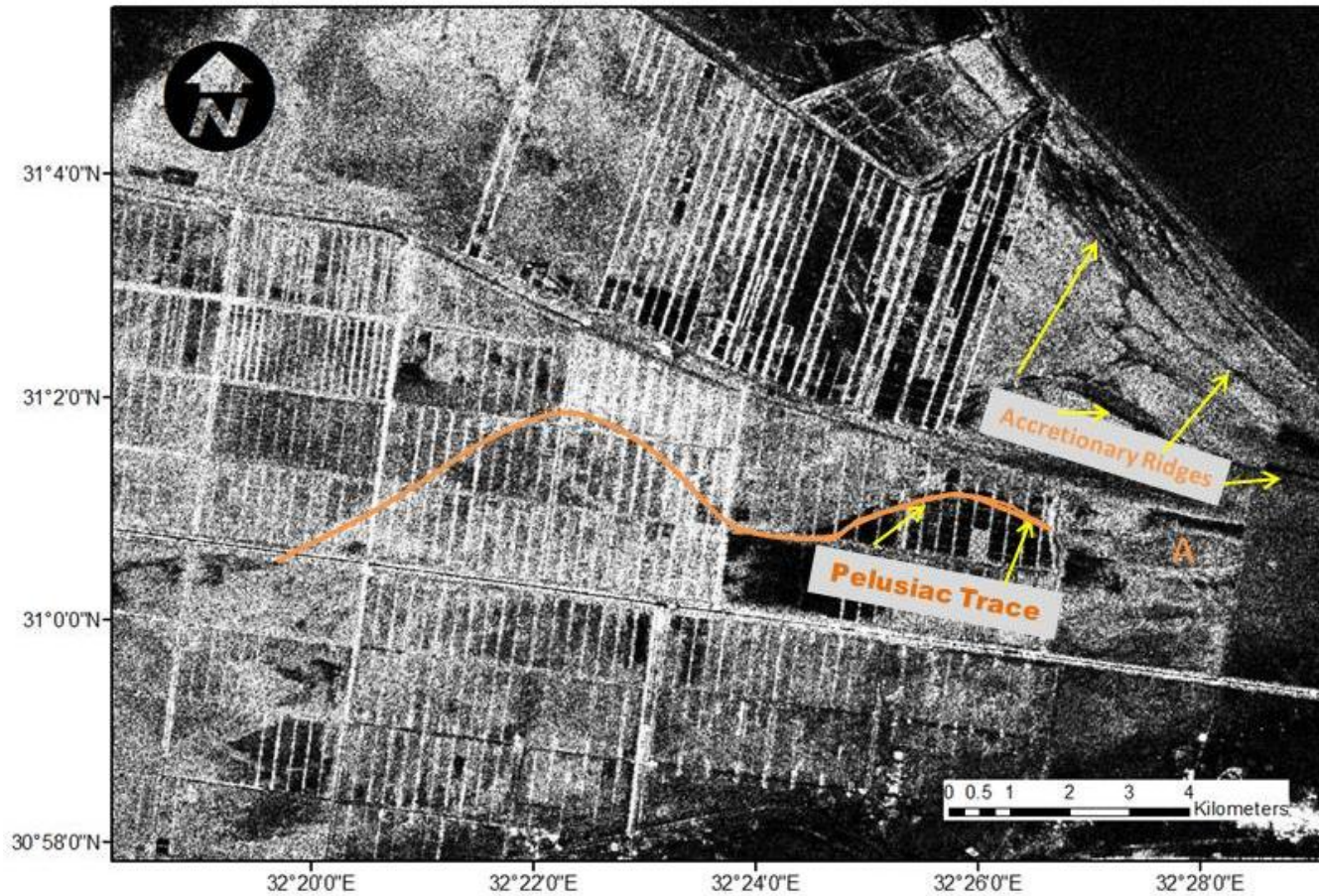


Figure 2.7: Radarsat-1 image product collected in HH polarization of the Plain of Tineh, Egypt. The letter A denotes the Pelusium ruin area shown by an oval shape. The Pelusiac River trace may be seen extending from the ruin area to the west for approximately four kilometers.

were in the PALSAR imagery. Instead, the rise upon which the ruins are set is clearly delineated as a kilometer long oval. The area surrounding the ruins is marked by changing greys and blacks due to differences in soil moisture. West of the Pelusium ruins, the linear trace ending at the ruins is delineated for approximately 8 kilometers. The linear feature is marked by light grey fields to the north of the feature, while the south contains black fields where it is seen more clearly. Although more detail was available from the Landsat dataset, the Radarsat-1 image did show the linear feature for 8km.

**SIR-C:** The 1994 datasets collected in the Giza, Egypt area from the SIR-C/X-SAR instrument aboard the NASA Space Shuttle Endeavor were also analyzed. The instrument recorded in X, C, and L bands providing radar back-scatter for HH, VV, HV, and VH polarizations like the PALSAR instrument (Thurmond et al. 2006). These datasets were collected prior to the termination of construction for the Peace Canal, but coverage for the plain of Tineh was poor and/or unavailable for the area of study and further analysis was not possible.

**TerraSAR-X:** The higher resolution SpotLight product was able to resolve the ruin boundaries with greater detail in comparison to the PALSAR imagery. The accretionary ridges are discernible in the north within the strandplain in Figure 2.8. The first thick ridge shaped in a long 'S' is also a strong feature. Smaller ridges may also be discerned by magnifying the image further. The ruins of Pelusium are located in a dark oval shape feature. To the west of the ruin's oval area is also a dark, straight linear

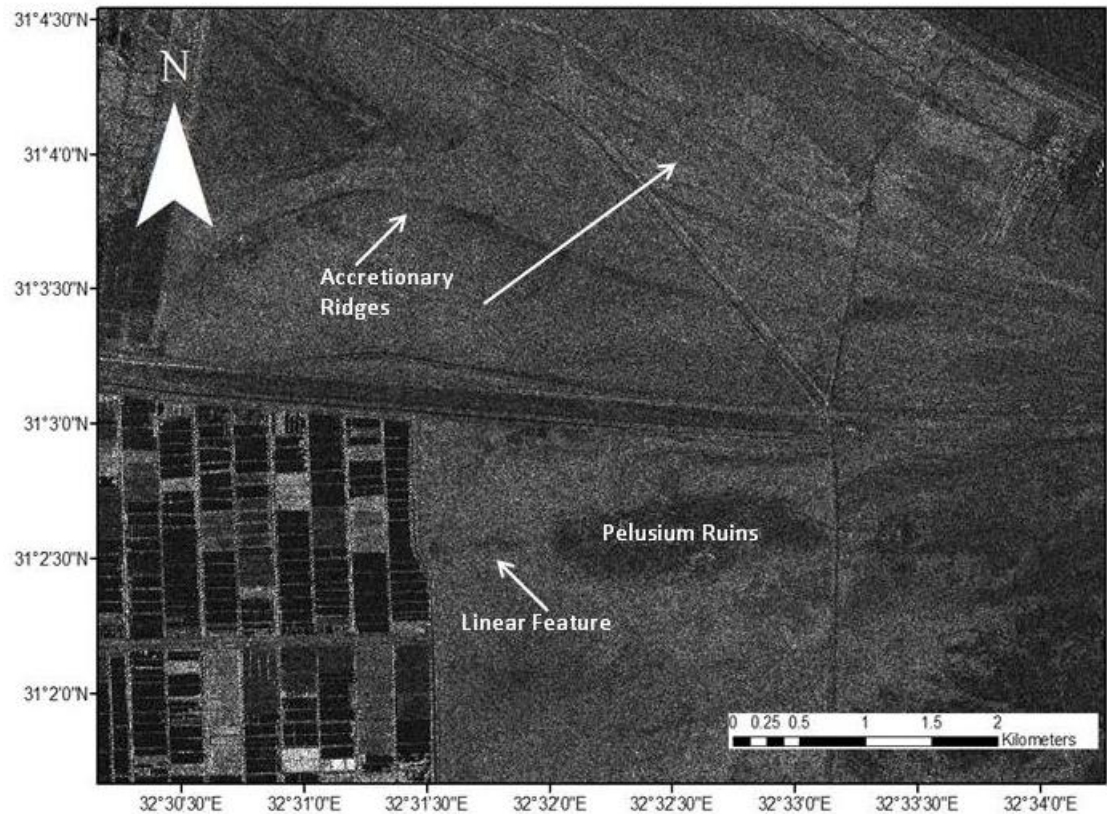


Figure 2.8: The Pelusium ruin area in the Plain of Tineh as observed from the high –resolution TerraSAR-X satellite. A darker linear feature extends from the Pelusium ruins to the fish farms fields located 0.5 km west.

feature that is lost at the boundary with the agricultural plots. The area to east of the Pelusium and Tel el Farama ruins was ignored in previous studies, but neither Landsat nor these high-resolution radar products were able to image any unusual features there.

#### 2.1.4 Remote Sensing Interpretations

The Pelusiac River flow paths provided by the previous studies including Sneh and Weissbrod (1973) and Hoffmeier and Abd-El Maksoud (2003) could not be distinguished at all using recent GeoEye optical imagery. This was in part because areas lacking water or vegetation cover were limited to acreage along the Suez Canal, which

was extensively reworked during the construction of the Canal. The archeological area for Tel el Farama and ancient Pelusium was not reworked, but no trace was observed in those areas either. Only sabkha and salt crust environments can be observed surrounding the ruins. The northern beaches were also un-vegetated but most of the area north of the Al Kantara Shark- Al Arish Road has been added onto the delta as longshore accretion and is of younger age than the Pelusiac Branch. For optical imagery, the 1998 Landsat dataset was the latest to show a linear trace ending at the Pelusium ruins area. The trace was clearly delineated for approximately 12 km on the Landsat TM dataset. The earlier datasets from 1984 and 1975 provided a greater observable length of up to 20km, but resolution dropped, especially for the Landsat MSS 1975 images.

Radar data has the capability to image the subsurface through the use of long wavelength radar signals and in extremely arid environments; radar can be very effective because subsurface features will appear brighter (Elachi et al, 1994; Gaber et al, 2011). Elachi et al (1994) explains that the refraction at the air/sand boundary causes the apparent enhancement of the image since it results in a smaller incidence angle. A smaller incidence angle means a stronger backscatter return which acts as sufficient compensation for the absorption at the surface sand boundary and the scattering and reflection at the sand/air boundary (Elachi et al, 1994). Imaging depth for low moisture sand has been measured at 1.5m to 3m for sand dune type deposits.

The radar datasets were analyzed using contrast stretches, but were first treated for speckles using smoothing and sharpening filters. The mid-level sharpening filter provided more satisfactory, clear results. The road infrastructure and individual fields are

clearly delineated. Unfortunately, the reflectance of the roads is very strong and fallow areas cannot be observed in detail. Furthermore, many of the fields are flooded and used for fish farming. The resulting ponds block the radar signal from penetrating the surface. Also, the accretionary ridges that were clearly observed in the Landsat images were not as prominent in radar.

In the PALSAR image, the linear feature west of the Pelusium ruins was not observed. The linear feature is marked by light grey fields to the north of the feature, while the south contains black fields. It is possible this area was flooded, highlighting the feature in this area. The RADARSAT dataset has lower resolution, but for the purposes of delineating subsurface features, it had greater value in this study. It was able to image the same feature east of the Pelusium ruins as the Landsat imagery, though for a much shorter duration. RADAR was useful for subsurface imaging, but its efficiency was obstructed by the agricultural development of the plain, fish farming ponds, and other factors which combined to obstruct the radar signal.

The linear feature west of the Pelusium ruins was used to create a shapefile in ArcGIS. The shapefile was used to compare it to the similar feature seen on the Landsat and RADAR datasets. The feature was located in the same location within the different datasets. The shapefile was then compared to the imported and geo-referenced map created by Sneh and Weissbrod (1973) of their interpreted Pelusiac Branch. The results were a very close match and support the linear feature being a trace for the Pelusiac. The trace showed a very low sinuosity, but was not completely straight which decreases the possibility of being a dug canal to the Pelusium ruins. The only other river passing

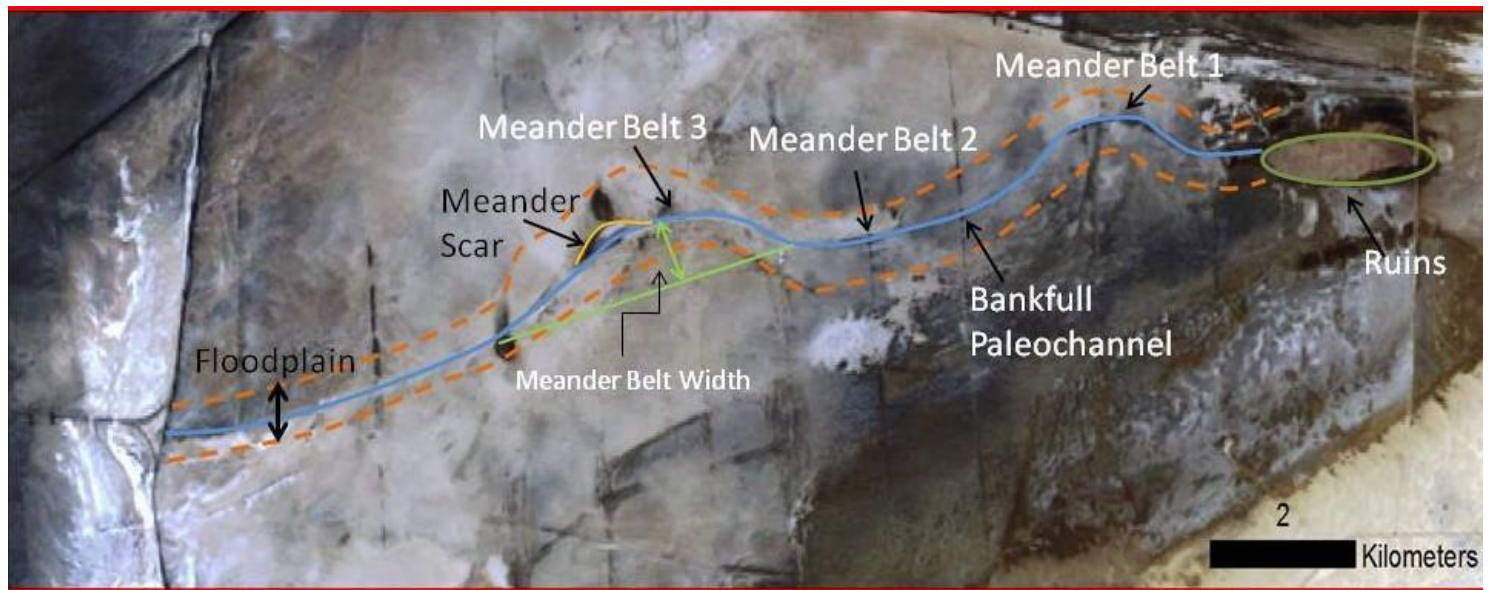


Figure 2.9: Interpreted fluvial geomorphology for the Pelusiac River in the Plain of Tineh. The meander belts, Pelusiac paleochannel and floodplain are shown as interpreted from remote sensing analysis of Landsat imagery. B: Landsat TM Bands 3-2-1 displayed as RGB. 4X Zoom. Data acquired Sept. 20, 1984

through the Plain of Tineh was the Tanitic according to Said (1981) and it was supposed to empty near Port Said. So, the linear feature extending from the Pelusium ruins is instead interpreted as a Pelusiac distributary channel. No other Pelusiac or linear features relating to river channels were imaged using the available datasets in this area. Figure 2.9 shows the interpreted geomorphology of the Pelusiac paleochannel. The Landsat TM 1984 image was the dataset providing the greatest amount of detail for the Plain. Using the above discussed methods to analyze the image, some of the river features related to the Pelusiac were interpreted. The paleochannel trace is outlined in blue. Bracketing the feature is a ~1km wide flood plain. The meander belts were also labeled as well as a feature interpreted as a meander scar. Figure 2.9 clearly portrays the dimensions of the paleochannel in planform within the delta plain.

Other observed features included the accretionary ridges. The shape of the ridges show that the accreted area was added on by an early, thick, loose 'S' shaped ridge shoreline. The bay like indentation between the promontory at Manzala Lagoon (lagoon west of Suez Canal) and this first ridge was then filled in by smaller (less thick) subsequent ridges before the indentation was filled. New ridge accretions likely added onto the modern shoreline shape until it reached its current configuration. The youngest ridge was dated at 25A.D. by Sneh and Weissbrod (1973) with the modern beach and spit of El Malaha marking the modern shoreline today. The reason that the ridges accreted in this fashion might be related to the mouth of the Pelusiac being located in the immediate area of the Pelusium ruins. The river sediments must have created a promontory at the

mouth. It is likely the remnants of the promontory affected how the ridges accreted onto the area in front of the river mouth.

The second unknown linear feature observed in Figure 2.4 (location 6), was a straight linear feature cutting into the Pelusiatic river trace west of the Pelusium ruins. Research into the plain showed that Sneh et al. (1975) proposed the feature to be a man-made canal. The straight geometry of the feature as observed on the Landsat image supports human constructions, since natural features are not normally so well defined in straight lines.

Although most image enhancement methods were constructive in portraying differences in lithology, for the study's objective, most were of limited use and visual discrimination through the application of band combinations was key. Contrast stretches were particularly useful. Supervised classification was performed on the Landsat data. Maximum likelihood classification provided good definition for multiple areas throughout the different years, but discrimination between the delta plain covered by a thin salt crust and thick salt crust concentrations along water body edges was problematic. Minimum distance classification provided similar results. Unsupervised classification was also attempted, but results were inconclusive and were very different to supervised classification results. Principal Component (PC) analysis and density slicing were also applied in ENVI using manipulation of bands, but the results were unsatisfactory. Band ratios were also created for individual and RGB false color image analysis. Nine band ratios were produced: 3/4, 4/3, 5/7, 2/3, 3/2, 4/5, 5/4, 3/5 and 7/2.

The use of band ratios did not produce great results and band combinations were instead focused on.

By utilizing Landsat TM and MSS, river features were successfully recognized based on observed shade variations of the plain. For lithologic differences in the delta plain, band combinations RGB 465 and 654 differentiated best and river channel features were delineated more clearly when imaged as a single grayscale band in either band 1 or 3. Although the earlier datasets were the most valuable for analysis of the river channel features in the Plain of Tineh, the greater resolution of the 1980s products were preferable to the lower quality available imagery of the 70s.

## **2.2 Planform Analysis**

The remote sensing analysis findings were used to map the flow path of a late avulsion of the Pelusiac in the Plain of Tineh. The river trace's channel parameters were subsequently mapped and measured to analyze the river morphology along the observable length of the river trace.

### **2.2.1 Planform Geometry**

River morphology may be used to portray changes in magnitudes of discharge, both water and sediment, even when long-term hydrologic and stream flow measurements were not recorded (Sridhar, 2007). Discharge of water and sediments, in turn, determines the dimension of river channel geometry including width, depth, meander wavelength, and slope (Schumm, 1968).

# River Channel Patterns

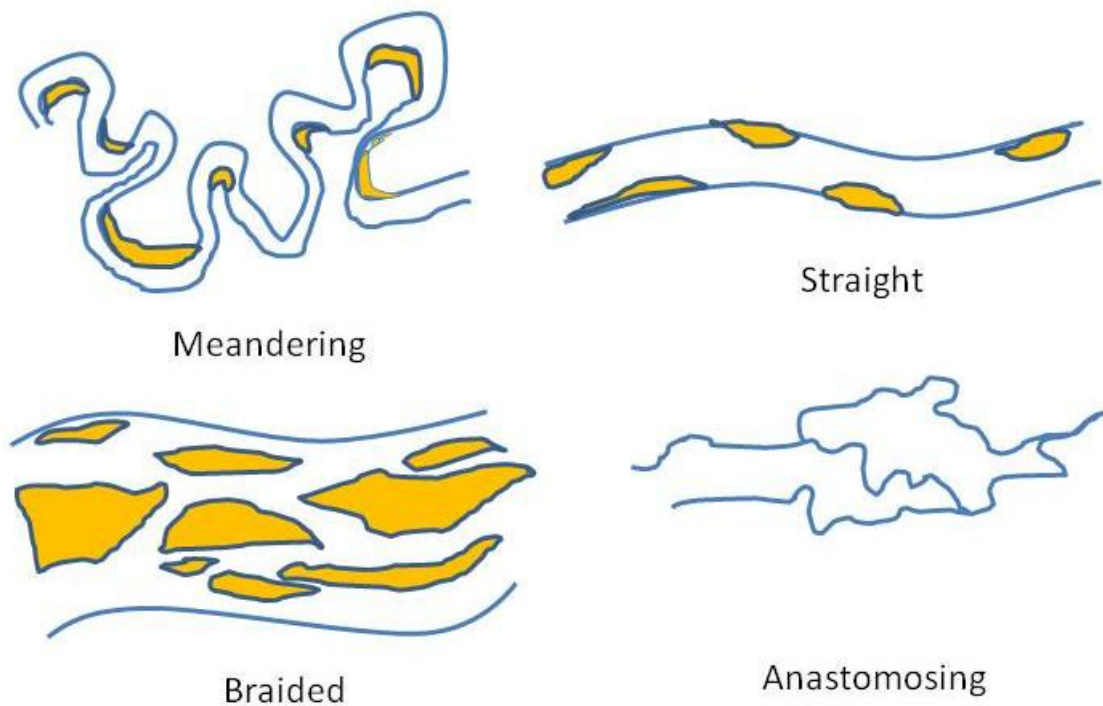


Figure 2.10: Types of principal river patterns seen in planform view . Modified from Miall, (1977).

Discharge is the amount of water passing any point in the stream at a given time. Channels will conform to changing discharge due to changes in water and/or sediment load over time. As discharge increases, normally depth, length, and velocity also increase. Although discharge changes are caused by multiple basin variables, a comparison of past and present channel morphology may quantify changes in the discharge regime of a river over time (Rosgen, 1994; Rosgen, 1996; Sridhar, 2007). Meander wavelengths, channel patterns, and paleochannel dimension relationships were first applied for paleohydrogeology by Dury (1954, 1976) and Schumm (1968). Their

equations allow paleo-discharge to be estimated using the empirical relationships between discharge and channel dimensions, such as those developed by Williams (1988).

Channel dimensions, as studied in river geomorphology, has focused on meander and braided rivers (Zhang et al. 2008). The four main river channel patterns are meandering, straight, anastomosing and braided as shown in Figure 2.10. Meanders are looping curves or bends found in sinuous river streams caused by differences in valley-slope, bed-load, discharge, bed-resistance and transverse oscillation (Zhang et al. 2008).

Channel dimensions relationships have been established early between meander parameters and hydrologic parameters (Dury 1954, 1976; Schumm, 1968; Williams 1988). Parameters include bankfull channel width ( $W_b$ ), bankfull cross-sectional area

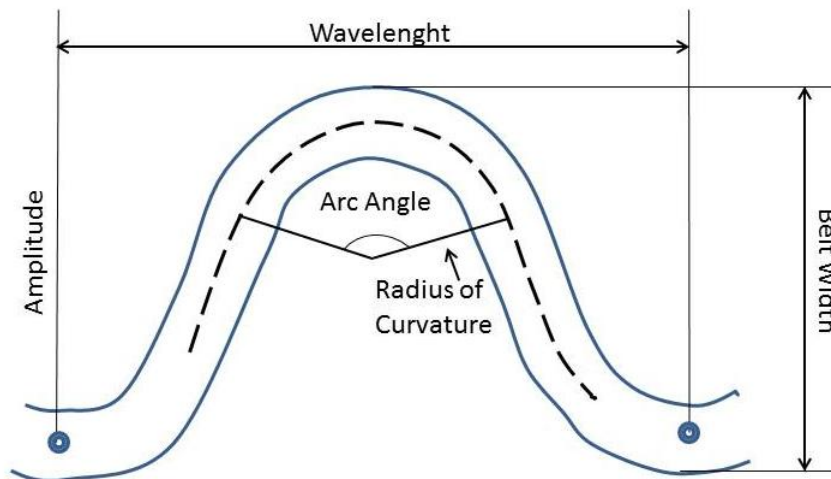


Figure 2.11: An idealized meander in planform view. The wavelength, belt width, and radius of curvature were all measured for the meanders in the study area. Modified from Williams (1986).

(Ac), and bankfull channel depth (Db). Other meander specific features include the wavelength (Lm), bend length (Lb), belt width (B), and radius of curvature (Figure 2.11).

The visible planform trace of the Pelusiac was used to calculate paleochannel morphology-related discharge estimates for comparison with the Damietta distributary post-Aswan Dam. The geomorphologic evidence and channel geometry measurements of the paleochannel were used to quantify changes of the paleo-hydrologic regime for the Pelusiac Branch prior to 25 AD when it ceased to flow.

### **2.2.2 Planform Measurement Methods**

The river planform analysis and discharge estimation calculations were performed using the results from the remote sensing analysis. Measurements for the formulas were collected using Landsat TM imagery from 1998 and 1984. The four paleochannel meanders imaged in the Landsat TM datasets were used for the values of the Pelusiac river trace in order to collect information concerning the Pelusiac after it went defunct. Values of interest included meander width and depth, and particularly paleo-discharge estimations. Ten meanders were also chosen for analysis from the terminal Damietta distributary for comparison and validation of the Pelusiac values. (Fig. 2.12a). Meander 1 is in the actual promontory and Meander 10 is 56km from the river mouth. Meanders in proximity to the river mouth were chosen because the three Pelusiac paleomeanders (Fig.2.12b) were located a few kilometers from the known shoreline of the Mediterranean coast during Roman times, before the river went defunct. Meander 3 is located almost 12 km from the Roman coastline while Meander 1 is about 3km from the same. Planform

parameters were measured using the measurement tool in ESRI's ArcGIS software. The tool measures lengths of lines and polylines. Measurements were based along the centerline of the channel when possible.

### **2.2.3 Calculated Planform Results**

A comparison of the paleochannel and modern day Damietta channel geometry was undertaken. The dimensions of the channels including width and depth, meander length, and belt width were measured for three paleomeanders of the defunct Pelusiac. The three observable paleomeanders were first measured, and then the planform channel dimension estimations for the Pelusiac were calculated based on empirical relations by Williams (1988). A reach average was then obtained (Table 2.1). The Pelusiac paleoreach average was applied within the empirical relationships discussed previously. Results show that the paleochannel reach with a meander wavelength,  $L_m$ , of 6000 m, has a corresponding average bankfull width of 390 m and a bankfull depth of ~7 m. Bankfull flow is defined as river flow that fills the channel to the top of its banks (Williams, 1978). For geomorphology, the bankfull level is considered to be at the active floodplain according to Williams (1978). Bankfull discharge usually occurs during flooding when discharge is high enough to reach its bankfull stage (Williams, 1978). The Damietta modern day reach average (Table 2.2) obtained from ten present-day meanders show that an average channel meander with a meander wavelength of 4500 m has a bankfull width of 300 m and a bankfull depth of ~6 m. The percent difference between the Pelusiac reach average bankfull channel width and bankfull channel depth and the

### The Damietta Branch and Promontory



### Pelusiatic Trace Paleomeanders



Figure 2.12: Overview of study area. Top: The Damietta Promontory and modern-day Damietta Branch flow north through the Nile delta into the Mediterranean Sea. Meanders chosen within the terminal reach are shown. Bottom: The Plain of Tineh is shown. The Pelusiac River is traced in blue and the visible meanders are numbered. The Pelusiac Line fault and the Roman Coast line are also presented. Source Landsat TM Bands 321 RGB Data acquired November 11, 1998.

Damietta reach is 26% and 13% respectively. The proximity in both bankfull width and depth is unexpected as is the Pelusiac channel's somewhat greater width and depth. Summerhayes et al. (1978) illustrated changes across the delta to include a classical phase, 5000 years ago, where more than seven small distributaries, including the Pelusiac discharged sediment into the Mediterranean, before flow was confined to two distributaries (the Rosetta and Damietta) during the past 500 years. As a result, the combined flow into only two distributaries suggests that a considerable difference in channel dimensions between a small paleochannel and a larger Damietta should be observed. Table 2.3 compares the planform characters of the Damietta meanders and Pelusiac paleomeanders in greater detail. The Pelusiac channel is wider and deeper than the modern terminal Damietta channel. The width-depth ratio is correspondingly higher for the Pelusiac. Smaller widths may indicate a smaller discharge value and/or decreases in coarse sediment load. Width-depth ratios are often higher for channels with high bank erosion and higher coarse loads (Sridhar, 2007). The Pelusiac is also much less sinuous, with a Sinuosity Index of 1.04 vs. the Damietta's 1.60. Based on the index, the Pelusiac pattern would be classified as straight as compared to the Damietta's meandering pattern. The meander width ratio is higher for the Damietta at 8.01 while the Pelusiac's is a low 1.95. The cross-sectional area is estimated at 2100 m<sup>2</sup> for the modern Damietta. The Pelusiac had an estimated cross-sectional area of 3300 m<sup>2</sup>; a difference of more than 1000m<sup>2</sup>.

### Channel Dimensions- Pelusiac Paleomeanders

Location	Meander wavelength in meters (measured) $L_m$	Bankfull width in meters ( $W_b=0.17L_m^{0.89}$ )	Bankfull depth in meters ( $D_b=0.12W_b^{0.69}$ )
Paleomeander 1	4825.91	322.73	6.46
Paleomeander 2	6508.94	421.18	7.76
Paleomeander 3	6670.59	430.48	7.88
<b>Reach Average</b>	<b>6001.81</b>	<b>391.46</b>	<b>7.37</b>

48

Estimates are based on empirical relations by Williams (1988)

$L_m$ = meander wavelength,  $W_b$ = bankfull width,  $D_b$ = bankfull depth

Table 2.1: The table presents channel dimension estimations for the Pelusiac paleomeanders observed in the optical remote sensing imagery analysis.

### Channel Dimensions- Damietta distributary

No.	Location	Meander wavelength in meters (measured) $L_m$	Bankfull width in meters $(W_b=0.17L_m^{0.89})$	Bankfull depth in meters $(D_b=0.12W_b^{0.69})$
1	Damietta A	6030.59	393.52	7.41
2	Damietta B	7662.79	487.03	8.58
3	Izbat Mustafa Al Laddam A	2919.47	206.33	4.74
4	Izbat Mustafa Al Laddam B	5367.48	354.77	6.90
5	Izbat Wulsun A	2103.11	154.10	3.88
6	Izbat Wulsun B	6231.13	405.15	7.56
7	Izbat Waqf Qandil A	4175.01	283.68	5.91
8	Izbat Waqf Qandil B	4324.52	292.71	6.04
9	Izbat Al Qurayi A	3247.02	226.81	5.07
10	Izbat Al Qurayi B	2923.87	206.61	4.75
	<b>Reach Average</b>	<b>4498.50</b>	<b>301.07</b>	<b>6.08</b>

Estimates are based on empirical relations by Williams (1988)

$L_m$ = meander wavelength,  $W_b$ = bankfull width,  $D_b$ = bankfull depth

Table 2.2: Ten meanders were chosen from the terminal Damietta distributary branch and measured at their 2012 dimensions for comparison to the Pelusiac paleomeanders. The channel dimension estimations are presented in this table.

Dury (1976) showed that discharge may be quantified using its empirical relation to channel width, meander wavelength, cross-section area and channel slope. Discharge estimations were calculated using equations developed by Williams (1978) and Osterkamp and Hedman (1982). Table 2.4 shows calculated bankfull discharge and average discharge at the locations of the measured meanders for both the Damietta and Pelusiac paleomeanders. Bankfull discharge for the Pelusiac was around  $5700 \text{ m}^3 \text{ s}^{-1}$  while the average discharge would have been around  $650 \text{ m}^3 \text{ s}^{-1}$  using the reach average (Table 2.5). The modern Damietta has a calculated bankfull discharge of  $5100 \text{ m}^3$  while the average discharge is  $420 \text{ m}^3 \text{ s}^{-1}$ . The percent difference for bankfull discharge and average discharge for the compared reaches is 11% and 43%, respectively. Discharge equations developed by Dury (1976), Carlston (1965), Pickup and Warner (1984) and Bishop and Godley (1994) were also utilized (Table 2.5). Although values vary greatly among resulting discharges, the Pelusiac continues to trend as the larger waterway when comparing discharge, just as in bankfull width and depth.

Natural differences in rivers and channel meanders as well as accuracy in measurement of reach variables makes discharge estimations represent broad estimates since river wide local variability is not examined for the whole (Williams, 1978, 1986). Although neither hydrologic nor streamflow records are available for the Pelusiac for comparison, discharge and channel planform data is available for the modern Damietta and was used for estimation verification. On average, the Damietta has a sinuosity of 1.3 as reported by Negm et al. 2011. The measured sinuosity for the lower 56km of Damietta reach for this study was 1.6.

### Planform Characters Comparison

Channel Planform Parameter	Label/Units	Relation Used	Pelusiatic Past	Damietta Present
Meander Wavelength	$L_m$ (m)	measured	6001.81	4498.50
Bankfull Channel Width	$W_b$ (m)	$W_b = 0.17L_m^{0.89}$	391.85	303.17
Bankfull Channel Depth	$D_b$ (m)	$D_b = 0.027L_m^{0.66}$	8.40	6.96
		$D_b = 0.12W_b^{0.69}$	7.37	6.19
Cross-Section Area	$A_c$ (m <sup>2</sup> )	$A_c = W_b D_b$	3289.73	2108.96
		$A_c = 0.0054L_m^{1.53}$	3259.61	2096.95
Width Depth Ratio			46.67	43.58
Meander Width Ratio			1.95	8.01
Sinuosity Index	Si		1.04	1.60

Table 2.3: The measured and calculated planform characters for the chosen Damietta meanders in 2012 and the Pelusiatic river paleomeanders from optical imagery. Parameter values are averaged based on measurements at various meanders from Tables 2.1 and 2.2.

### Meander discharge- average and bankfull

No.	Location	Average Discharge (m <sup>3</sup> s <sup>-1</sup> ) $Q=0.027W_b^{1.69}$	Bankfull Discharge (m <sup>3</sup> s <sup>-1</sup> ) $Q_b= 4.0 A_b^{1.21}S^{0.28}$
1	Damietta A	655.94	8834.09
2	Damietta B	940.44	13844.10
3	Izbat Mustafa Al Laddam A	220.29	2266.08
4	Izbat Mustafa Al Laddam B	550.52	7100.38
5	Izbat Wulsun A	134.51	1224.97
6	Izbat Wulsun B	689.02	9393.06
7	Izbat Waqf Qandil A	377.27	4432.41
8	Izbat Waqf Qandil B	397.77	4734.77
9	Izbat Al Qurayi A	258.49	2766.22
10	Izbat Al Qurayi B	220.79	2272.49
	Reach Average	444.50	5686.86
1	Pelusiatic Paleomeander 1	469.13	3280.08
2	Pelusiatic Paleomeander 2	735.74	5653.97
3	Pelusiatic Paleomeander 3	763.39	5912.13
	Reach Average	656.09	4948.72

Q- Average discharge; Q<sub>b</sub>- Bankfull discharge; A<sub>b</sub>- Bankfull cross section area; S- Slope

Figure 2.4: Paleo-discharge was calculated for the Pelusiatic paleomeanders and the Damietta meanders chosen for comparison of results. The discharge estimates for both locations are presented in m<sup>3</sup> s<sup>-1</sup>. Equations are from Osterkamp and Hedman (1982) and Williams (1978).

**Discharge Comparison- present Damietta and Pelusiac paleomeanders**

Discharge Type	Discharge Equation	Creator	Damietta Present	Pelusiac Past
Average Discharge	$Q=0.027W_b^{1.69}$	Osterkamp and Hedman (1982)	444.50	656.09
Average Discharge	$Q=0.000017L_m^{2.15}$	Carlston (1965)	1214.91	2258.17
Average Discharge	$Q= [(W/2.99)^{1.81} + (L/32.857)^{1.81}] + 0.83A_c^{1.09}*\Omega /3$	Dury (1976)	5742.60	6100.18
Bankfull Discharge	$Q_b=(W_b/2.99)^{1.82}$	Dury (1976)	4476.46	7140.97
Bankfull Discharge	$Q_{2.33}=(W_b^{0.96}*(D_b^{0.6}))/2.2$	Bishop and Godley (1994)	351.09	502.80
Bankfull Discharge	$Q_b=4.0 (A_b^{1.21})(S^{0.28})$	Williams (1978)	5686.86	4948.72

Table 2.5: Discharge estimates for the present Damietta and defunct Pelusiac paleomeanders using reach average channel dimensions. Q- Average discharge;  $Q_b$  - Bankfull discharge;  $A_b$  - Bankfull cross-section area;  $\Omega$ - Sinuosity, S- Slope. Calculated values are based on reach averages.

The average width is reported as approximately 280m (Negm et al. 2011) and this study calculated bankfull width at 301m. Using the average discharge estimation equation of Osterkamp and Hedman (1982), this study found the Damietta’s present average discharge to be  $\sim 420 \text{ m}^3 \text{ s}^{-1}$ . Fanos et al. (1993) reported average discharge for the Damietta Branch to be  $563 \text{ m}^3 \text{ s}^{-1}$ . The percent difference between the two discharge values is 29%. The difference in discharge may be explained by the present study’s focus on the lower 56km reach of the Damietta Branch. Although normally water increases downstream due to the additions of rainfall, tributary discharge and/or groundwater seepage, this is not the case for the Nile delta. Due to large withdrawals of water for irrigation purposes, discharge actually decreases downstream (El-Din, 1977). Since the discharge estimations are in accordance for the modern Damietta, the average discharge of  $650 \text{ m}^3 \text{ s}^{-1}$  seems a reasonable estimate for the paleoflow of the defunct Pelusiac Branch of the Nile delta.

## 2.3 Discussion

### **The utility of remote sensing applications, sensor capability, and study timing**

The Pelusiac river trace was imaged using optical imagery from the Landsat TM sensor in the Plain of Tineh. The observed linear feature is 135 m wide at its maximum and approximately 13 km long. It extends from Tell el Farama toward the east in the direction of the Suez Canal, just north of the Peace Canal. The trace is lost within 10 km of the Suez Canal near the point where it intersects the Peace Canal as a result of extensive construction undertaken to create the new canal structure in the Plain and being near the reach of the reworked area from construction of the Suez Canal as well. One of the objectives of this study was to locate a buried Pelusiac river channel in order to apply planform geometry equations to learn about the paleo-hydrologic regime of the river prior to becoming defunct. Planform analysis requires a preserved planform view of the river so that channel measurements may be collected. In the case of the defunct Pelusiac, a planview paleochannel could only be acquired using remote sensing platforms, since the river trace was infilled and covered by other sediments along the east part of the delta. This is true for the majority of the recorded paleochannels in the delta through time. Studies intent on finding accurate locations for ancient river beds in the Nile delta are implemented using geophysical methods such as GPR, based upon historical accounts for location discrimination. Although these methods have proved effective, they are limited to smaller study areas and their results cannot be used for planform analysis. Furthermore, they are hindered by the focus of the Egyptian population along the delta and the continued urbanization of the area through time. In the Plain of Tineh,

development of the area was minimal prior to the middle 90s and the ruins of Pelusium were once located at the mouth of the Pelusiac river. This increased the probability of locating a planform trace there. Furthermore, Sneh and Weissbrod, 1973 reported the discovery of a river trace in this area. Since the focus of the study was the discovery of the feature and its location, their results only provided a simplified map showing the flow path of the river feature. The lack of higher resolution and accuracy of the presented results precluded the use of the data for our study's objective. Furthermore, this feature may no longer be observed today due to the agricultural fields covering the area. Instead, a remote sensing analysis was carried out focusing on the modern high resolution sensors available in order to locate the reported feature.

The utility of remote sensing studies in geology has been repeatedly proven throughout the last decade and continues to increase as technology continues to improve. Advantages include remote collection of data, repetitive coverage, cost effectiveness, widespread coverage and quick data collection times. In order to increase the effectiveness of these sensors, studies areas must meet as many criteria as possible to reach the "ideal conditions." In the study area, widespread agricultural fields including fish farm ponds, cover almost all of the delta plain and part of the strandplain. Although imagery from the SPOT was available with spatial resolutions of 10m, the land cover prevented the detection of buried channels using optical imagery using current datasets. The analysis results found the Landsat TM datasets from 1984 to be most effective for imaging the Pelusiac river trace. The spatial resolution for these images was 30m. Although the use of the Landsat TM data greatly diminished the available spatial resolution for the study in

comparison to SPOT, the ideal conditions of a sandy, non-vegetated or anthropologically developed plain were met during the time period the data was collected. Similar limitations were met when using radar platforms, including the high resolution TerraSAR-X datasets. Older radar datasets, including RADARSAT-1, were more useful and showed the Pelusiac trace for short distances in comparison to the higher resolution datasets due to the Plain being less developed. Radar remote sensing data for the Plain of Tineh was not available for dates prior to the development of this area, since radar does not have as consistent data coverage as multi-spectral remote sensing. The validity of the remote sensing methods' results was to be confirmed using Ground Penetrating Radar (GPR) surveys during the field season. The area prevents a suitable response due to the shallow water table on the plain (Figure 2.13). Furthermore, the groundwater is highly saline. The greatest detriment to GPR surveys for this study was the fish farm ponds located along the Pelusiac trace discerned from the remote sensing analysis. Nonetheless, the available resolution from the more timely Landsat imagery allowed for the required measurements to be taken from the channel paleo-meanders.



Figure 2.13 : The water table is considerably shallow in the Plain of Tineh. Marine water intrusion is also an inherent problem and the salinity of the groundwater is very high as a result. (Photographs courtesy J. Quintanar)

## **The validity of discharge estimations with a focus on paleo-discharge**

River basin studies using paleo- and modern channel geometries most recently applied in studies including Amsler et al. (2005), Callow and Smetten (2006) and Sridhar (2007). Although this study compared two different distributaries of the Nile River at different points in time, the results serve to portray the similarity between the defunct Pelusiac and the modern Damietta in both channel parameters and average and bankfull discharge. These results were unexpected, as Summerhayes et al. (1978) illustrated changes across the delta to include a classical phase, 5000 years ago, where more than seven small distributaries, including the Pelusiac discharged sediment into the Mediterranean before flow was confined to two distributaries (the Rosetta and Damietta) during the past 500 years. As a result, the combined flow into only two distributaries would suggest a considerable difference in channel dimensions and discharge between a small paleochannel and a larger Damietta channel. Instead, the data portray two similarly sized channels, and the Pelusiac paleochannel appears to have had a greater discharge.

Channel width may vary over short distances for many streams. Dimensions also vary through time due to water and sediment supply changes and even anthropologic factors (Dury, 1976). The incongruity of a larger paleochannel is due to a combination of all three factors. Anthropologic factors have played the most significant role within the last century. Until the 1900s, discharge reaching the Mediterranean Sea was measured at 100 billion  $\text{m}^3\text{yr}^{-1}$ . Egypt's flood season lasted from August to October, and the greatest discharge was observed in those months. The lower Aswan Dam was then finished in 1902 and discharge decreased to 35 billion  $\text{m}^3\text{yr}^{-1}$ . A second dam was built in Aswan, the

Aswan High Dam. It was completed in 1964 and completely controls discharge of water in northern Egypt. Presently, only small amounts of Nile water reach the Mediterranean, as the majority is diverted into irrigation canals in the delta (El-Din, 1977). The Damietta itself is dammed by two barrages along its reach. The southern barrage is the Zifta Barrage in the city of Zifta. The Faraskour Bank is located further north between meanders 5 and 6 in the study area. Not only has water supply been affected by human influence on the Nile, but sediment discharge as well. Pre-Aswan Dam, sediment discharge to the Mediterranean ranged from 60 to 180 million tons a year. Only a fraction of that value makes it to the coast today since the majority of sediment gets trapped behind the Aswan High Dam in the Lake Nasser Reservoir. Within the last hundred years, channel morphology has been primarily driven by anthropogenic factors as the Nile continues to be controlled by man.

Channel dimensions vary through time due to the various many variables, including those discussed in this study. The natural variability of rivers and channel meanders as well as accuracy of measurement make discharge estimations represent broad estimates for a studied reach since river wide local variability cannot be fully examined due to the limitations of the observed Pelusiac trace in the remote sensing analysis (Williams, 1978, 1986). Nonetheless, discharge estimations as developed by Osterkamp and Hedman (1982) and Williams (1978) portray a Pelusiac Branch that prior to its demise was not only similar in planform character and discharge to the modern day Damietta, but had slightly greater values in both.

# **Chapter 3: Stratigraphy and Sedimentology**

Field work was conducted on April 25, 2012 in the Plain of Tineh located east of the Suez Canal in the northeastern Nile Delta. Exposed beds along a major irrigation canal running parallel to the Al Kantara Shark- Al Arish road were measured and described. In addition to field observations for lithofacies interpretation, samples were collected for further analysis including identification of mollusk fossils, diatom analysis and laser particle size analysis. Stratigraphic sections were also created and a shoreline oblique transect is analyzed and discussed.

### **3.1 Methods**

**Field Work-** The primary data was derived from exposed outcrops along an irrigation canal flowing parallel for most of the length of the Al Kantar Shark-Al Arish Road to the north and west of the Pelusium ruins. Four sections were chosen and sedimentological and stratigraphic data collected along an irrigation canal flowing parallel to the paleo-shoreline of the Mediterranean at ~25 A.D. The sections were measured and information regarding sedimentary structures, lithofacies, grain size, and fossils was collected.

A hand-held GPS device was used to document the exact position of the measured sections at every stop. Sections were measured using measuring tape and grain sizes recorded using a grain-size card based on the Wentworth classification. A small shovel and hammer were used to scrape fresh faces as necessary. Samples were collected from different horizons at every measured section and bagged and transported to the United

States for further laboratory work. Pictures were taken along the canal measured sections to document and complement the field studies.

**Laboratory Work-** Stratigraphic sections were drawn using Adobe Photoshop and were used to identify and correlate similar facies. Correlations were based on lithofacies, certain sedimentary structures and shell fossils.

Laser particle size analysis (LPSA) was completed on June 18, 2012 in the Department of Earth Science at Rice University using a Malvern Mastersizer 2000. The instrument was run on tap water and each sample run twice for result comparison. Samples consisted of sands, muds and clays. The samples were prepared by deflocculating with sodium metaphosphate. Notations were made concerning samples with magnetic grains. Samples CHB-4b contained a large amount of broken shell matter and was too coarse for the Malvern to process. This sample was measured for grain size manually. The rest of the samples were measured without incident and results processed using Excel software.

Fossiliferous samples were sieved and shell samples collected for identification. Shells were washed using water and a small brush to remove sand and clay matter. These were then photographed and identified using the guide to Mediterranean Sea Shells appended by George Tornaritis. Identification was based upon shell features and photographic recognition of identical samples. Shell samples were valuable for their contribution to environment of deposition.

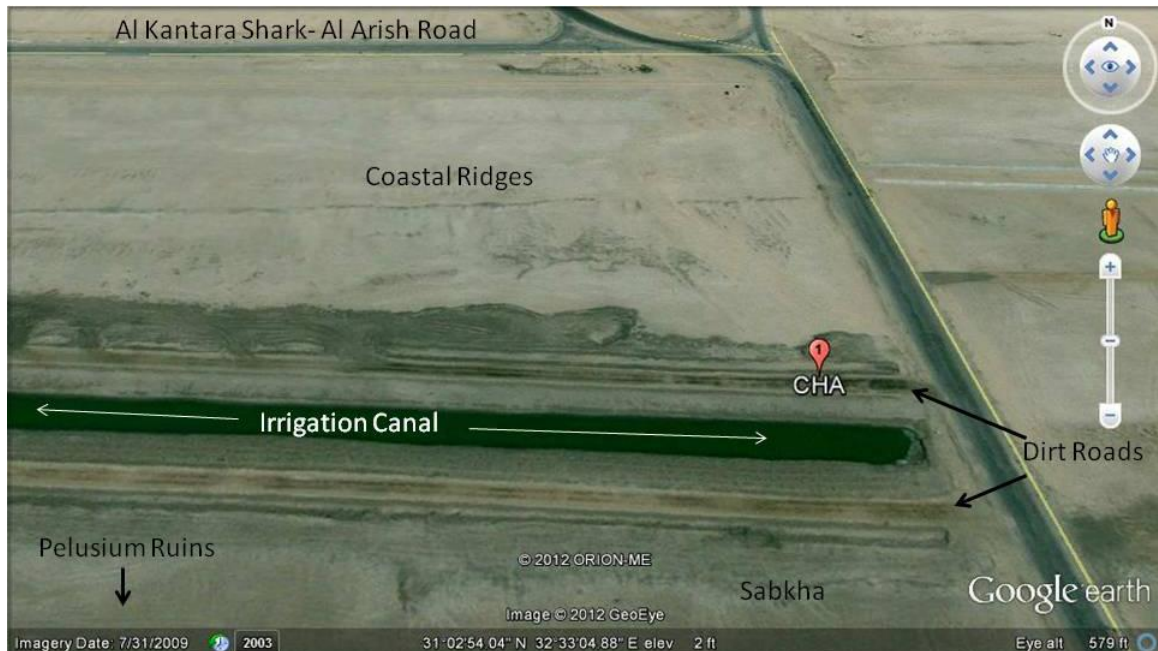


Figure 3.1: Location of measured section CHA .The measured section location is marked by the red balloon. The section was measured at the termination of an exposed length of an irrigation canal flowing west to east in the Plain of Tineh. (Background image from Google Earth image, Copyright 2012).

Samples were also analyzed and found to contain diatoms for a number of sections. Diatom identification of taxa was carried out by Dr. Abdelfattah Zalut of Tanta University, Egypt. Samples rich in diatoms were analyzed by thin section and organized based on habitat for use in interpretation of environment of deposition.

### 3.2 Stratigraphic Analysis

Four stratigraphic sections were created for the corresponding sections measured in the field. The chosen sections were measured along an irrigation canal flowing parallel to the paleo-shoreline of the Mediterranean during Roman occupation of the area prior to 25 A.D. Descriptions of the sections, observed facies and summary interpretations are discussed below.

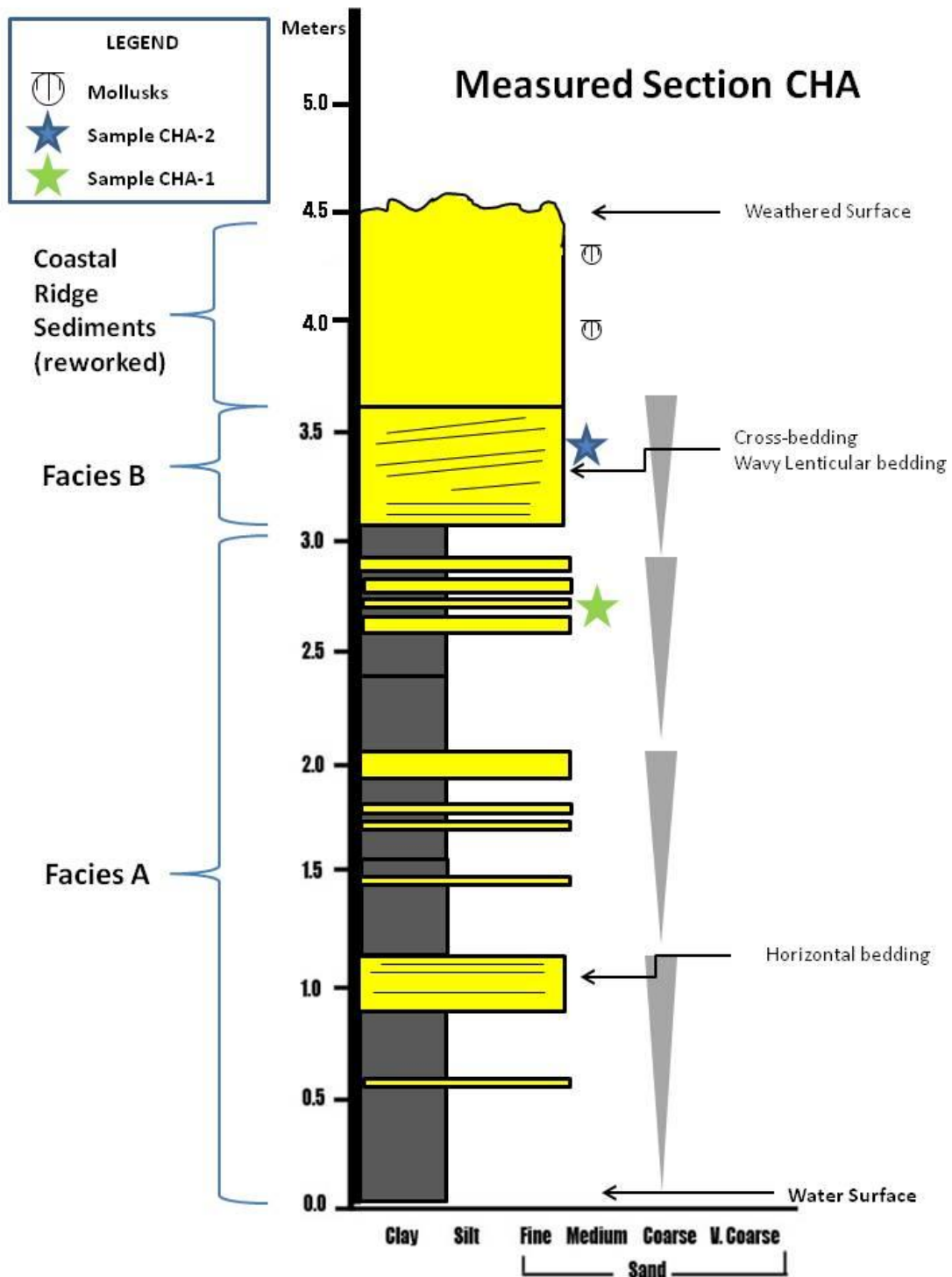


Figure 3.2: Stratigraphic columnar section for the location CHA along an irrigation canal running parallel to the Al Kantara Shark- Al Arish road.

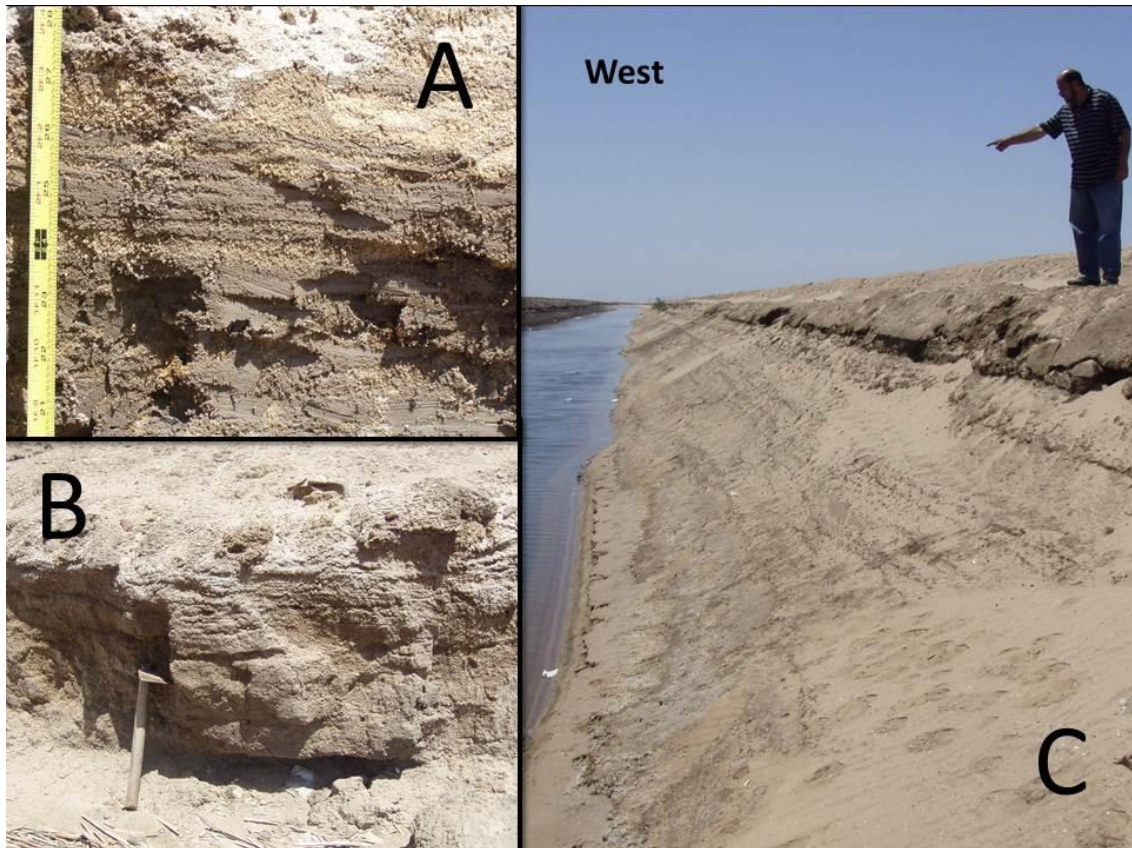


Figure 3.3: Field photographs taken at section CHA. A) Wavy and lenticular bedding were present in the upper part of the measured section. B) Thick silty mud bed at the termination of the canal. Cohesiveness of the clays allowed for better resistance against erosion in comparison to the sandy beds. C) Image of the entire measured section. Measurements were begun above the waterline and terminated below the added road gravels. (Photographs courtesy S. Sohby)

### *Section CHA*

Stratigraphic section CHA was measured north of the ruins of the City of Pelusium at  $31^{\circ} 2'53.40''\text{N}$ ,  $32^{\circ}33'7.16''\text{E}$  (Fig. 3.1) and located north of the borehole section (S-19) of Stanley et al. (2008) (shown in Figure 3.2). Measurements were taken from above the water line of the canal to just below the non-local road gravels.

Description: The measured section was 3.6 meters and consisted of three upward-coarsening successions (Figure 3.2). A meter of reworked sediments from the

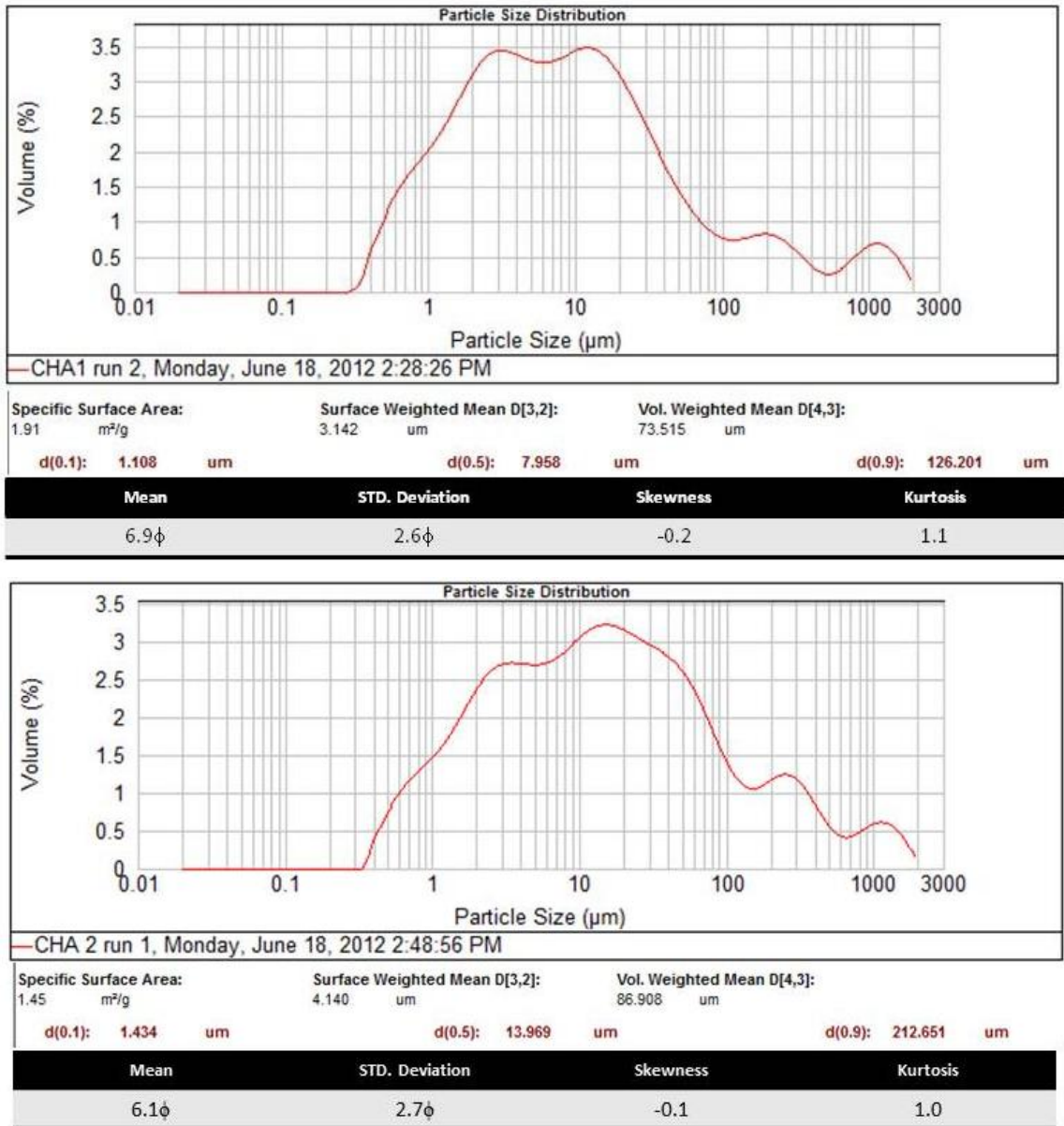


Figure 3.4: Particle size distribution by volume is shown graphically for sample CHA-1 and CHA-2. Statistical derivations including weighted means and graphic mean, standard deviation and skewness and kurtosis values displayed beneath their respective graphs. Similar graphs with statistical derivations were created for the analyzed samples collected at the various measured sections.

construction of the road overlies the measured section in this area. Mud beds beginning at the canal water base are overlain by coarser-grained sand beds 10- 30cm thick (Figure 3.3). Sands were well- sorted, fine- to medium-grained and tan yellow (10 YR 6/6) in

color. Most sand beds were massive and horizontally bedded and contained dark magnetic grains. The upper part of the measured section showed lenticular to wavy bedding sedimentary structures. Intercalated sand beds ranged in thickness from 7cm to 13cm. The section was capped by a sandy bed with cross-bedding. The silty mud clays are a dark brown (Munsell Color Index, 10 YR 5/3). Some of the muds contained <1cm wide fine-grained shelly laminations. The poor preservation prevented identification of shell debris for mollusk faunas but studies conducted in the area have found *Donax semistriatus*, *Maetra* sp., and *Solen* species (Stanley et al. 2008). Clay beds show a high concentration of crystallized evaporites, mainly halite, along exposed faces.

Grain Size Analysis: Two samples were collected in section CHA. These are CHA-1 and CHA-2 that correspond to the muddier components of the facies. Grain size analysis results using Laser Particle Size Analysis (LPSA) showed textural assemblages of over 75% muds for sample CHA-1 (Figure 3.4). Results from the analysis for all samples are located in Appendix 1. The overall silt percentage was 50%, with 35% clay and 15% sand corresponding to silty mud (sM) in the modified Folk (1980) ternary diagram for fines. Statistical analysis showed a very poorly sorted sample with a standard deviation of  $STDV=2.6\phi$  that was also coarse skewed,  $Sk=-0.15$ . The textural composition of sample CHA-2 was distributed as 26% clay, 52% silt, and 22% sand and plotted as a sandy clayey silt (scZ) in the ternary diagram. This sample was also very poorly sorted since  $STDV=2.7$ .



Figure 3.5: Location of measured sections CHB and CHC along an irrigation canal running almost parallel to the Al Kantara Shark- Al Arish Road. The measured areas are northwest of the Pelusium Archeological area which consists of a rise surrounded by modern sabkha. The area is bounded local dirt roads with fish farm agricultural areas to the west. Modified from a Google Earth image, Copyright 2012.

### ***Section CHB***

Section CHB was measured west of section CHA, and has reference coordinates of  $31^{\circ} 2'58.23''N$ ,  $32^{\circ}31'50.82''E$  (Figure 3.5). It is located midway between the boundaries roads of the Pelusium archeological area, along the irrigation canal flowing parallel to Al Kantara Shark- Al Arish road.

*Description:* The section contained about 3.5m of fine-to medium-grained, massive to horizontally laminated sands that were locally shelly (Figure 3.6). Coarser shell debris beds reached up to 5cm wide at their maximum. The shell hash consists of angular coarse-grained shell

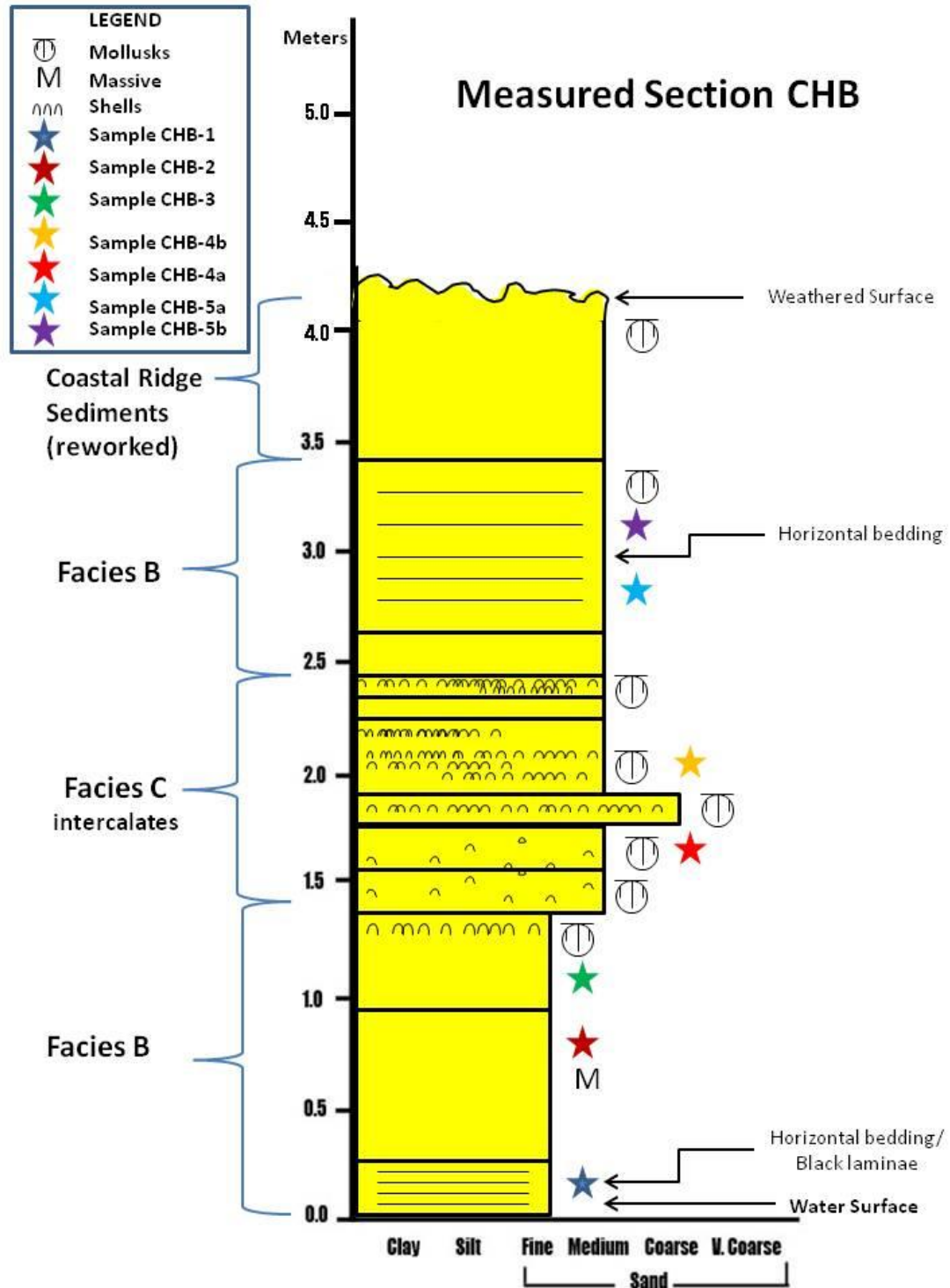


Figure 3.6: A stratigraphic section was created for the measured section in location CHB. The section contains Facies B1 and B2 which intergrades in the middle of the section. Facies C overlies these deposits. Facies B1, B2, and C have been interpreted as nearshore, beachface deposits.

fragments to whole specimens within the deposit along with quartz, feldspar, mica, hornblende and magnetite grains in the rest of the sand matrix (Figure 3.7). The two lower beds in the section were fine- and medium-grained sands ranging from dark brown to gray yellow in color. These beds were considerably heavy mineral-rich in comparison to the other beds in the section. The lowermost bed consisted of dark sand laminae and dark sand thin beds. Coarse-grained, poorly sorted, mixed mollusk angular shell hash was present within collected samples (CHB-1, CHB-2). Shell hash and shell debris beds increased in frequency in the middle of the section. Quartz-rich, medium-grained sands graded with bleached, poorly-sorted and poorly preserved, nested shell debris beds up to 5cm wide (samples CHB-3 and CHB-4a through c). These graded beds were overlain by very light, quartz-rich medium-grained sands with localized oxidation that mottled the sands a bright orange. Thin black heavy mineral laminae were observed near the top of the measured section grading into coarser-grained pebble beds of differing textural composition. All the collected samples for beds in section CHB contained magnetite grains, but these were much more concentrated in the bottom beds of the measured section.

*Mollusk Assemblages:* Overall, beds containing shell hash had poorly preserved shells, though some whole specimens were collected for beds CHB1, CHB2, CHB3, and CHB4b. The shell hash contains angular broken gastropod and bivalve shell fragments. The largest of the intact mollusks in the collected samples have a maximum length of 2.5 cm and belong to *Cerastoderma glaucum* (Bruguière, 1789) collected in the sampled shell debris bed, sample CHB-4b. They were also the best represented. Other

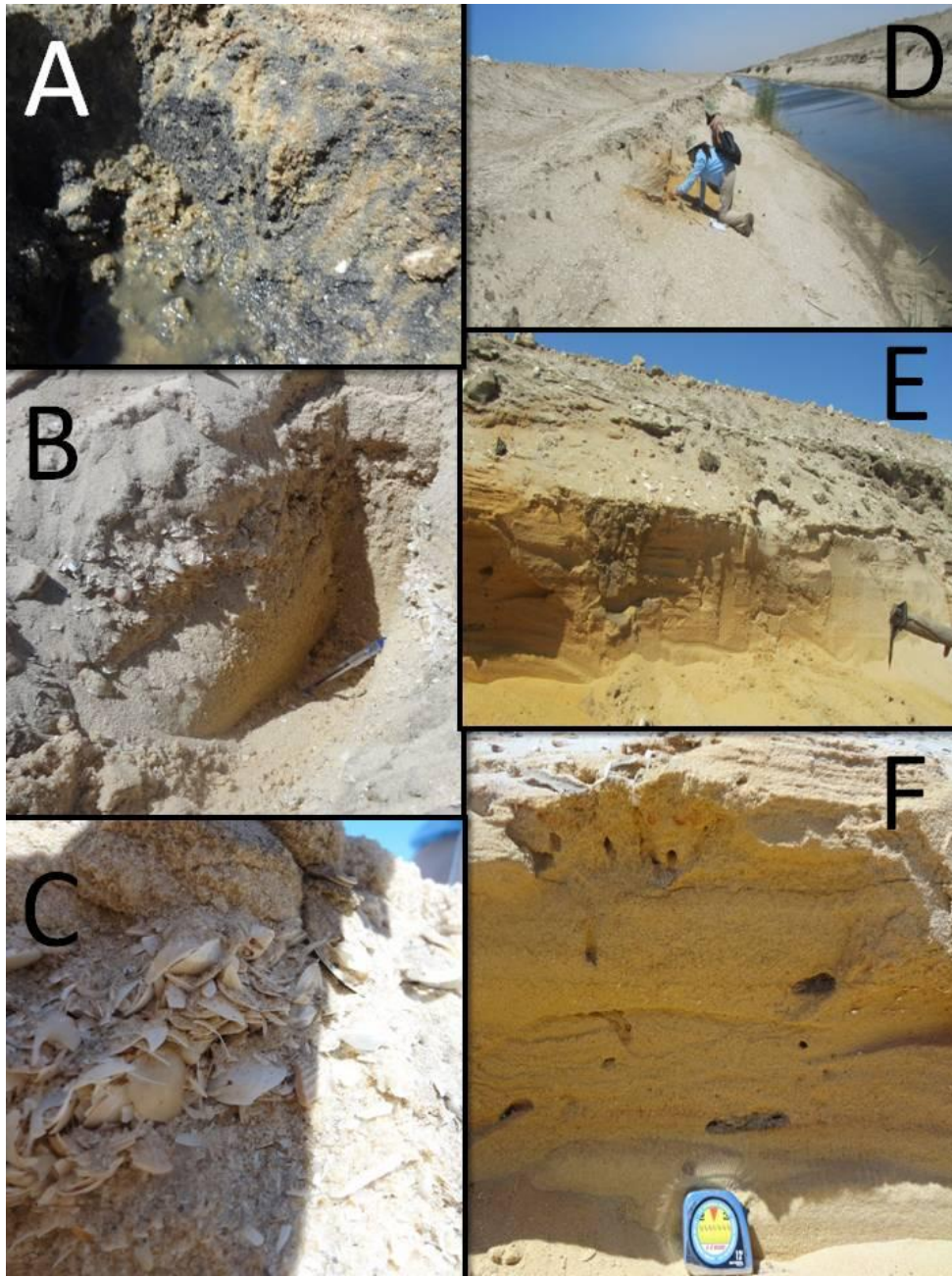


Figure 3.7: Field photographs of section CHB. A) Lowermost beds of the measured section at the water line. Fine sand beds with alternating dark light colored sands. B) Middle of the measured section showing intergrading beds of Facies B1 and B2. C) Poorly sorted, shell debris beds of Facies B2. D) View of the stratigraphic section along the canal length. E) Upper part of the studied section. The beds contain heavy mineral banding and local oxidation. F) Upper sandy beds of Facies C is well sorted and medium-grained and ranges in color from a pale tan, to bright orange due to oxidation. (Photographs courtesy J. Quintanar (B, C, E, F), S. Khan (D), M. Sobhy. (A))

mollusks in the sample include *Pirenella conica* (Blainville, 1829), *Abra* sp., *Donax semistriatus* (Poli 1795), *Mactra stultorum* (Linnaeus, 1758), *Loripes lacteus* (Linne, 1758), *Neverita\_72osephina* (Risso 1826), *Corbicula* sp., *Cyclope neritea* (Linnaeus, 1758), and *Nassarius gibbosulus* (Linne, 1758). Sample CHB1, CHB2, and CHB3 also had a varied assemblage that included many *Pirenella conica* (Blainville, 1829) and *Cyclope neritea* (Linnaeus, 1758) as well as infrequent *Cerastoderma glaucum*, (Bruguère, 1789), *Donax semistriatus* (Poli 1795), and *Mactra stultorum* (Linnaeus, 1758). The most common species in the samples are shown in Figure 3.8. The above listed specimens are from mixed environments including freshwater, brackish and marine. The mixed environments suggest re-working before deposition within the sandy beds.

Grain Size Analysis: Section CHB corresponds with collected samples CHB-1 through CHB-5b in stratigraphic section CHB. LPSA resulted in a textural assemblage of 77.8 % sand, 19.6% silt and 2.6% clay for sample CHB-1. The textural assemblage plots within the muddy sand (mS) field in the fines ternary diagram. The median was  $d(0.5)=249.2 \mu\text{m}$ . Statistical analysis showed the sample to be poorly sorted and strongly fine skewed with a standard deviation equal to 1.9 and skewness of 0.3. Sample CHB-2's textural assemblage was headed by 89% sand fraction with 8% silt and 3% clay. The median was  $181.2\mu\text{m}$ . The dominant grain size for CHB-1 and CHB-2 was fine sands as shown by a mean of  $2.7\phi$  and  $2.5\phi$ , respectively. Grain size analysis provided a textural composition for the sand fraction in CHB-3, including; 14.9% fine (F), 49.5% medium



Figure 3.8: Gastropod and bivalve samples collected from fossiliferous sands in the measured sections along an irrigation canal parallel to the Mediterranean shoreline during 25 AD. A: *Pirenella conica* (Blainville, 1829), B: *Nassarius gibbosulus* (Linne 1758), C: *Turboella similis* (Scacchi, 1836), D: *Cyclope neritea* (Linne, 1758), E: *Bornia sebetia* (Da Costa, 1829), F: *Cerastoderma glaucum* (Bruguière, 1789), G: *Donax semistriatus* (Poli 1795), H: *Loripes lacteus*, (Linne, 1758). Picture courtesy J. Quintanar.

(M), 22.6% coarse (C) and 13.0% very coarse (VC) sands. The median was  $d(0.5)=402.6\mu\text{m}$ . The sands in this sample were moderately sorted with a standard deviation of 0.9, and skewness equal to 0.3 that made it fine skewed. The section showed a coarsening upward trend from muddier sands to medium-grained sands. Sample CHB-4a's textural composition showed coarse-grained sands as the majority of the sand fraction at 49%. This was due in part to the coarser grained angular shell fragments of the sands in the middle of the section where they grade into the shell debris beds. The sands

were moderately sorted with a standard deviation of  $0.7\phi$  and a median of  $d(0.5)=580.4\mu\text{m}$  for this sample. Sample CHB-4b was collected within the thickest shell debris bed. The sand matrix is almost identical to sands sampled in Facies B1 which are intergraded with this facies. The sand was evaluated using a grain size card since the shell debris samples were not analyzed using the Malvern 2000 laser as the debris shells were too coarse overall. The sample was comprised of medium- to coarse-grained sand matrix. Sample CHB-4c tops the shell debris beds. CHB-4c had a higher percentage of medium-grained sands, with 44.8% (M) and 34.0% (C) within the textural composition. The median  $d(0.05)$  was calculated at  $364.6\mu\text{m}$  and  $327.7\mu\text{m}$  for CHB-5a, and CHB-5b, respectively. These sands were moderately well-sorted, coarse skewed medium-grained sands. The samples in the upper part of the section were primarily medium-grained. Differences between beds were related to level of oxidation staining of the sands and slight textural variations with thin <4cm thick coarser-grained beds. Samples for the facies were primarily medium-grained sands ranging from  $250\mu\text{m}$ - $500\mu\text{m}$  for all samples. Overall the facies showed coarsening-upward beds until the middle of the section, were grain-size fined to medium-grained sands.

### ***Section CHC***

Section CHC was collected west of section CHB along the irrigation canal and across from a farm road serving as the boundary between the fish farms and Pelusium archeological area at coordinates  $31^{\circ} 2'59.86''\text{N}$ ,  $32^{\circ}31'26.67''\text{E}$  (Figure 3.5).

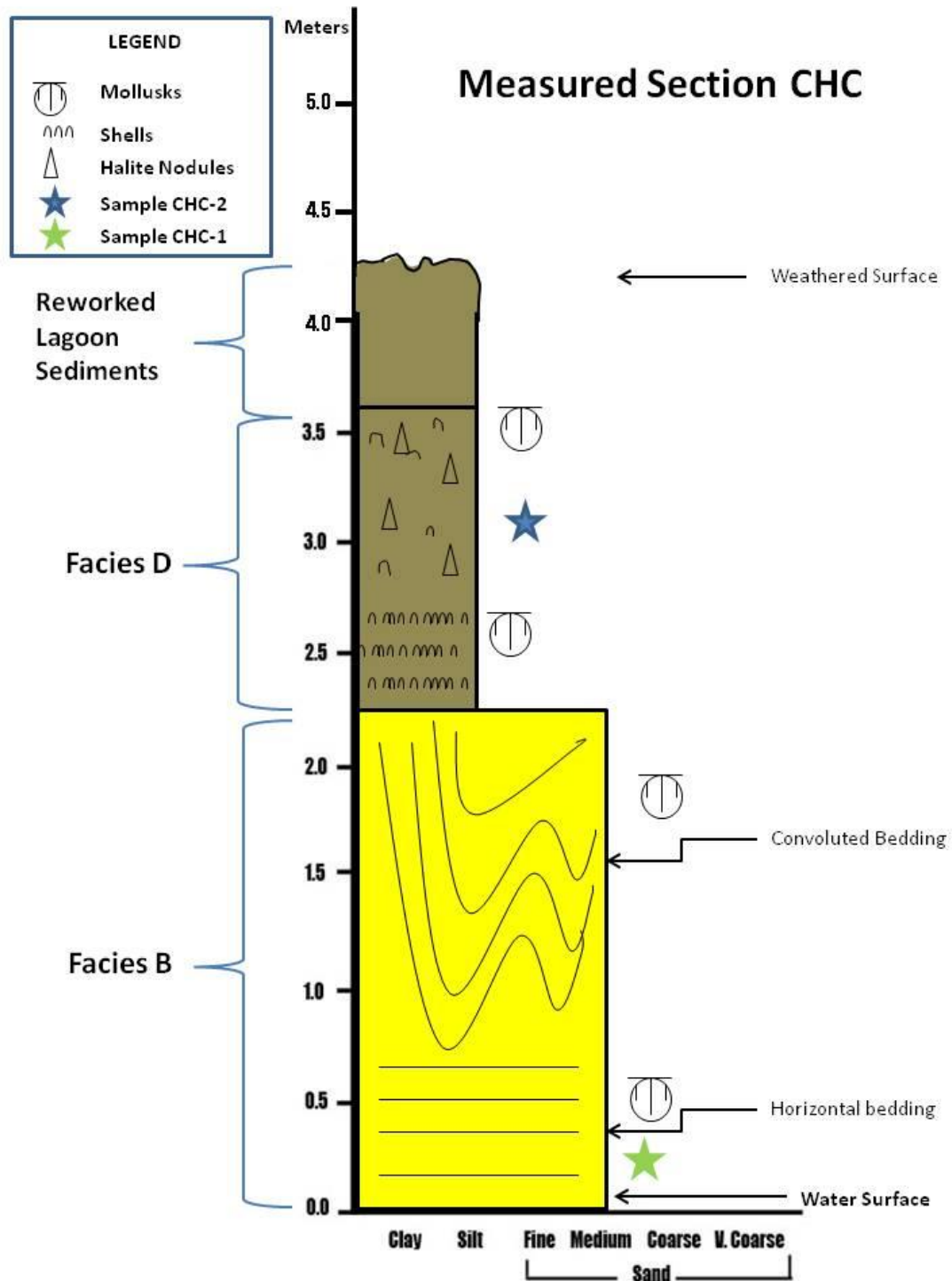


Figure 3.9: Stratigraphic columnar section for the location CHC data collected in the field. The section shows the abrupt change in facies between sandy Facies C and the shelly silts of Facies D.

Description: Section CHC is 4.3 m thick and shows a sharp transition between sand and mud beds (Figure. 3.9). The measured section is overlying by approximately 1 meter of reworked road material. The lower bed is a medium-grained, quartz-rich, shelly, light tan sand with horizontal bedding (Figure 3.10). Convolute bedding occurs below the sharp contact with the muds. The sand bed correlates to the topmost bed in section CHB. The overlying muddy bed is massive with a concentrated shell lag at the base and fossiliferous throughout. Shell fossils are moderately preserved and many shells were whole. It also contains ~5mm colorless, gypsum crystals.

Mollusk Assemblages: The shell hash in the bottom sandy bed contains poorly-preserved angular broken gastropod and bivalve shell fragments. The largest of the intact mollusks in the collected samples have a maximum length of 3 mm and belong to *Donax semistriatus* (Poli 1795) in sample CHC-1. The sample also had *Maetra stultorum* (Linnaeus, 1758) and both species of mollusks were commonly found in the sandy sample. The highly fragmented shell hash for the sandy bed indicates reworking by waves, instead of deposition *in-situ*. Furthermore, the assemblage for the sandy bed included both lagoonal and nearshore marine environments of deposition. Identified shells in sample CHC-2 include *Donax semistriatus* (Poli 1795) and *Cyclope neritea* (Linnaeus, 1758). The mollusks in the muddy bed are more likely to have been deposited *in situ* due to their high level of preservation of the shells. Both the mollusk and gastropod species observed prefer saline environments, though the mollusk prefers sandy beaches and the gastropods indicate a saline lagoon or estuary environment.

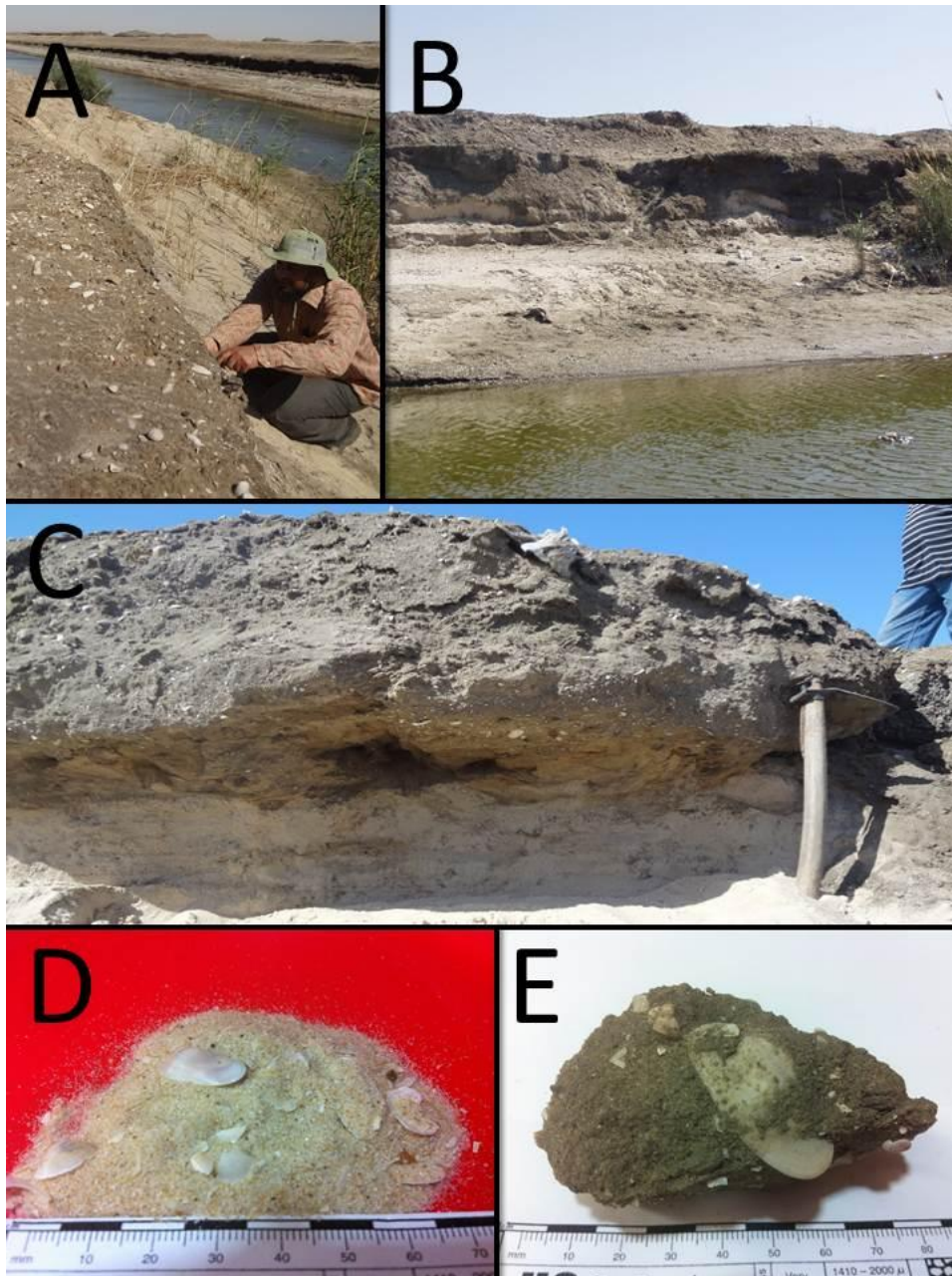


Figure 3.10: Field photographs of section CHC. A) Dark shelly silts overlie loose tan sands. Bivalves reach maximum lengths of 3cm. B) View across the canal. Overlying shelly silt beds are thicker on the opposite side of the canal. C) Overhanging bed of shelly silts overlies sandy beds showing convoluted bedding. D) Sediment sample, CHC-1 of the lower shelly sand bed corresponding to Facies C. E) Collected sample, CHC-2 containing large bivalve. Even dry, sediment holds well together. (Photographs courtesy J. Quintanar (C, D, E), and S. Khan (A, B) .



Figure 3.11: Location of the westernmost section CHD along an irrigation canal parallel to Al Kantara Shark- Al Arish Road. Measured section location is shown by the red ballon. (Modified from Google Earth image, Copyright 2012.

Grain Size Analysis: Sample CHC-1 was collected from the lower sandy bed with convoluted bedding. The textural composition was made up wholly of sands with the sand fraction divided into 21% fine, 63% medium, 15% coarse, and 1% very coarse. The bed was overall, medium-grained sand with a graphic mean of  $1.6\phi$  and moderately well sorted with a graphical standard deviation of  $0.5\phi$ . The median for the volume distribution is  $d(0.5)= 336.4\mu\text{m}$  and the calculated volume and surface weighted means are  $D[4,3]=372.4 \mu\text{m}$  and  $D[3,2]=319.5\mu\text{m}$ . Sample CHD-2 plotted as a clayey sandy silt (csZ) within the revised Folk (1980) diagram. It has a textural composition of clay=14%, silt=55% and sand=31%. The sample was very poorly sorted with a graphical standard deviation of  $2.4\phi$ . The graphic mean was  $4.97\phi$  which corresponds to an overall representative size of coarse silt.

### ***Section CHD***

Section CHD was the westernmost measured section, and nearly midway between the boreholes (S-12 and S-19) sections of Stanley et al., (2008). The section is located from the first crossover bridge across the irrigation canal running parallel to Al Kantara Shark Al Arish road and was measured along the irrigation canal at coordinates 31° 3'8.16"N, 32°29'58.93"E (Figure 3.11).

*Description:* The measured section was 3.6 m along the exposed face of the canal wall and is overlain by a meter of reworked material for the road base (Figure 3.12). Section CHD contains massive to laminated silt beds (Figure 3.13). The color ranges from gray (5 YR 4/2) clays to brown (10 YR 5/4) sandy silts when dry. Textural variation is common with beds ranging from clayey silt, clayey sandy silt, sandy clayey silt and sandy mud. Sediment hardness varies for the clays and ranges from medium to stiff. The stiffer, more cohesive clays are more resistant to erosion and protrude from neighboring beds. The two bottommost beds consisted of dark brown sandy muds with common circular oxidation mottling with diameters no wider than 2mm. Shell fragments were infrequent and beds consisted of clays with medium hardness. The second bed contained "coffee grounds" plant debris and prevalent mud cracks. Samples CHD-1 and CHD-2 were collected from the first and second measured beds, respectively. These were overlain by a coarser grained bed of grey clayey silt. It was fossiliferous and contained broken shell fragments ranging from 1mm to 30mm in length for whole bivalve shells.

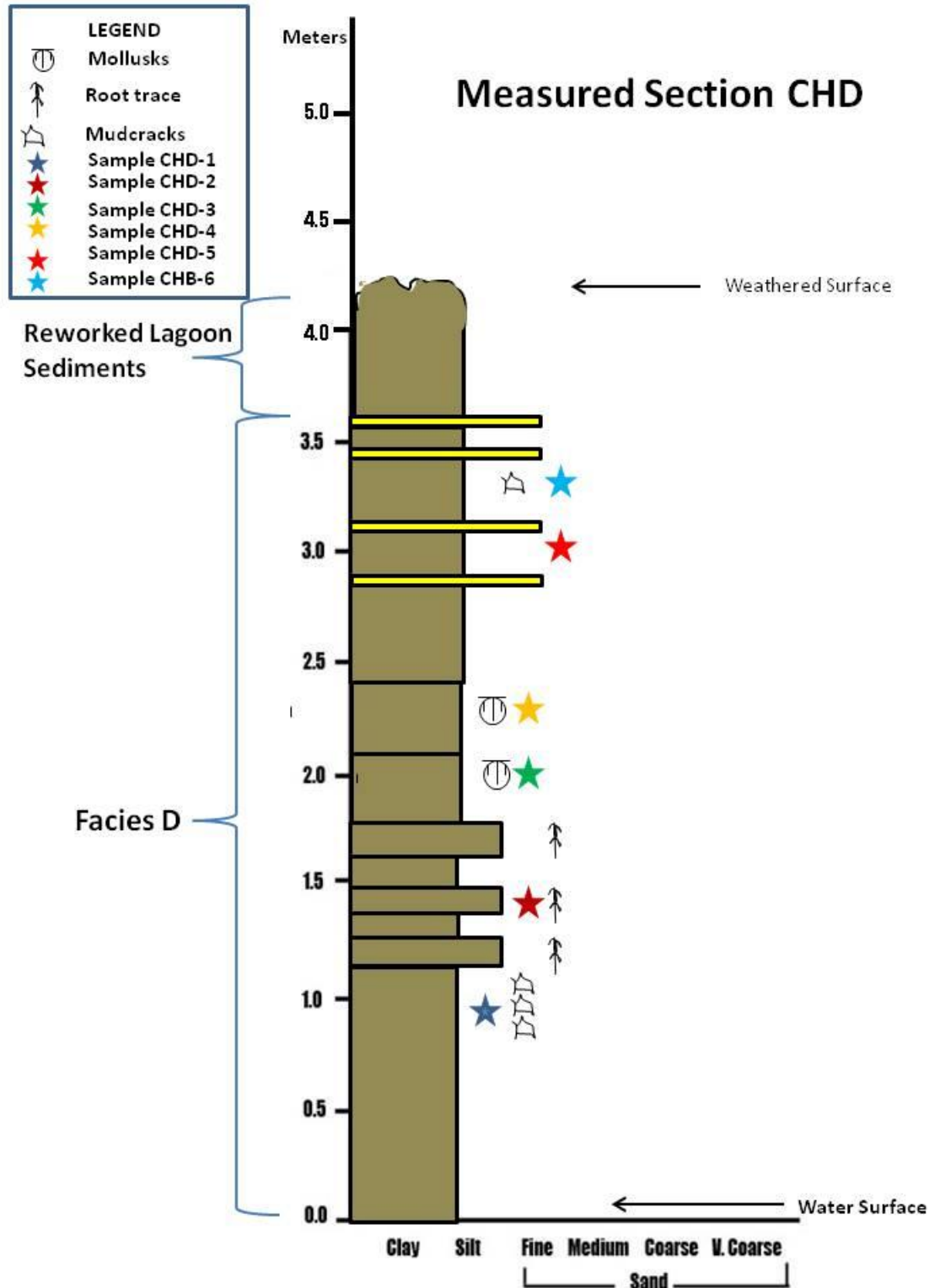


Figure 3.12: Constructed stratigraphic section of measured location CHD. The section consisted of beds belonging to Facies D of lagoon deposits.

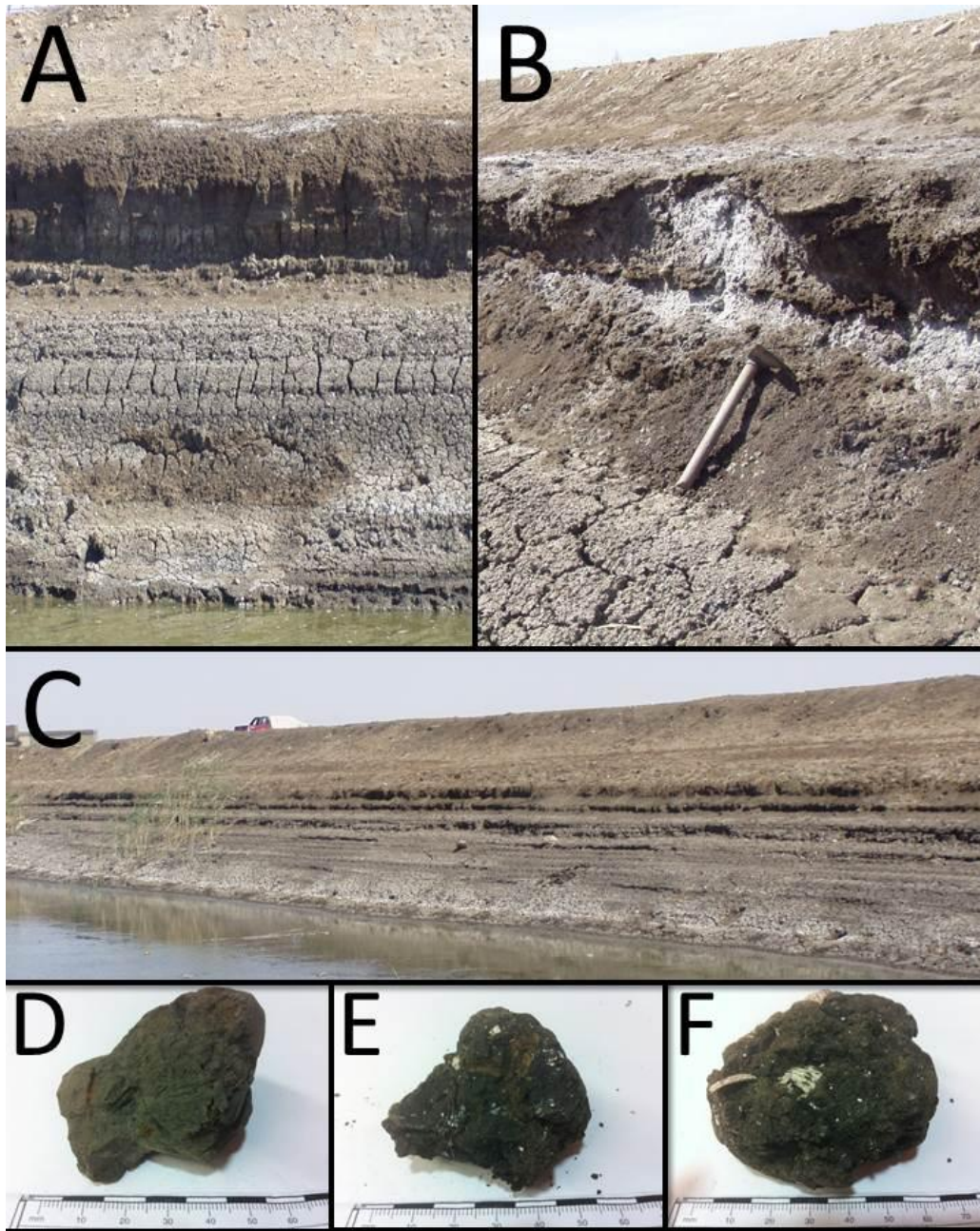


Figure 3.13: Field photographs of section CHD. A) Measured section at location CHD consisted of fine to medium silts of varying compositional textures including sandy and clayey silts and muddy sands. Mudcracks were common in these deposits. B) Halite evaporites were pervasive along exposed surfaces of the more clay-rich beds, particularly in the upper beds of the section. C) View of section CHD across the canal. Some contained more cohesive sediments than their neighbors. D) Sediment sample CHD-2 shows root traces and oxidation mottling. E) Sediment sample CHD-4 shows oxidation mottling, shells and root traces. F) Sediment sample CHD-3 is very shelly and contained well preserved bivalve shells. [Photographs courtesy M. Sobhy (A, B, C) and J. Quintanar (D, E, F).]

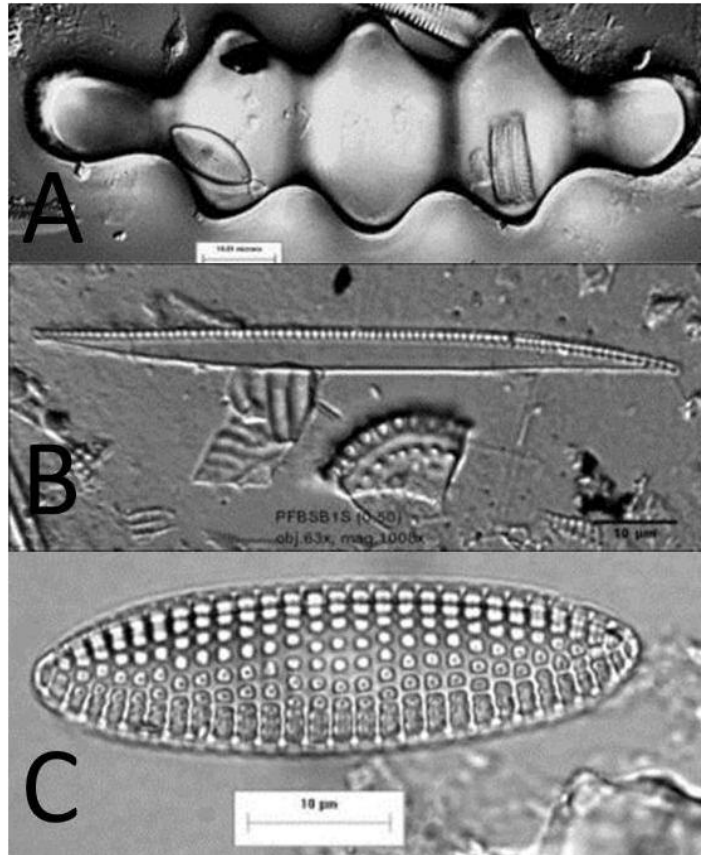


Figure 3.14: Three different taxa of diatoms commonly found within samples of section CHD. A) *Terpsinoë musica*. B) *Nitzschia sigma*. C) *Tryblionella granulate*. Images courtesy Florida Coastal Everglades Longterm Ecological Research.

Root trace disruption was minimal, but was oxidized along the traces. Muds contained thin <2cm light brown silt laminations within the soft clays. Sample CHD-3 was collected from this bed. Sandy clayey silts were deposited above the previous beds. Silt and soft clay are intercalated in this bed. Shell fragments were minimal and whole bivalve shells had a maximum length of 10mm. Sample CHD4 was collected from the sandy clayey silt bed. Sample CHD-5 was collected from the coarser grained overlying sandy mud. It also contained horizontally laminated intercalations of sand and soft silty clays. This bed was not fossiliferous and contained pervasive salt crystallization and

mudcrack disruptions along exposed faces. The measured section was capped by a sandy clayey silt, dark brown in color that contained considerable salt crystallization and lacked shell fossils. Sample CHD6 was collected from the cap bed.

Mollusk Assemblages: The silts of section CHD contained only bivalve mollusks of species *Cerastoderma glaucum*, (Bruguière, 1789). The shells were present in the younger beds within samples CHD3 and CHD4. The shells were very well preserved and a bright white color. Sample shells of whole specimens were measured and the largest examples had a maximum length of 2.5 cm. *Cerastoderma glaucum* bivalves are indicative of saline lagoons or estuary environments with soft sediments for the mollusks to burrow. The well preserved *C. glaucum* shells and single species represented in the bed suggest local derivation of shells instead of reworking and subsequent post-deposition.

Diatom Assemblages: Beds within section CHD were analyzed for diatoms and beds corresponding to samples CHD-1 through CHD-3 were diatom-rich. Fourteen different taxa were identified as commonly occurring within samples CHD-1 and CHD-2 and frequently occurring in CHD-3. The majority of the taxa live in brackish environments, though freshwater and/or marine environments were also represented. Prevalent taxa included: *Campylodiscus bicostatus*, *Campylodiscus clypeus*, *Diploneis bombus*, *Epithemia adnata*, *Hantzschia virgata*, *Navicula aegyptiaca*, *Nitzschia sigma*, *Nitzschia sigmoidea*, *Synedra ulna*, *Tabularia fasciculate*, *Terpsinoë Americana*, *Terpsinoë musica*, *Tryblionella granulate*, and *Tryblionella levidensis*. The observed taxa indicate growth within a quiet-water environment such as lacustrine, with warm, brackish water conditions and moderate alkalinity (Dr. A. Zalut, personal communication, October

11, 2012).

Grain Size Analysis: Measured section CHD corresponds to collected samples CHD-1 through CHD-6. Textural variation was common among the silt beds. The sandy mud (sM) beds were located at the base and near the top of the stratigraphic section (CHD-1, CHD-2, CHD-5). Sample CHD-1 had a textural composition containing 29% clay, 50% silt and 21% sand. It was very poorly sorted with a graphical STDV= 2.7 $\phi$  and the main representative size was 6.3 $\phi$  which corresponds to fine silts. The sample data were coarse skewed (Sk= -0.1771). Sample CHD-5 was similar with a textural composition of 27% clay, 47% silt and 25% sand and sample CHD-2 contained 19% clay, 52 % silt and 28% sand. The samples were very poorly sorted fine- and medium-coarse silts respectively, though skewness was near symmetrical for both. Sample CHD-3 consisted of 26% clay, 70% silt, and 3% sand and plotted as a clayey silt (cZ) in the revised Folk (1980) ternary diagram for fines. The sample contained very fine to fine silts (Graphic Mean= 5.99 $\phi$ ) that were poorly sorted (graphical STDV=1.68 $\phi$ ). The sample was fine skewed with a skewness value of Sk= 0.11. Sample CHD-4 plotted as a clayey sandy silt with a textural composition of 22% clay, 63% silt and 15% sand. The dominant grain size was fine silt (graphic mean= 4.59 $\phi$ ) that are very poorly sorted (graphical STDV=2.4). Sample CHD-6 was a sandy clayey silt with a textural composition of 27% clay, 52% silt and 21% sand. Fine silts (graphic mean= 6.15 $\phi$ ) were the predominant grain size and the sample was overall very poorly sorted (graphical STDV=2.59). Beds overall coarsen-upward in measured section CHD and showed a dominant grain size trend toward fine silts.



Figure 3.15: Location of TEF samples in relation to measured sections CHA-CHD near the Pelusium Ruins in the northeastern Plain of Tineh. (Modified from a Google Earth image, Copyright 2012).

### ***Section TEF***

Section TEF was trenched, so a stratigraphic section was not created.

Description: TEF samples were collected by shallow trenching in the sabkha plain west of the Pelusium City ruins. Four samples were collected (TEF 1-4) at spaced intervals. Sample TEF 3 for example was located at coordinates  $31^{\circ} 2'25.83''\text{N}$ ,  $32^{\circ}31'37.94''\text{E}$  (Figure 3.15). Section TEF lies due south of measured section CHC, which marks the transition zone between eastern sand and western muds. The collected samples were all sandy muds, dark brown in color, with no shells and medium to stiff clay hardness. The samples showed hard, halite crystallized crusts (Figure 3.16).

Grain size analysis: The TEF samples were all sandy muds (sM) as plotted in the ternary diagram and contained textural compositions of very similar proportions for fines.

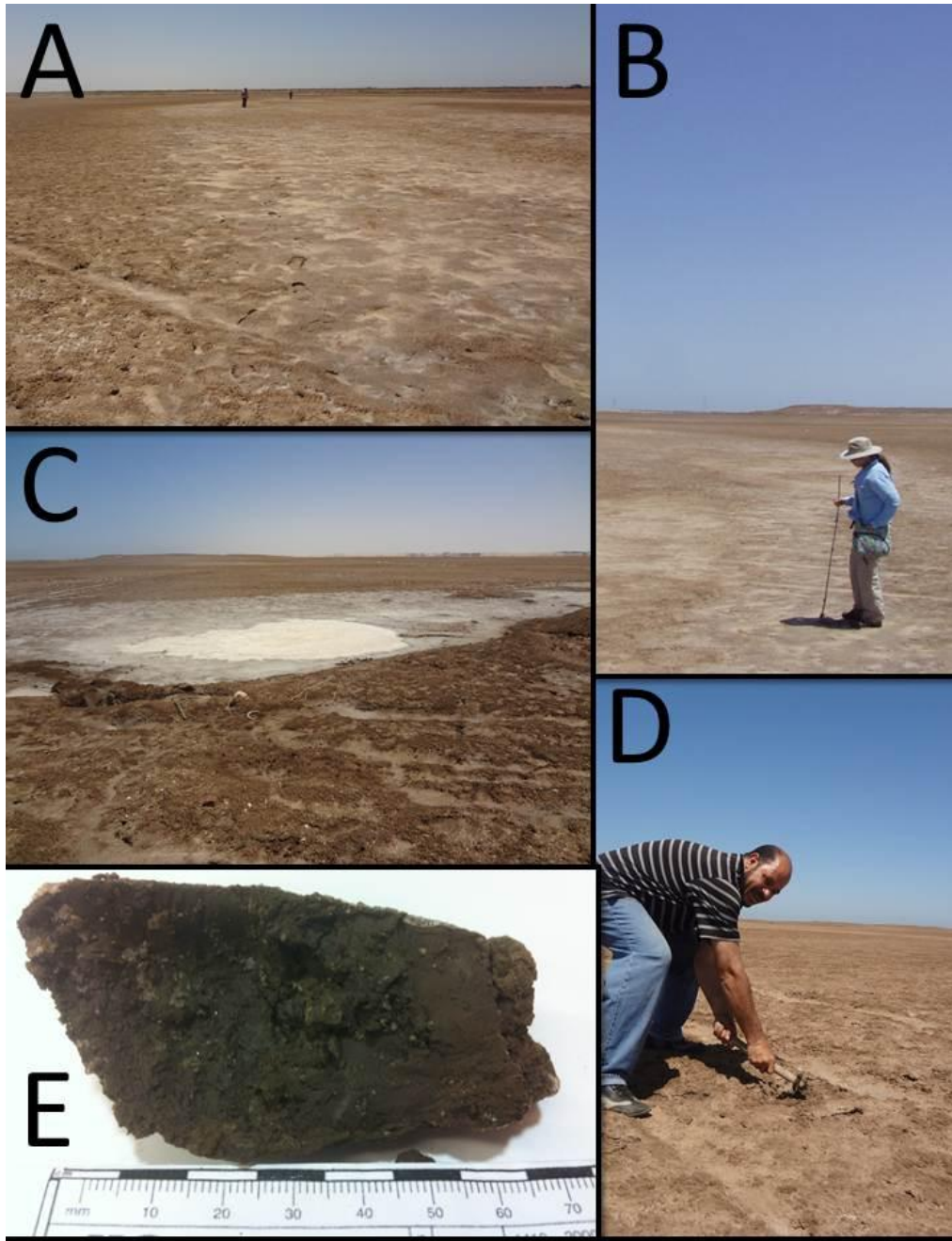


Figure 3.16: Field photographs taken at location TEF. A) The archeological plain surrounding the Pelusium ruins topographical high. Areas of lower elevation within the plain show differences from the surrounding substrate including greater evaporite deposits. B) The depression is a linear feature that splits into two and curves to surround the Pelusium ruins. C) Modern sabkha near the boundary road to the agricultural farms. D) Samples were collected by trenching below the sabkha sediments. E) Sample TEF-3 consists of stiff sandy muds. [Photographs courtesy J. Quintanar, (A,C, D, E); and S. Khan (B).]

Sample TEF 3 will be reported here. The sample contained 25% clay, 49% silt, and 26% sand. The predominant grain size for all samples was fine silt with very poor sorting (graphical STDV for all samples was greater than  $2.7\phi$ ). All samples, bar TEF1, were coarse skewed. Statistical derived values including STDV, Sk, and Rku are presented in the grain size analysis appendix along with graphed particle size distribution for all samples in section TEF.

### **3.3 Lithofacies Analysis**

Four different lithofacies were identified within the observed sedimentary succession in the northeastern Plain of Tineh. The lithofacies are described and interpreted as follows: Facies A- Subtidal Flat, Facies B- Foreshore Sands, Facies C- Beachface Shell Deposit, Facies D- Lagoon Silts. Table 3.1 portrays the identified lithofacies, summarized descriptions and interpreted environments of deposition.

#### ***Facies A (Subtidal Flat)***

Facies A consists of coarsening upward silty mud beds and sands. Sedimentary structures included lenticular and wavy bedding of sands and muds in beds ranging from 3 to 25mm in width and cross-bedding of sands. The silty mud clays are a dark brown (Munsell Color Index, 10 YR 5/3) while sands are a medium tan (10 YR 6/6). Crystallized halite evaporites were common on clay beds. Section CHA is interpreted as belonging to Facies A except for the upper laminated sand section.

***Interpretation:*** Facies A is indicative of a subtidal flat environment. It shows both wavy lenticular bedding as well as cross-bedding sedimentary structures. Broad tidal flats

<b>Facies</b>	<b>Lithology</b>	<b>Sedimentary structures</b>	<b>Interpretation</b>
A	Coarsening upward silty mud beds and sands; halite	Wavy and lenticular bedding, cross-bedding	Tidal Flat Deposits
B	Moderately-sorted, fine-to medium-grained, quartzose –rich sands; textural variation; locally oxidized; heavy mineral banding; some shells	Horizontal laminations, convolute bedding gradational with C	Foreshore Sands
C	Shell debris beds; bivalves and gastropod shells, extremely poorly sorted; medium- to coarse-grained tan sand matrix	Massive, gradational with B	Beachface Shell Deposits
D	Massive to very thinly (~ 1mm) laminated sandy silts with some clay intercalations; Fe mottling, root traces; halite and gypsum	Massive to planar laminated	Lagoon deposits

Table 3.1: The table shows the facies names, their respective lithologies and present sedimentary structures, if any. Furthermore, it includes the interpreted environment of deposition for each of the chosen facies present in the study area.

commonly show intercalating sands and muds with flaser or lenticular bedding, and cross bedding is the most common sedimentary structure (Galloway and Hobday, 1996). Lenticular bedding often occurs in tidal flats due to alternating current flow. Sands are often deposited by wave action, while mud beds are emplaced during slack water conditions. Tidal flats may show coarsening-upward progressions (Boggs, 2001). Salt crystallization was present within the recovered samples and mudflats often show salt crystallization disruptions (Galloway and Hobday, 1996). The lack of mudcracks suggests that the samples were not sub-aerially exposed, supporting a subtidal environment of deposition.

***Facies B (Foreshore sands)***

Facies B consists of fine-to medium-grained, planar-bedded, quartzose –rich sands. These varied in color from grayish tan (10 YR 6/6) to light tan (7.5 YR 7/6). The facies beds are horizontally bedded. Convolute lamination was present locally (Figure 3.17). Textural variations are present with fines grading into coarser thin bed deposits no greater than 4cm wide. Heavy mineral banding is also present as horizontal laminae < 10mm wide within the otherwise quartz-rich sands (Figure 3.18). Magnetite grains are present within the sands. Locally, sands are oxidation-stained to a bright orangey-yellow (7.5 YR 7/8). The sand deposits were commonly shelly where the facies intergrades with Facies C. The shell hash consists of angular coarse-grained shell fragments. Facies B is gradational with Facies C and shows inverse grading with coarser quartzose-rich sand. The facies is located within measured stratigraphic section CHB and the upper most part of the CHA section and lower part of the CHC section.

*Interpretation:* Facies B is interpreted as beachface deposits. Foreshore sediments are typically fine to medium-grained sands though coarser grained pebbles as lenses or layers are also common. Heavy mineral laminae alternating with coupled sand are also common due to stronger storm swash, among other factors (Galloway and Hobday, 1996). The thin parallel laminae found within the facies are indicative of swash-backwash flow in the foreshore. Inverse grading is often present in these deposits, with fines coarsening upward into more quartz-rich sands (Boggs, 2001; Galloway and Hobday, 1996). Parallel lamination, heavy mineral laminae and coarser pebble layers are all present in Facies B. The dark-orange sands were stained from localized Fe-oxidation. Convolute lamination occurs in Facies B deposits due to plastic deformation of partially liquefied sediments credited to breaking waves within the beachface deposits of this facies (Boggs, 2001). The present magnetite grains are also indicative of the foreshore as they are commonly found in beach placer deposits.

***Facies C (Beachface Shell Deposits)***

Facies C consists of poorly- sorted very coarse shell debris beds within a well-sorted, medium- to coarse-grained sand matrix. The sand matrix is well-sorted with medium- to coarse-grained rounded grains and a tan yellow (7.5 YR 8/6) color with mostly abraded shell hash. The sand compositional assemblage is quartz-rich, although heavy minerals are present within the sand matrix, including magnetite grains. The shell debris beds ranged in size from 2cm to 5cm thick. This facies occurs in measured section CHB. Facies C is interbedded with Facies B.



Figure 3.17: Convoluted bedding in a sandy bed of Facies C. Convolute bedding often forms irregular small scale anticlines and synclines as observed in this image from an irrigation canal in the Plain of Tineh.

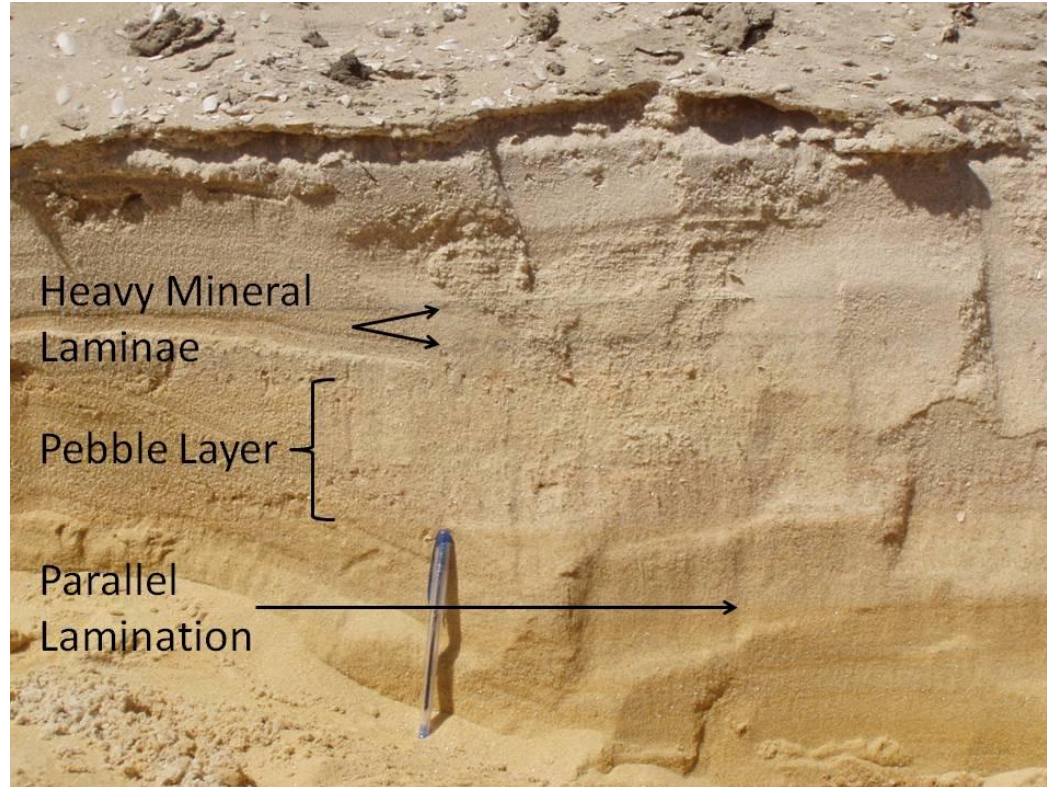


Figure 3.18: Foreshore laminated sands of Facies C showing parallel lamination, textural variation, and heavy mineral laminae in well-sorted, fine- to medium-grained sand. (Photo courtesy J. Quintanar)

*Interpretation:* Shell debris thin beds and lenses may be observed in beachface deposits (Galloway and Hobday, 1996). The poorly sorted, mixed environment shell debris beds of Facies C are indicative of a high-energy beachface environment. The poor sorting and angular shell fragments observed in the shell debris beds are due to shell breakage from reworking of sediment in the high-energy swash zone (Boggs, 2001). The gastropod and bivalve mollusks in the shell hash correlate to both marine, freshwater and brackish environments. The presence of all three assemblages suggests redistribution and post-deposition of the shells since it's unlikely for the assemblage to be found together under normal conditions. Reworking of the sand and shell hash is attributed to reworking by waves in a high-energy coastal marine environments such as the foreshore.

***Facies D (Lagoon Deposits)***

Facies D consists of massive to very thinly (~ 1mm) laminated silts. The brown (10 YR 5/4) laminated silts are often intercalated with finer grey (5 YR 4/2) clays. Textural composition varies and beds include clayey silt, sandy mud, clayey sandy silt and sandy clayey silt. Clay content hardness varies from medium to stiff. Infrequent fossiliferous beds frequently contained well-preserved mollusk and gastropod shells. Mudcracks and salt crystallization disruptions were common along exposed faces. Oxidation mottling, woody plant material, and root trace disruptions were more infrequent. Colorless gypsum crystals, < 5mm in size were also infrequent, and commonly found in only one bed. The TEF samples showed a richer brown color (7.5 YR 5/4). Facies D is observed in the upper part of stratigraphic section CHC and entire section CHD (Figure 3.19).

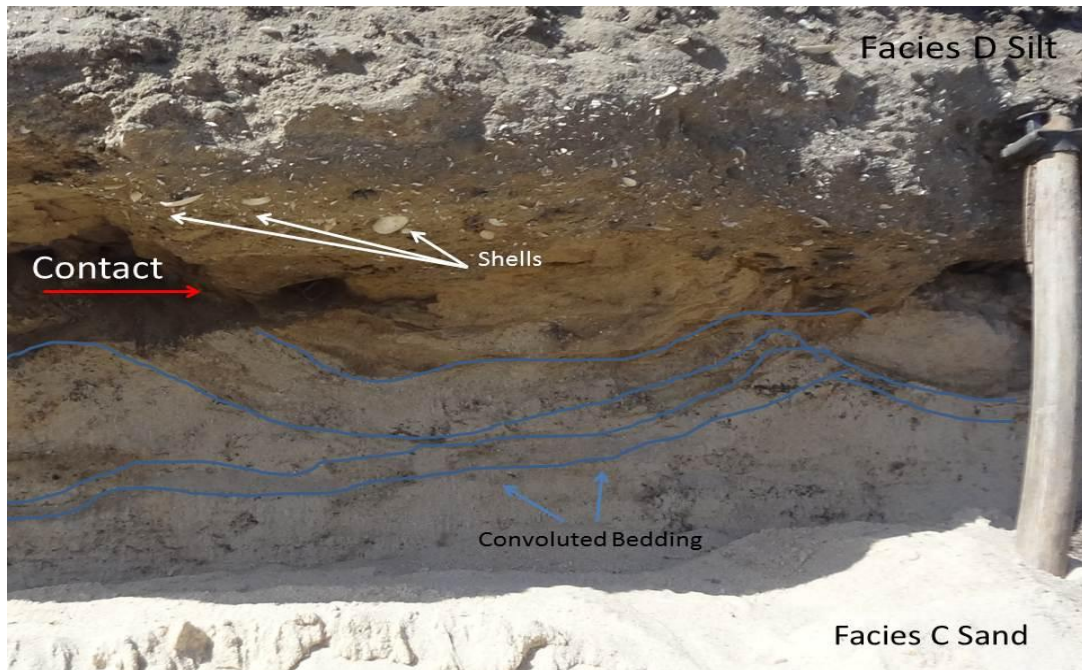


Figure 3.19: Transition between Facies C and Facies D that were interpreted as beachface and lagoon deposits, respectively. Facies C is a well-sorted, medium-grained sandy facies containing convoluted bedding. It is sharply overlain by a shelly, dark silt bed. (Photographs courtesy J. Quintanar)

Interpretation: This facies was interpreted as indicative of a lagoonal environment. Lagoons are commonly low-energy water environments. Exceptions include areas of intruding tidal inlets. Deposited lagoon sediments are primarily composed of fine-grained deposits with coarser sand beds confined to tidal inlet and related feature deposition. Muds and thin sand and silt intercalations are often deposited in the lagoon bottom and mollusk shell fragments are common within deposits as observed in Facies D (Boggs, 2001; Galloway and Hobday, 1996). The mollusk shells identified from this facies are also indicative of a brackish lagoon environment. The thin sandy laminae intercalated with muds are indicative of deposition due to wind or storm influences blowing sand into the lagoon body. Sedimentary structures include horizontal

lamination, but sediments may be massive. The observed mudcracks are indicative of changing water conditions and lagoons may show evaporite deposition and Facies D contained both salt crystallization and gypsum crystals (Boggs, 2001). Diatom taxa were indicative of brackish water environments, which occur in mixing zones for some lagoons. The clay beds contain mottled orange-yellow mottling which is indicative of localized re-oxidation of ferrous salts within the sandy silt. This type of re-oxidation occurs along well aerated paths and is associated with root traces, bioturbated burrows, or mudcracks related to changing moisture conditions (Galloway and Hobday, 1996). As the soil is exposed to air, the iron oxidizes creating typical yellow to red mottling. Facies F1 contains root traces and large polygonal mudcracks that would provide these aerated pathways for soil oxidation and may be found in quiet environments like lagoons.

### **3.4 Bivariate plots for grain-size analysis**

Bivariate plots were created to graphically describe the sedimentary characteristics of the collected samples based on the three main environments of deposition: tidal flat, beachface, and lagoon (Figure 3.20). Statistically derived standard deviation and skewness as well as graphic mean in phi ( $\phi$ ) were utilized to observe possible trends. Tidal flat deposits were shown to have similar characteristics to the lagoon deposits. Standard deviation vs. skewness shows these sediments to be extremely poorly sorted with a dominant near symmetrical skewness, though some were coarse skewed. Beach deposits were also preferentially near symmetrical in terms of skewness with moderately well-sorted grains.

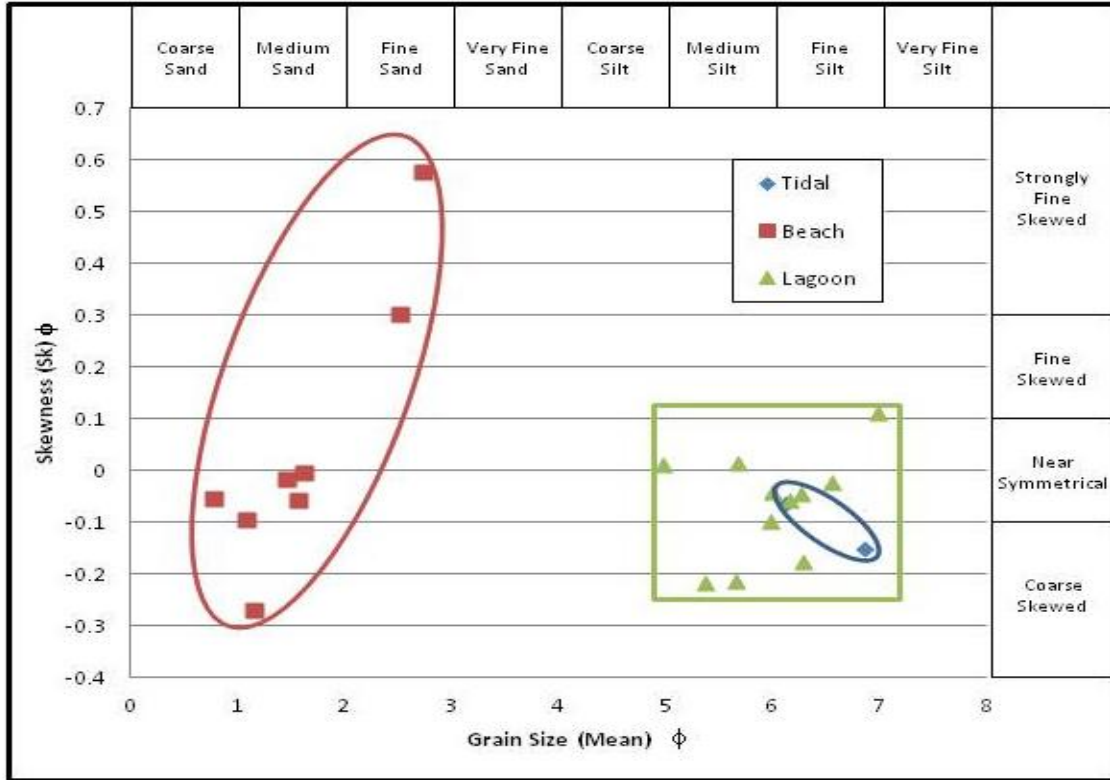


Figure 3.20a: Bivariate plots created to describe sedimentological characteristics of the interpreted environments of deposition including tidal flat, beachface, and lagoon using the collected samples from the measured sections. (a) compares skewness vs grain size. Fields were added as a comparison aid between the three types of environments.

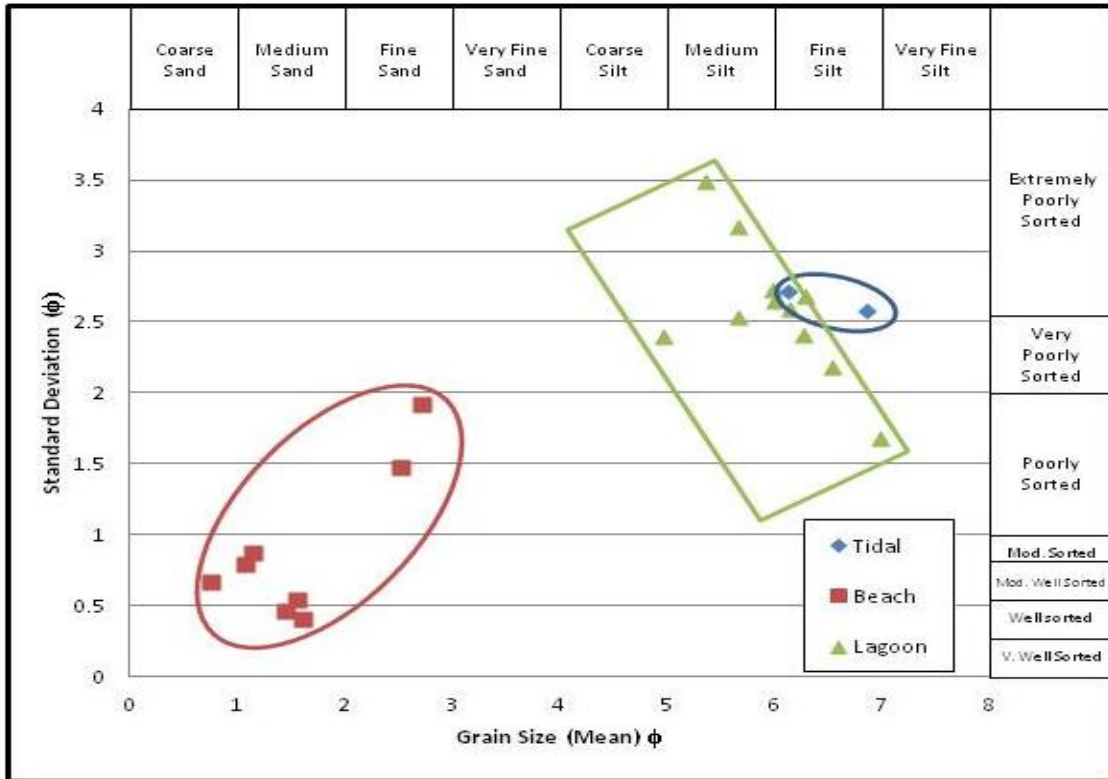


Figure 3.20b: Bivariate plot comparing standard deviation to grain size for three different observed facies in the field; tidal flat, beach and and lagoon. Fields were added as a comparison aid between the three types of environments.

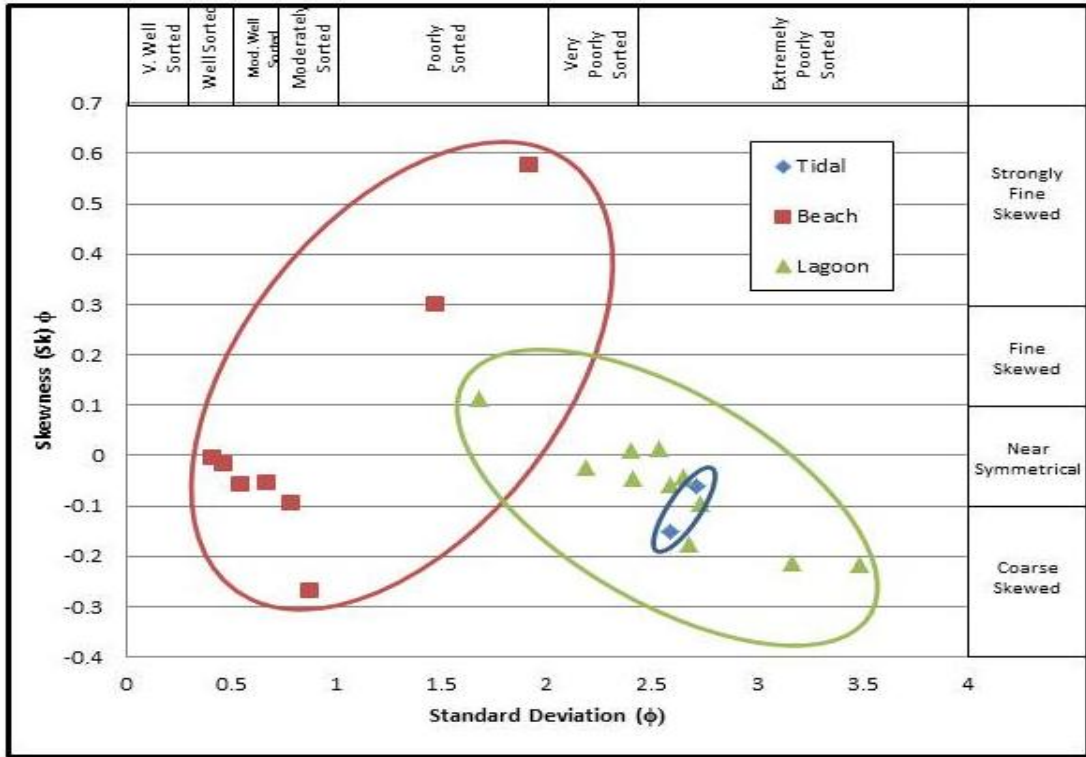


Figure 3.20c: Bivariate plot comparing standard deviation skewness for three different observed facies in the field; tidal flat, beach and lagoon. Fields were added as a comparison aid between the three types of environments.

Outliers for beach sediments were shown to be poorly-sorted and strongly fine-skewed. The grain size in phi was also plotted vs. the standard deviation for the three environments of deposition. The tidal sediments tended toward fine silts in the collected samples and were extremely poorly-sorted. Beach sediments were predominantly medium- to coarse-grained sand and well- to moderately sorted. The outliers were fine-grained sands. Lagoon sediments ranged in sorting from poorly-sorted to extremely poorly-sorted and contained fine-to medium-silts with outliers falling within the coarse silt category. Grain size vs. skewness was also plotted for comparison in Figure. 3.20a-c.

### **3.5 Shoreline Oblique Transect**

The shoreline oblique transect was analyzed through correlation of four stratigraphic sections in the northeastern Plain of Tineh along a 5km stretch along the main irrigation canal. The measured sections were collected in the field parallel to the interpreted Mediterranean coastline during 25 A.D. Figure 3.21 shows the east to west constructed transect. **A** is located 820m northeast of the Pelusiac ruins and **A'** is located 5km west of **A** and 202m south of Al Kantara Shark-Al Arish road.

Section CHA consisted of Facies A and was indicative of subtidal flat deposits. It was capped by the sandy, cross-bedded foreshore sand deposits of Facies B. Section CHB contained Facies B and C which correspond to upper shoreface and foreshore deposits. Section CHC contained both Facies B and Facies D and served as an abrupt facies transition of the sandy foreshore sediments in the east, and the silty lagoon sediments in the west. Section CHD instead contained over 3m of Facies D lagoon sediments. The

transect shows a prograding shoreline and nearshore environment where the lagoon sediments pinch-out between section CHD and CHB, while the foreshore sediments underlying the lagoon sediments in the west are instead interrupted by the subtidal flat facies in the east.

### **3.6 Discussion**

#### **The paleogeography and depositional environment based on sedimentology and lithofacies analysis of the northeastern Plain of Tineh.**

This study also considered the sedimentology and stratigraphy of the northeast corner in the Plain of Tineh. The sedimentology and lithofacies analysis indicates that the Pelusiac paleochannel flowing during Roman times emptied into the Mediterranean through an asymmetrical wave-influenced delta prior to becoming defunct.

Asymmetric wave-influenced deltas may occur when a strong net longshore sediment transport process and an available updrift sediment source are introduced (Bhattacharya and Giosan, 2003). The Pelusiac River was affected by both these factors during Roman times. The modern Damietta was emptying sediment into the Mediterranean to the northwest, and the Tanitic was also flowing to the north-west of the Pelusiac during that time. Both of these active river mouths provided sediment for longshore transport. The strong longshore current was also already flowing south-east along the coast, and the longshore accretion processes are credited with silting-up the Pelusiac River mouth until it became defunct (Sneh and Weissbrod, 1973). Figure 3.21 shows the 3D facies architecture of an asymmetrical delta

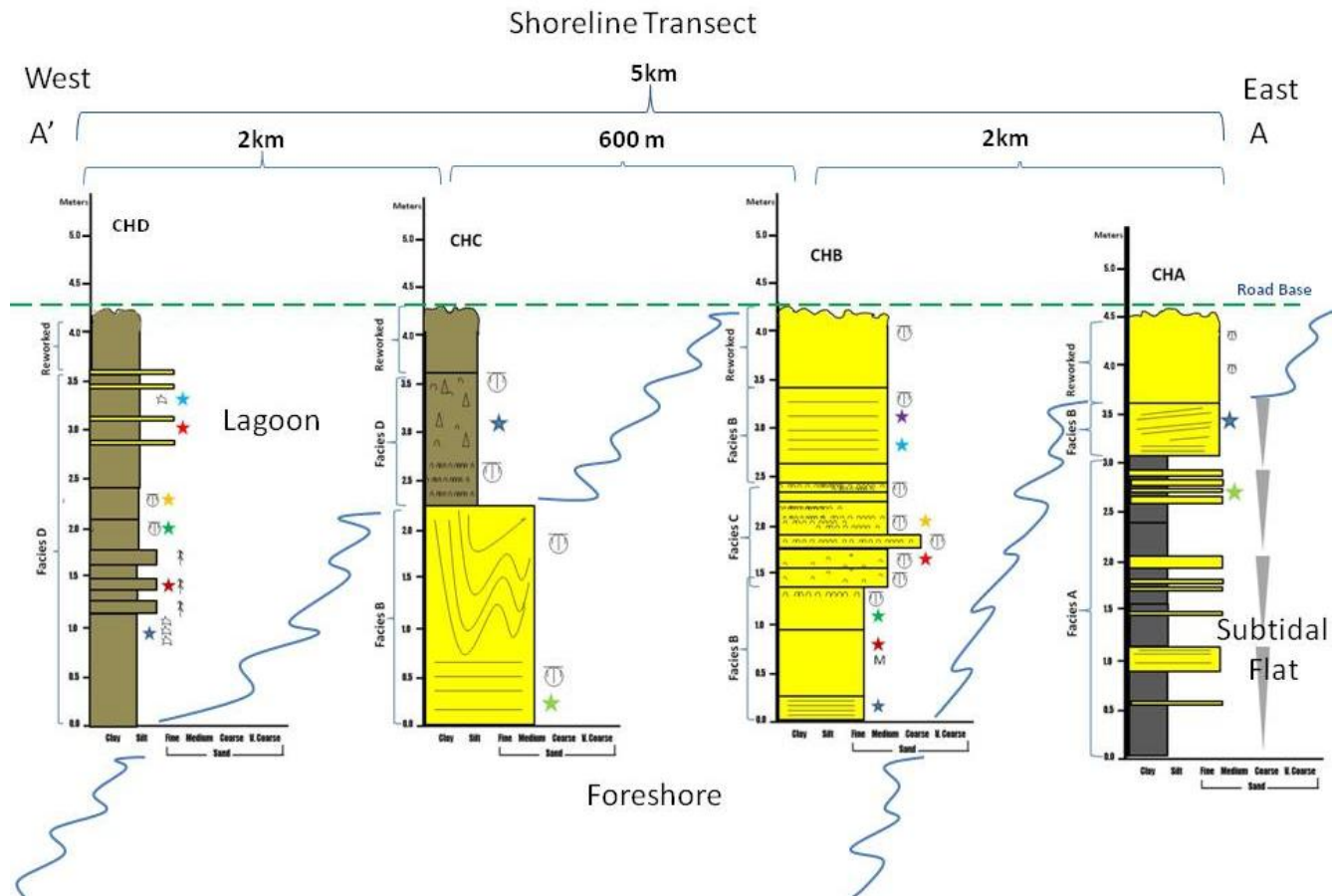


Figure 3.21: Shoreline oblique transect observed along the interpreted Roman coastline of the Mediterranean around 25 AD. The first section at A is located in the East, while the A' corresponds to the west direction. The transect shows tidal flat sediments in the east as well as beach deposits. The latter are overlain by lagoon deposits consisting of dark silts and muds.

Bhattacharya and Giosan (2003) suggest that an asymmetric delta will generally occur in microtidal areas as long as river discharge is greater than the sediment drift. Furthermore, subtidal flats in a high energy coast are often located behind barriers that serve as protection from strong wave activity (Boggs, 2001). The subtidal flat deposits mapped in the shoreline oblique transect are indicative of a subtidal prodelta in the study area. Section CHA was likely located behind a shoreline parallel barrier since the Nile delta coastline is located on a microtidal coast. Section CHB beachface deposits (foreshore) indicate a nearshore coastal environment, and are likely part of a barrier beach. The shell debris beds and heavy mineral banding coarsening into quartzose beds provide evidence of a high-energy wave environment. The shoreline is prograding since low-energy protected subtidal flat sediments are being overlain by open shoreline, high-energy foreshore deposits (Figure 3.22). Section CHD contained Facies D and contained silty lagoon deposits. These environments may be found in an asymmetric delta, which often creates protected lagoonal environments through a barrier complex (Bhattacharya and Giosan, 2003).

These interpretations, coupled with the strong south-east flowing longshore current, indicate that the Pelusiac river emptied into an asymmetric delta. Figure 3.24a portrays the Pelusiac prior to becoming defunct in 25 A.D. The Pelusiac flows in a single channel towards the Mediterranean into an asymmetric delta bounded by sandy ridges, though the majority of these are located on the updrift side. Figure 3.24b shows the progression of the paleochannel being deflected as riverine sediment discharge becomes

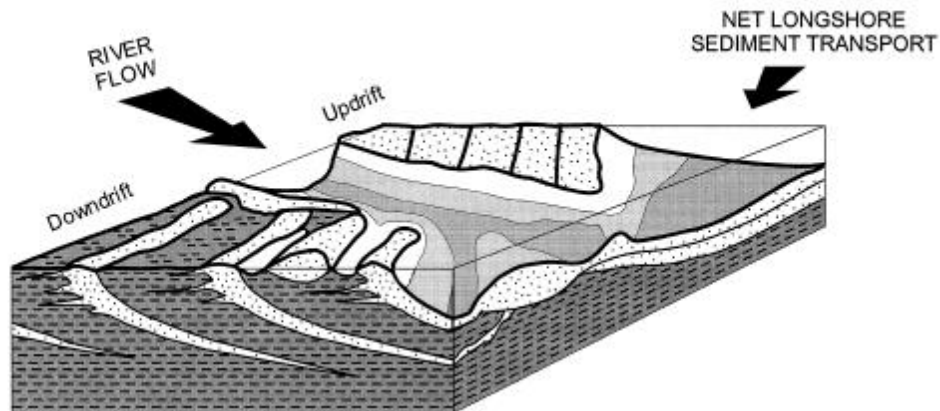


Figure 3.22: 3D Block diagram of an asymmetric wave-influenced delta. The updrift area of the delta contains sandy beach ridges while downdrift of the delta, bayhead and lagoon deposits are bounded by sandy barrier bar complexes. Source: Bhattacharya and Giosan, 2003.

less than the sediment drift deposits. Finally, in Figure 3.24c, the channel silts up and becomes defunct. Subsequent longshore accretion processes continue to deposit sediment along the coastline of the Plain of Tineh, building the present-day strandplain.

Sedimentary structures and lithofacies indicate that the sampled study area is the downdrift margin of an asymmetric delta. Since, the study area is updrift of the known Pelusiac river mouth located at the Pelusium ruins, the location would normally suggest the updrift margin. The Pelusiac river mouth was likely deflected through time as a result of decreasing sediment discharge, though. Sneh and Weissbrod (1973) reported two paleo-channel river branches, breaking off from the main Pelusiac trace and flowing north into the Mediterranean. It is possible that these branches did not flow consecutively with the supposed main trunk. Instead, they might be earlier terminal distributary branches that were previously deflected by the longshore drift. These diverging channels were not observed in the remote sensing analysis though, so further study would be

required to make a positive identification. Although this study has focused upon the Pelusiac, the Tanitic River was also flowing into the Mediterranean to the northwest of the Pelusiac. Due to the proximity, it is also possible that the Tanitic River was also affected by the net longshore drift, and its asymmetric delta's downdrift margin is the area that was sampled in this study. The support of the shape and location of the sedimentary ridges immediately north of sampled sections CHA and CHB more greatly commends the deflected distributary channel interpretation. As the channel migrated, downdrift, the downdrift margin deposits would be located further northwest than expected.

The downdrift margin includes the barrier-lagoon systems and less populous sand-barrier ridges common to the downdrift margin (Bhattacharya and Giosan, 2003). Section CHC showed a sharp transition between facies and indicates an abrupt change in depositional environment. Convolute bedding in the underlying sandy beds suggests shallow flow creating shear stress within the sandy beds (Boggs, 2001). The liquefaction caused the contorted layers and anticlinal features which are truncated at the contact with

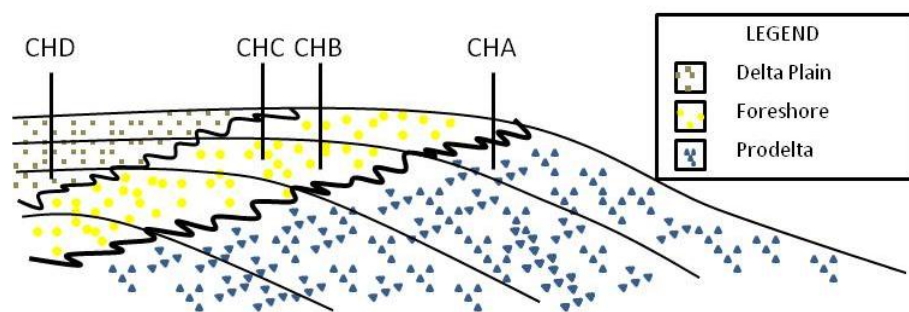


Figure 3.23: The interpreted sedimentary sequence for the study area is shown. The constructed shoreline transect portrays a progradational shoreline. The vertical lines show the position of the measured sections in relation to the sequence.

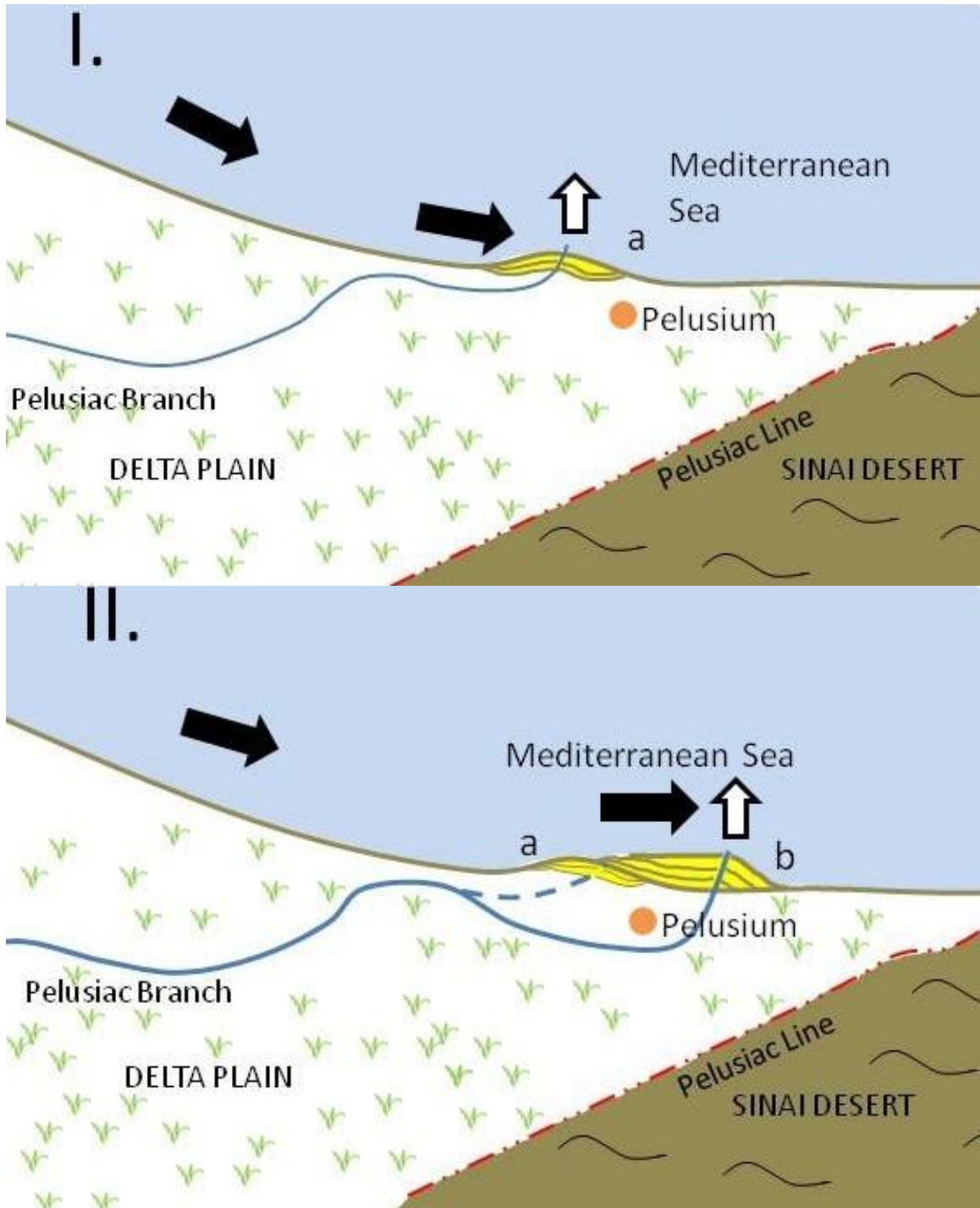


Figure 2.24: a) At I., The Pelusiac River is shown flowing northeast and emptying into an asymmetrical delta,(a.) b) At time II, in location b. The distributary river has been deflected into a second asymmetrical delta (b) building onto the first (a). Black arrow shows direction of longshore current. White arrow shows direction of fluvial sediment discharge.

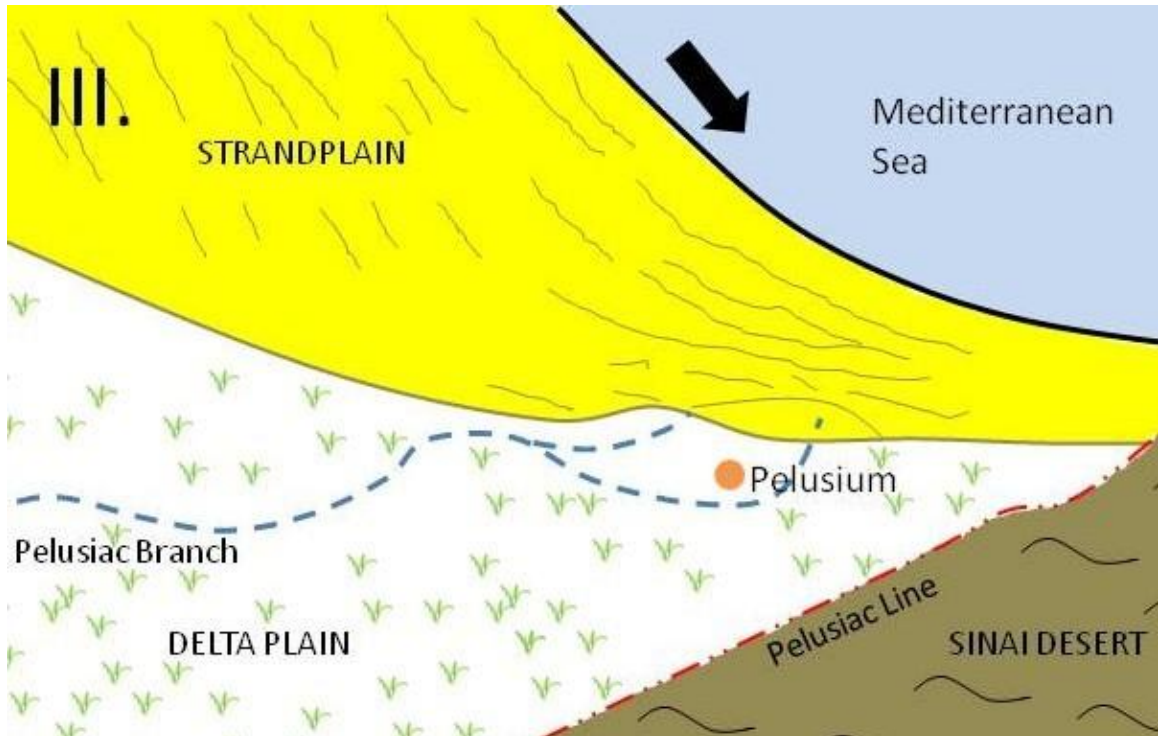


Figure 3.24c: At time III at ~25AD, the Pelusiac River has gone defunct due to longshore accretion processes which silted up the river mouth. Accretionary ridges mark additions to the strandplain through time as the net longshore current continues to deposit sediment from the modern Damietta river mouth. Black arrow shows direction of net shoreline current.

the fossiliferous silts of the lagoon facies. The abrupt contact is likely due to changes in the hydrodynamic regime. The silt beds observed in section CHC and CHD were walked out along the canal trace. They pinch-out into the foreshore sediments of section CHB. Section TEF was trenched, so a stratigraphic section was not created. The muddy sand within the samples of section TEF, correlate to the lagoon muddy sands of Facies D that were also observed in stratigraphic section CHC and CHD. The muds are similar and likely belong to the same Bilgas formation. Thus, we can deduce that the lagoon mud beds interfinger in the area south of the Roman Mediterranean coastline and west of the Pelusiac ruins, but do not progress into the northern strandplain ridges that began accreting onto the coastline post 25A.D. (Figure 3.25). Ages of the stratigraphic beds are

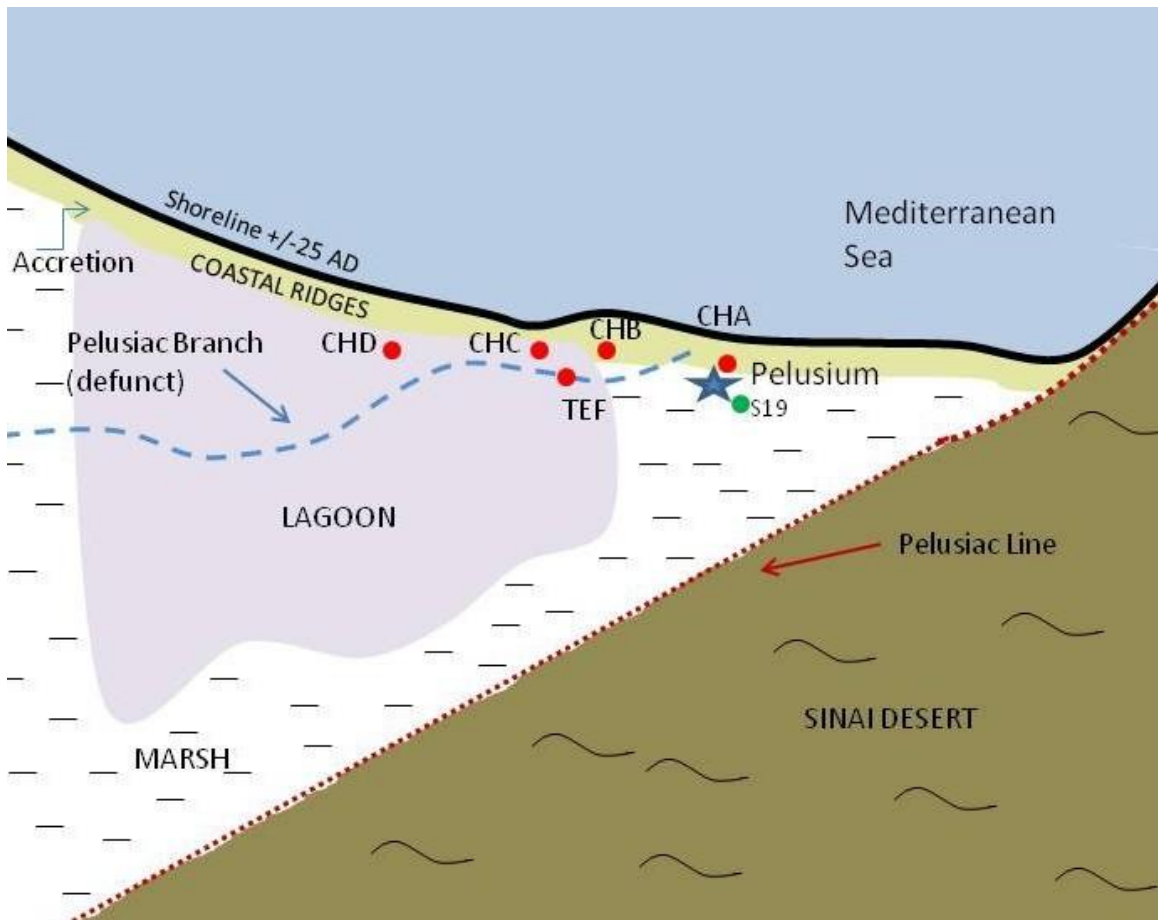


Figure 3.25: Sketch showing the paleogeography of the Plain of Tineh after the Pelusiac Branch mouth silted up and the river went defunct. Location of measured sections is shown. The coastal ridges represent accretion to the main delta body and aided the cease of flow for the river in this area. The area north of the Pelusiac Line was identified as Unit III and IV of Stanley et al. 2008. Modified after Coutellier and Stanley, 1987.

unknown but a Smithsonian core, S-19, collected east of the Pelusiac ruins in 1985 provides a radiocarbon age of 3070 $\pm$  110 BP for the base of the coastal and lagoon sediments observed in the core (Stanley et al., 2008). The date for the base of the coastal and lagoon sediments is calibrated to 800-850 AD by Goodfriend and Stanley (1999). The data suggests that the recorded facies in the studied area are equal the upper part of unit III and lower part of unit IV of Stanley et al. (2008) which were deposited during the

period (nearly from 1000 to 800 BC) of regression of the shoreline accompanied by uplifting of the area from approximately 1000 through 800 B.C.

# **Chapter 4: Conclusion**

Remote sensing methods were applied in order to verify the location of the Pelusiac's lower course and increase its known flow path east of the Suez Canal. Multispectral remote sensing in the form of SPOT and Landsat satellites, and radar datasets from the TerraSAR-X, PALSAR, RADARSAT and SIR-C platforms were all implemented. Remote sensing aided in verifying the location of the lower Pelusiac on the delta plain east of the Suez Canal through Landsat imagery. The observed linear feature is 135m wide at its maximum and approximately 13km long. It extends from Tell el Farama toward the east in the direction of the Suez Canal, just north of the Peace Canal. The trace is lost within 10km of the Suez Canal as the linear feature intersects the Peace Canal, probably due to the extensive construction undertaken to create the new canal structure. The feature has low sinuosity, indicative of a straight planform river and four marked paleomeanders. Planform analysis derived a bankfull paleo-discharge value of  $\sim 5700 \text{ m}^3 \text{ s}^{-1}$  and an average discharge of  $650 \text{ m}^3 \text{ s}^{-1}$  using the reach average for the Pelusiac river. Terminal meanders were also chosen for the modern Damietta branch as an accuracy check for the calculated values. Although the Pelusiac was not the main distributary in the Nile Delta, the derived values show a large distributary river transporting water and sediment into the northeastern delta plain prior to the river mouth completely silting up. Field work observations and measurements were analyzed north of the Pelusium ruins. Four different lithofacies were identified within the observed sedimentary succession in the northeast Plain of Tineh. The lithofacies are: Facies A- Subtidal Flat, Facies B-Foreshore sands, Facies C- Beachface Shell Deposits, Facies D-Lagoon Silts. In addition to field observations, samples were collected for further

analysis including identification of mollusk fossils, diatom analysis and laser particle size analysis. Stratigraphic sections were also created and a shoreline oblique transect was analyzed and discussed. The transect shows a prograding shoreline and nearshore environment where the lagoon sediments pinch-out toward the east of the delta plain. The foreshore sediments underlying the lagoon sediments interfinger in the west. These are subsequently interrupted by subtidal flat deposits north of the Pelusium ruins. The sampled study area is consistent with a downdrift margin of an asymmetric delta with barrier lagoon systems.

## REFERENCES

- ABDEL-KADER, A., 1982. Landsat analysis of the Nile Delta, Egypt, *Diss. University of Delaware*, PhD. Dissertation.
- AMSLER, M., RAMONELL, C. and TONIOLO, H. 2005. Morphologic changes in the Parana River channel (Argentina) in the light of the climate variability during the 20th century. *Geomorphology*. v. 70, p. 257-278.
- BAYNES, T.S., 1988. "Egypt." *The Encyclopedia Britannica: a Dictionary of Arts, Sciences, and General Literature*. v. 7, p. 705-710.
- BHATTACHARYA, J.P. and GIOSAN, L. Wave-influenced deltas: geomorphological implications for facies reconstruction. *Sedimentology*. v. 50, p. 187-210.
- BHATTACHARYA, J. P., 2006, Deltas, in: Posamentier, H.W. and Walker, R.G., eds., *Facies Models Revisited: Society for Sedimentary Geology (SEPM): Tulsa, OK, United States: Special Publication - Society for Sedimentary Geology*, v. 84, p. 237-292.
- BISHOP, P. and GODLEY, D. 1994. Holocene paleochannels at Satchanalai, north-central Thailand: ages, significance and paleoenvironmental indications. *Holocene*. v.4, p.32-41.
- BOGGS, S. 2001. *Principles of Sedimentology and Stratigraphy*. 3rd Edition. Prentice Hall.
- CALLOW, J. and SMETTAN, K. 2006. Channel response to a new hydrological regime in southwestern Australia. *Geomorphology*. v. 84. p. 254-276.
- CARLSTON, C. 1965. The relation of free meander geometry to stream discharge and its geomorphic implications, *American Journal of Sciences*. v. 263. p. 864-885.
- COLEMAN, J. M., 1981. *Deltas: Process of Deposition and Models for Exploration*, 2<sup>nd</sup> ed. Burgess Publishing Company, Minneapolis.
- COUTELLIER, V. and STANLEY, D. J., 1987. Late Quaternary stratigraphy and paleogeography of the eastern Nile Delta, Egypt. *Marine Geology*, v. 77, p. 257-275.
- DURY, G.H. 1954. Bedwidth and wavelength in meandering valleys. *Nature*. v. 176. p. 31.

- DURY, G.H. 1976. Discharge prediction, present and former, from channel dimensions. *Journal of Hydrology*. v. 30. p. 219-245.
- ELACHI, C., LADISLAVE, R., and SCHABER, G.G., 1984. Spaceborne radar subsurface imaging in hyperarid regions. *IEEE Transactions on Geoscience and Remote Sensing*. v. GE-22, No. 4. p. 383-388.
- EL-DIN, S. 1977. Effect of the Aswan High Dam on the Nile flood and on the estuarine and coastal circulation pattern along the Mediterranean Egyptian coast. *Limnology and Oceanography*. v. 22(2). p. 194-207.
- FANOS, A., FRIHY, O., KHAFAGY, A., and KOMAR, P. 1993. Erosion of the Damietta Promontory, the Nile Delta. In: Coastal Engineering '92. (Ed. W.L. Edge). *American Society of Civil Engineering*. New York. p. 3246-3259.
- FRIHY, O., 1996. Some proposals for coastal management of the Nile delta coast, *Ocean & Coastal Management*, v. 30, p. 43-59.
- GABER, A., KOCH, M., HELMI, G., M. and SATO, M., 2011. SAR Remote sensing of buried faults: Implications for groundwater exploration in the western desert of Egypt. *Sensing and Imaging: An International Journal*. v. 12, i. 3-4, p 133-151.
- GALLOWAY, W.E., 1975, Process framework for describing the morphological and stratigraphic evolution of deltaic depositional systems, in : M.L. Broussard (ed.), *Deltas, Models for Exploration*, 2<sup>nd</sup> edition, Houston, Texas, Houston Geological Society, p. 87-98.
- GALLOWAY, W.E., and HOBDDAY, D.K., 1996. *Terrigenous Clastic Depositional Systems*, 2nd Edition Springer-Verlag, p.60-157.
- GEOENGINEERS, INC., 2008, Report, Quality Assurance Project Plan for the Paleochannel Water Quality Monitoring Study WRIA 54 Planning Unit Study, Pacific Northwest Technology Park, Spokane, Washington: Report prepared for WRIA 54 Planning Unit, May 23. p. 1-10.
- GOODFRIEND, G. A. and STANLEY, D. J. 1999. Rapid strand-plain accretion in the northeastern Nile Delta in the 9<sup>th</sup> Century A.D. and the demise of the port of Pelusium. *Geology* v. 27(2), p.147-150.
- HOFFMEIER, J. and ABD EL-MAKSOU M., 2003. A new military site on “The Ways of Horus”- Tell El-Borg, 1999-2001: A preliminary report. *The Journal of Egyptian Archaeology*, v. 89, p. 169-197.

- LILLESAND, T.M., KIEFER, R.W., and CHIPMAN, J.W., 2004. *Remote Sensing and Image Interpretation*, 5<sup>th</sup> ed. New York, John Wiley and Sons, Inc.
- MIALL, A.D., 1977. A review of the braided river depositional environment. *Earth Science Reviews*. v. 13(1). p. 1-62.
- NATIONAL AERONAUTICS AND SPACE ADMINISTRATION (NASA), 2011. *Landsat 7 Science Data Users Handbook*. p. 1-186.
- NEEV, D. 1977. The Pelusium Line- A major transcontinental shear. *Tectonophysics*.v. 38. p. T1-T8.
- NEGM, A., ABDEL-AZIZ, T., SALEM, M. and YOUSEF, W. 2011. Impact of future discharges on Damietta Branch morphology. *Fifteenth International Water Technology Conference, IWTC 15- 2011, Alexandria, Egypt*.
- NIXON, S., 2004. The Artificial Nile – The Aswan High Dam destroyed a fishery, but human activities may have revived it, *American Scientist*, p. 92-158.
- OSTERKAMP, W. and HEDMAN, E. 1982. Perennial streamflow characteristics related to channel geometry and sediment in Missouri River basin. *USGS Professional Paper*. v. 1242. p. 847-851.
- PICKUP, G., and WARNER, R. 1984. Geomorphology of tropical rivers. II. Channel adjustment to sediment load discharge in the Fly and lower Purari, Papua New Guinea. *Catena*. v. 5. p. 19-41.
- RIZZINI, A., VEZZANI, F., COCCOCCETTA, V., and MILAD, G., 1978. Stratigraphy and sedimentation of a Neogene-Quaternary section in the Nile Delta area. *Marine Geology*, v.27, p. 327-348.
- ROSENQVIST, A., SHIMADA, M., and WATANABE, M., 2004. ALOS PALSAR: Technical outline and mission concepts. *4<sup>th</sup> International Symposium on Retrieval of Bio-and Geophysical Parameters from SAR Data for Land Applications*. Innsbruck, Austria.
- ROSGEN, D. L. 1994. A classification of rivers. *Catena*. v. 22. p. 169-199.
- ROSGEN, D.L. 1996. A classification of natural rivers: a reply to the comments by J.R. Miller and J.B. Ritter. *Catena*. v. 27. p. 301-307.
- SAID, R. 1981. *The Geologic Evolution of the River Nile*. Springer-Heidelberg, New York.

- SCHUM, S.A. 1968. River adjustment to altered hydrologic regimen- Murrumbidgee River and paleochannels, Australia. *United States Geological Survey Professional Papers*. v. 598. p. 65.
- SNEH, A. and WEISSBROD, T., 1973. Nile Delta: the defunct Pelusiac branch identified. *Science* v. 80, p. 59-61.
- SRIDHAR, A. 2007. Discharge estimation from planform characters of the Shedhi River, Gujarat alluvial plain: Present and past. *Journal of Earth System Science*. v. 116(4). p. 341-346.
- STANLEY D.J., 1988. Subsidence in the northeastern Nile delta: rapid rates, possible causes, and consequences. *Science*, v. 240, p. 497-500.
- STANLEY, D.J., BERNASCONI, M.P. and JORSTAD, T.F., 2008. Pelusium, an ancient port fortress on Egypt's Nile Delta Coast: Its evolving environmental setting from foundation to demise. *Journal of Coastal Research*, v. 24, p. 451-462.
- SUMMERHAYES, C.P.; SESTINI, G.; MISDORP, R., and MARKS, N., 1978. Nile Delta, nature and evolution of continental shelf sediments. *Marine Geology*, v.27, p.43-65.
- THURMOND, A. K., ABDELSALAM, M.G., and THURMOND, J.B., 2006. Optical-radar-DEM remote sensing data integration for geological mapping in the Afar Depression, Ethiopia. *Journal of African Earth Sciences*, v. 44, p. 119-134.
- TORNARITIS, G. 1987. *Mediterranean Sea Shells, Cyprus*. G. Tornaritis, 1987.
- WILLIAMS, G.P. 1978. Bankfull discharge of rivers. *Water Resources Research*. v. 14(6). p. 1141-1154.
- WILLIAMS, G. P. 1986. River meanders and channel size. *Journal of Hydrology*. v. 88. p. 147-164.
- WILLIAMS, G. P. 1988. Paleofluvial estimates from dimension of former channels and meanders. *Flood Geomorphology*. Wiley, New York. p. 321-334.
- WRIGHT, L.D., and J.M. COLEMAN, 1973. Variations in morphology of major river deltas as functions of ocean wave and river discharge regimes. *American Association of Petroleum Geologists Bulletin*. v. 57, p. 370-398.

ZHANG, B., AL, N., HUANG, Z., YI, C.B. and QUIN, F.C. 2008. Meanders of the Jialing River in China: Morphology and formation. *Chinese Science Bulletin*. v. 53(2). p. 267-281.

**APPENDIX A**  
**Grain Size Analysis**

117

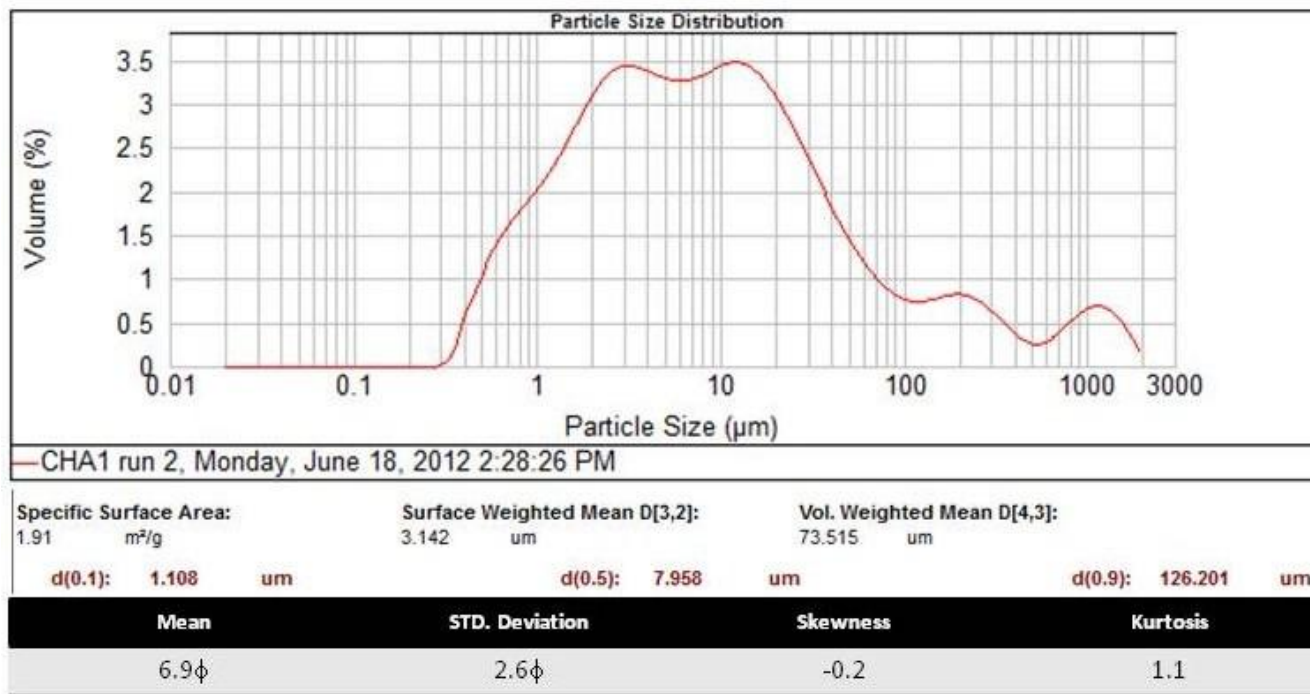


Figure A1: Plot of particle size (µm) vs. volume percent (vol. %) and calculated statistical parameters for Sample CHA1.

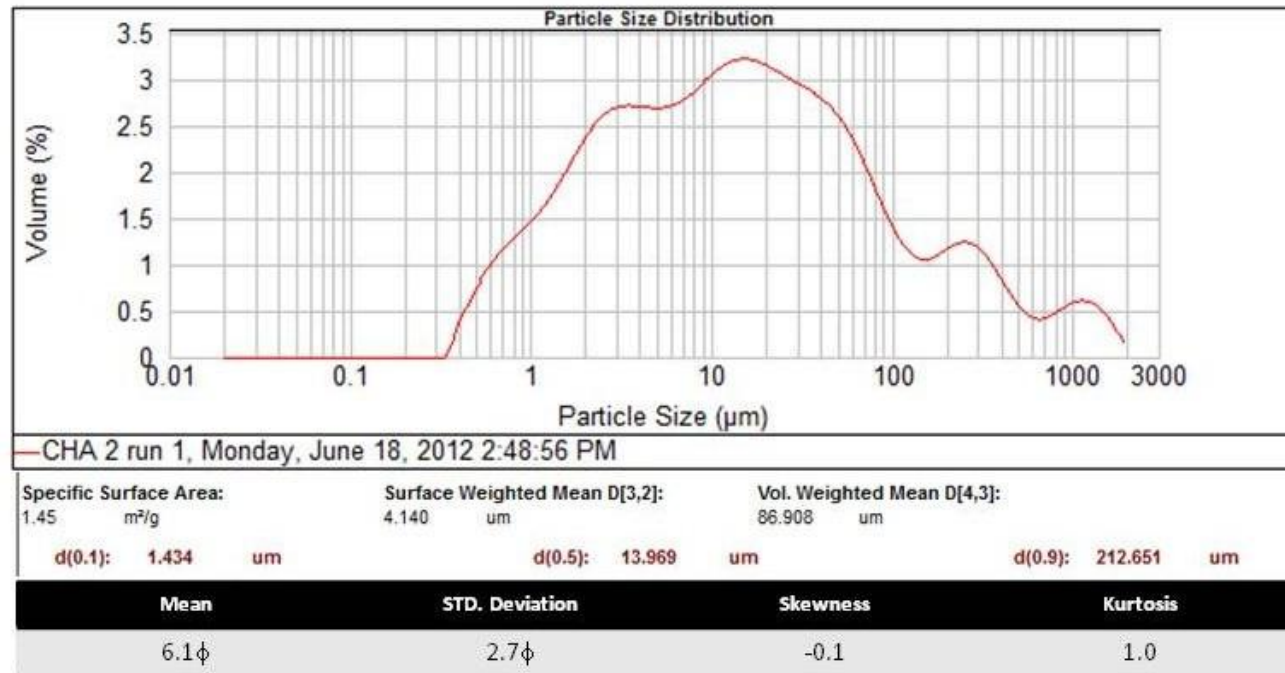
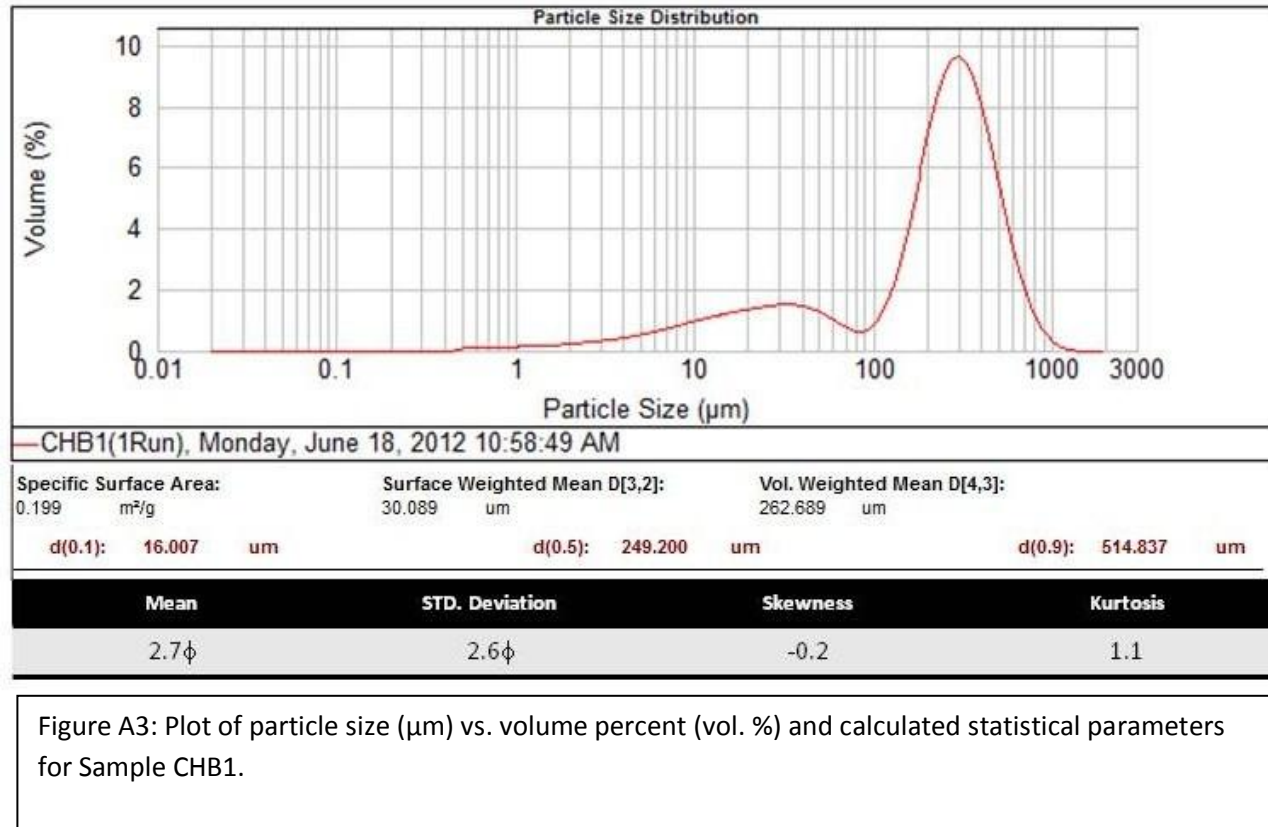


Figure A2: Plot of particle size ( $\mu\text{m}$ ) vs. volume percent (vol. %) and calculated statistical parameters for Sample CHA2.



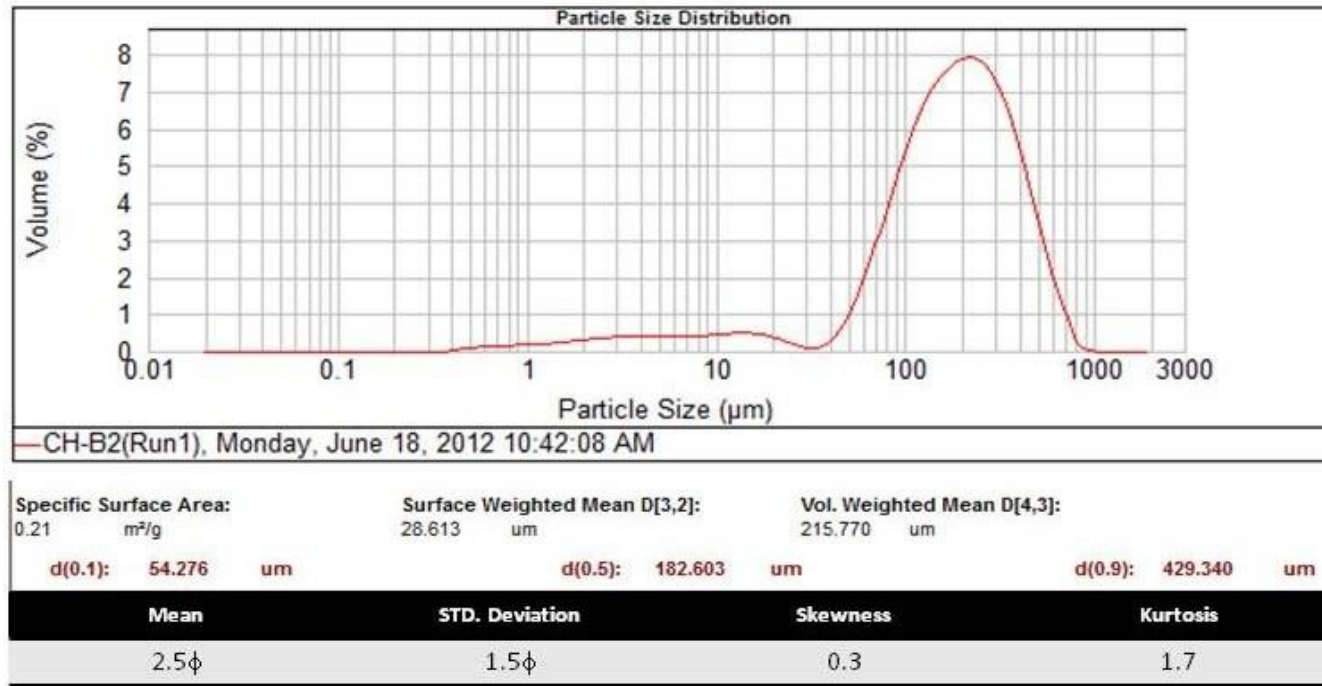


Figure A4: Plot of particle size ( $\mu\text{m}$ ) vs. volume percent (vol. %) and calculated statistical parameters for Sample CHB2.

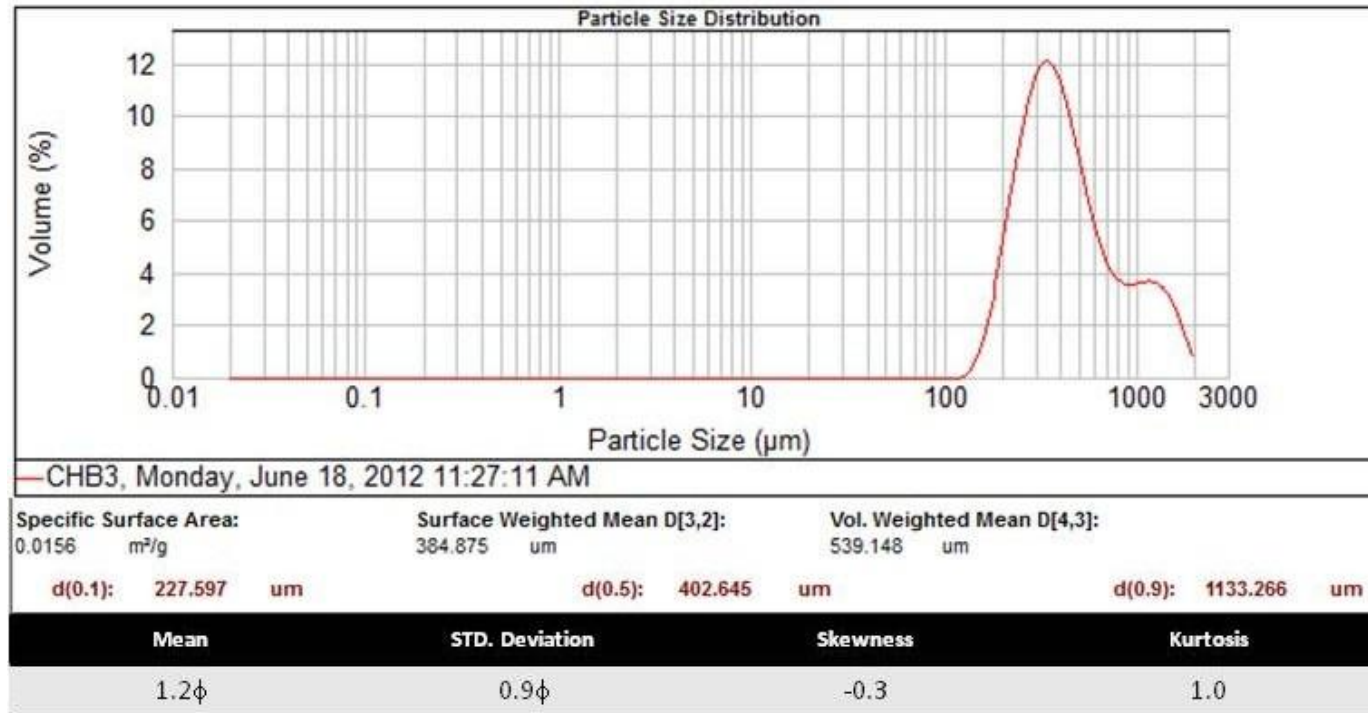


Figure A5: Plot of particle size ( $\mu\text{m}$ ) vs. volume percent (vol. %) and calculated statistical parameters for Sample CHB3.

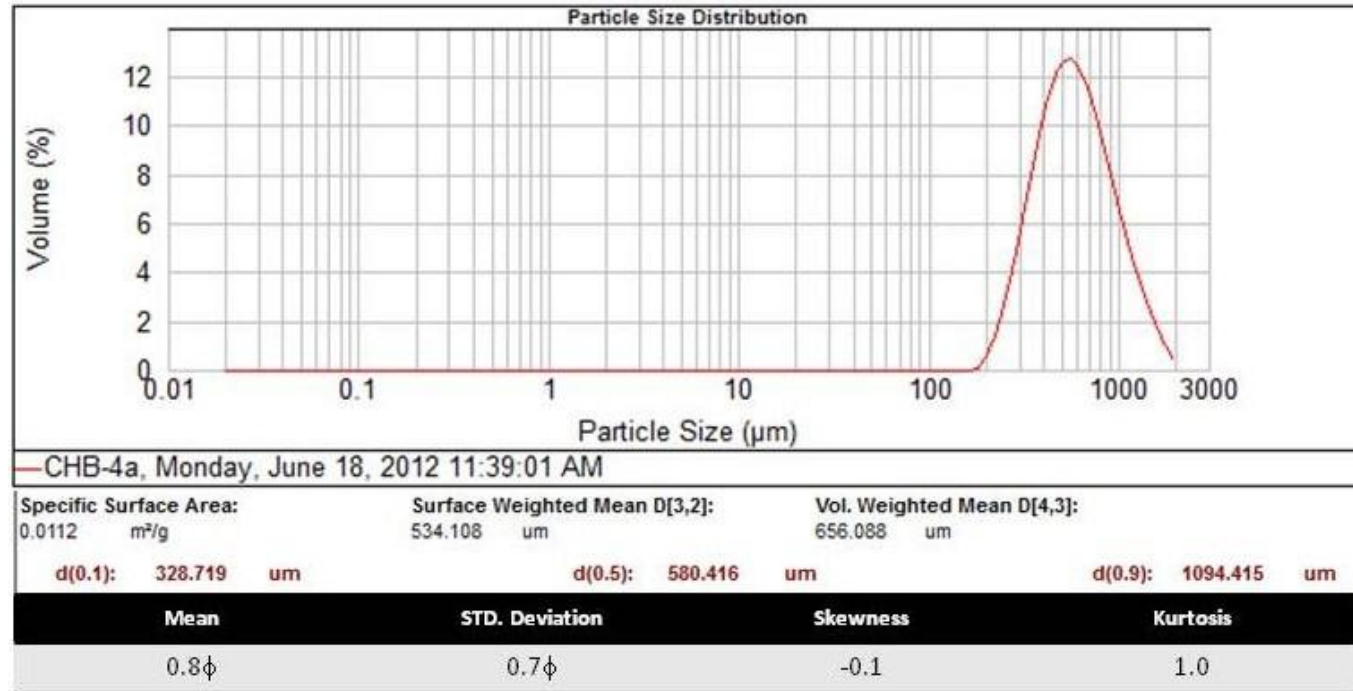


Figure A6: Plot of particle size ( $\mu\text{m}$ ) vs. volume percent (vol. %) and calculated statistical parameters for Sample CHB4a.

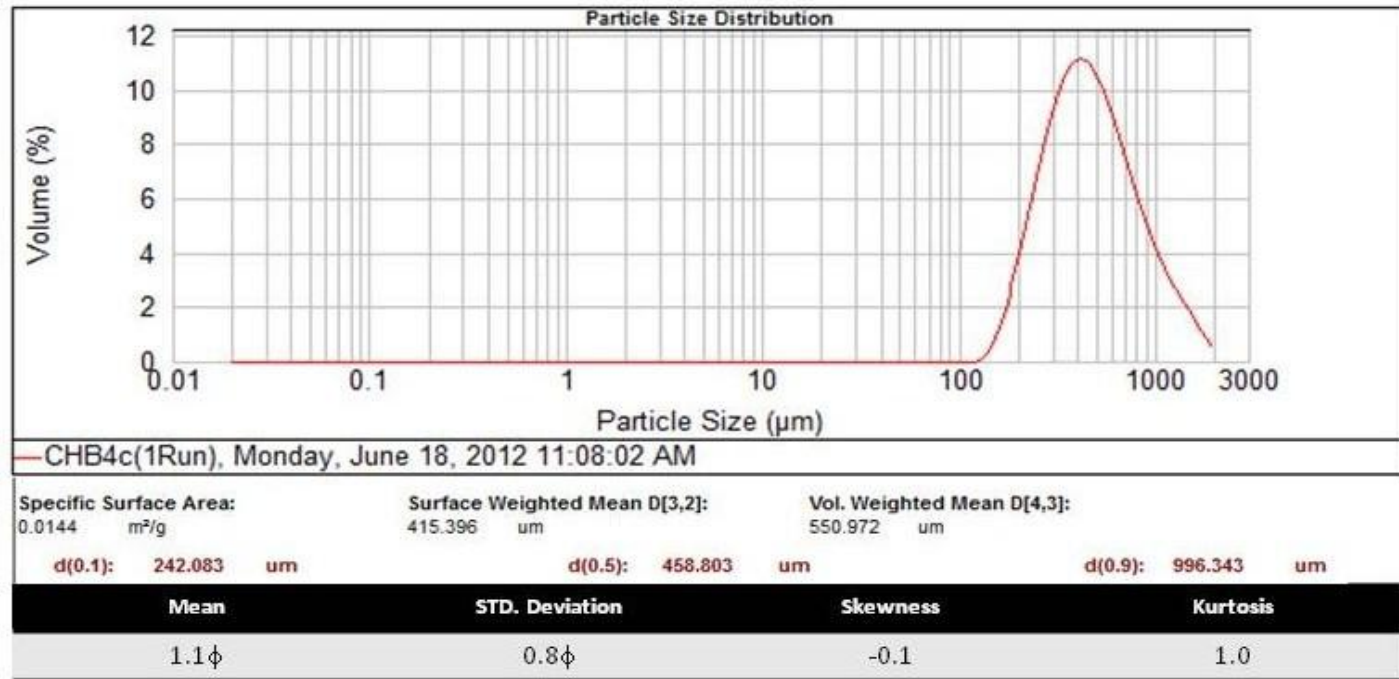


Figure A7: Plot of particle size ( $\mu\text{m}$ ) vs. volume percent (vol. %) and calculated statistical parameters for Sample CHB4c.

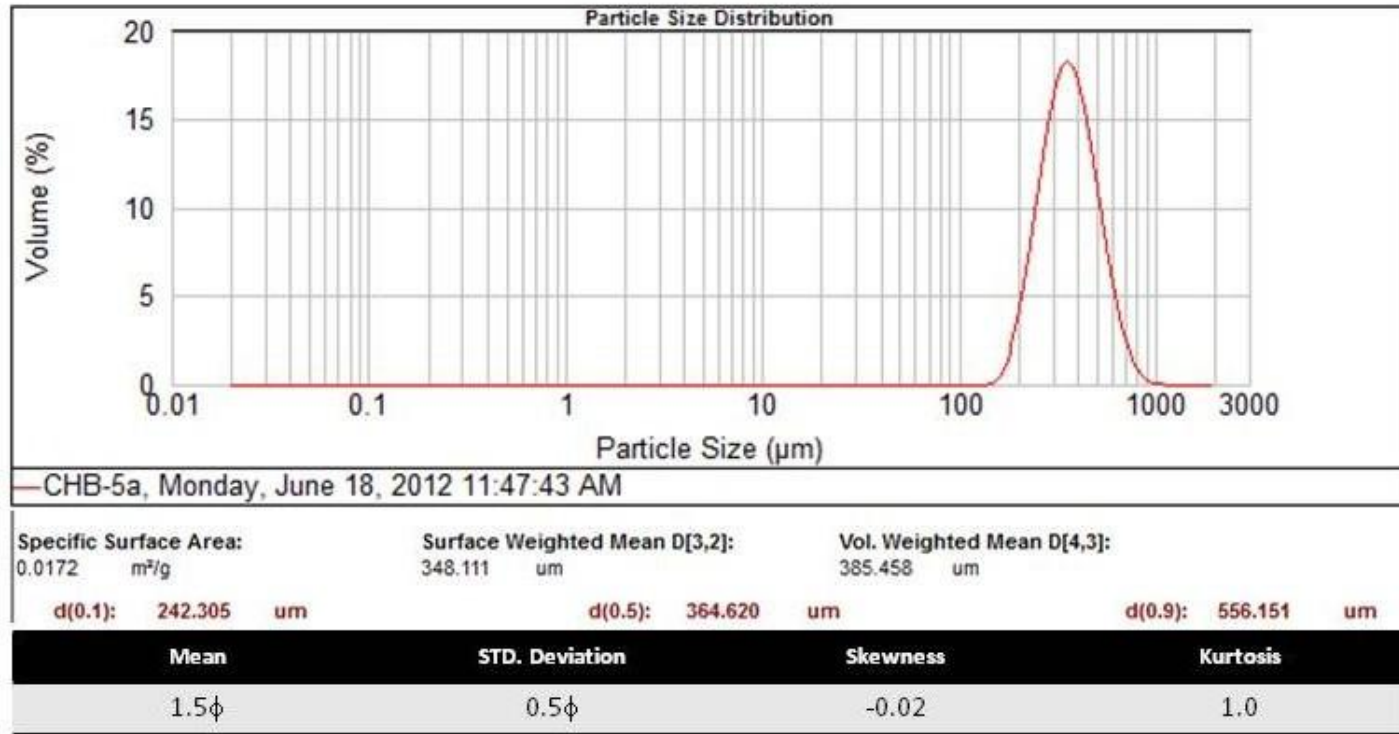


Figure A8: Plot of particle size ( $\mu\text{m}$ ) vs. volume percent (vol. %) and calculated statistical parameters for Sample CHB5a.

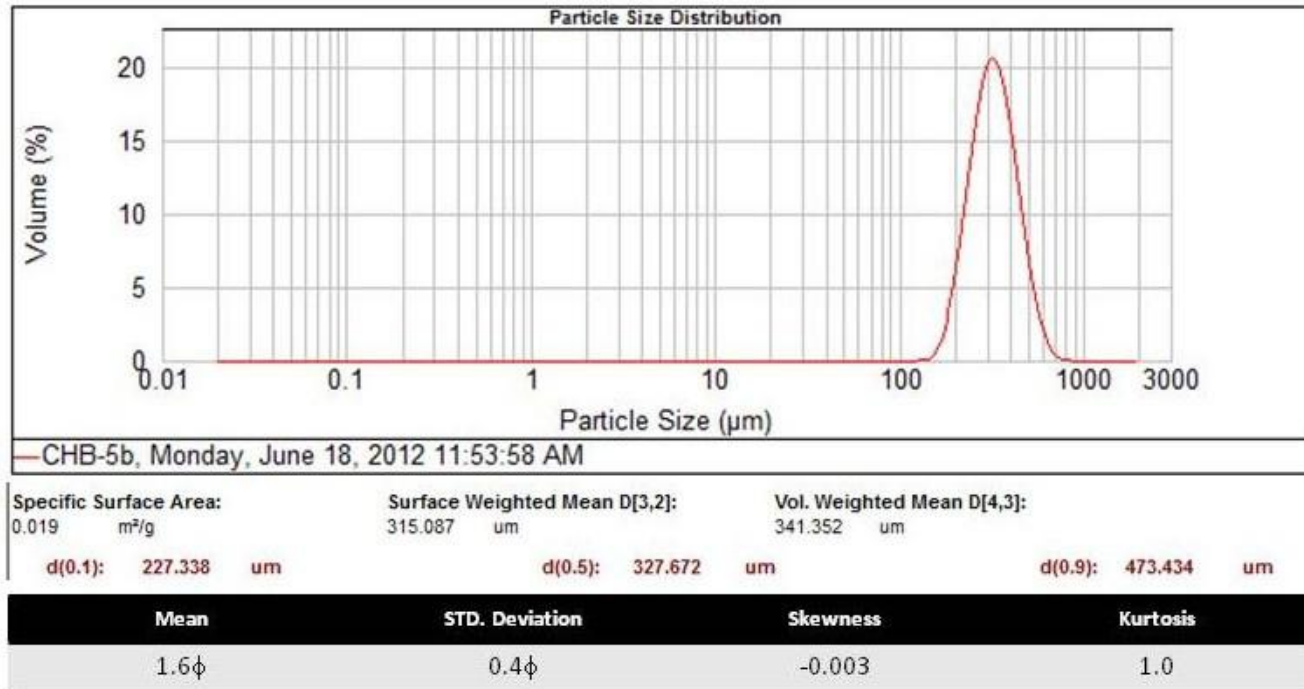


Figure A9: Plot of particle size ( $\mu\text{m}$ ) vs. volume percent (vol. %) and calculated statistical parameters for Sample CHB5b.

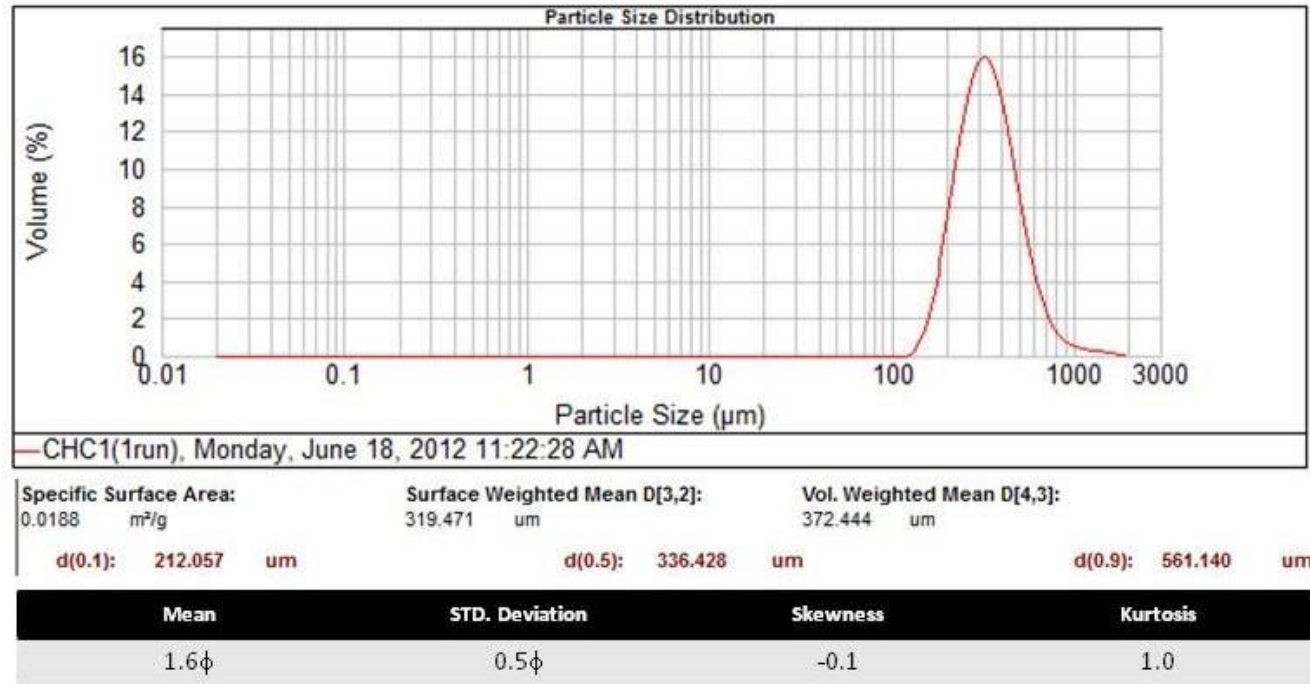


Figure A10: Plot of particle size ( $\mu\text{m}$ ) vs. volume percent (vol. %) and calculated statistical parameters for Sample CHC1.

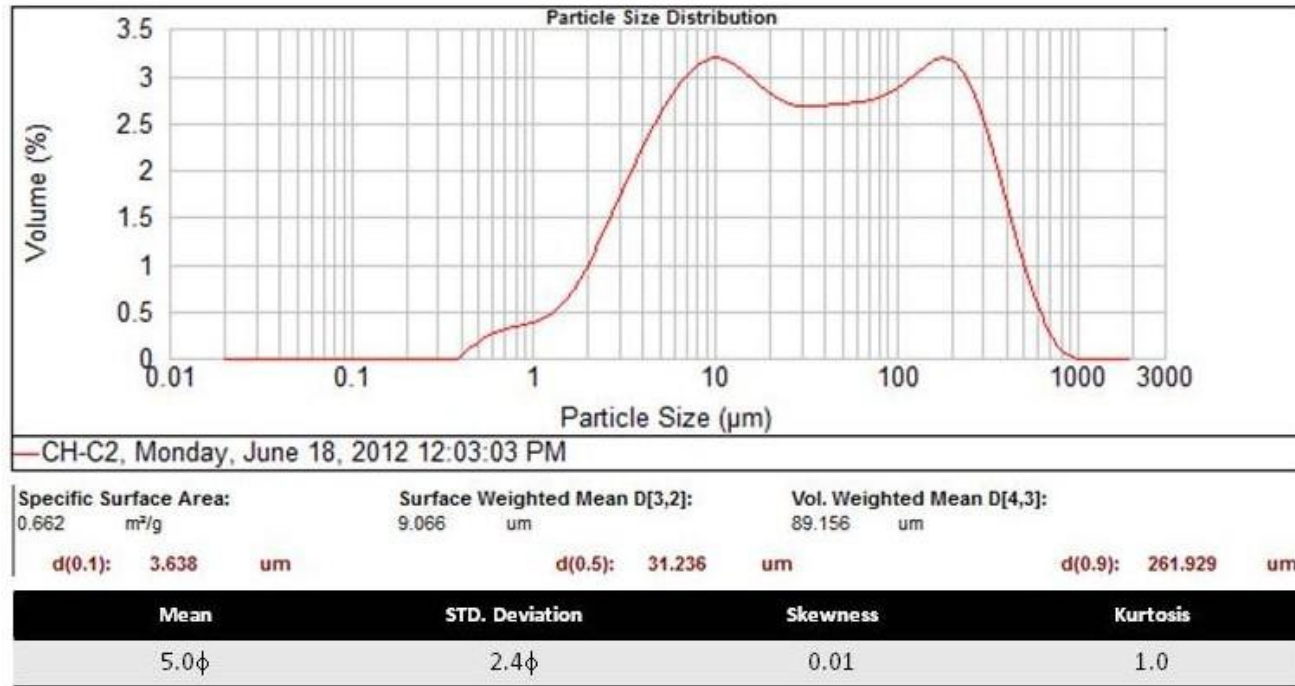


Figure A11: Plot of particle size ( $\mu\text{m}$ ) vs. volume percent (vol. %) and calculated statistical parameters for Sample CHC2.

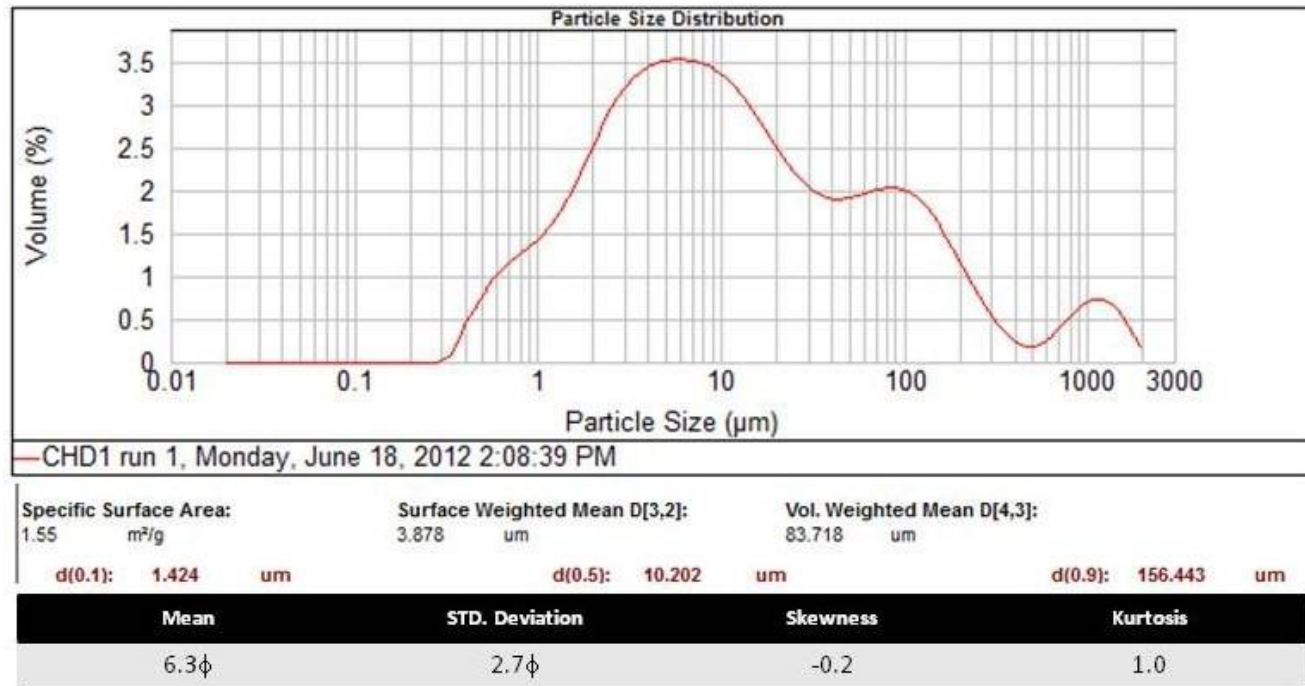


Figure A11: Plot of particle size ( $\mu\text{m}$ ) vs. volume percent (vol. %) and calculated statistical parameters for Sample CHD1.

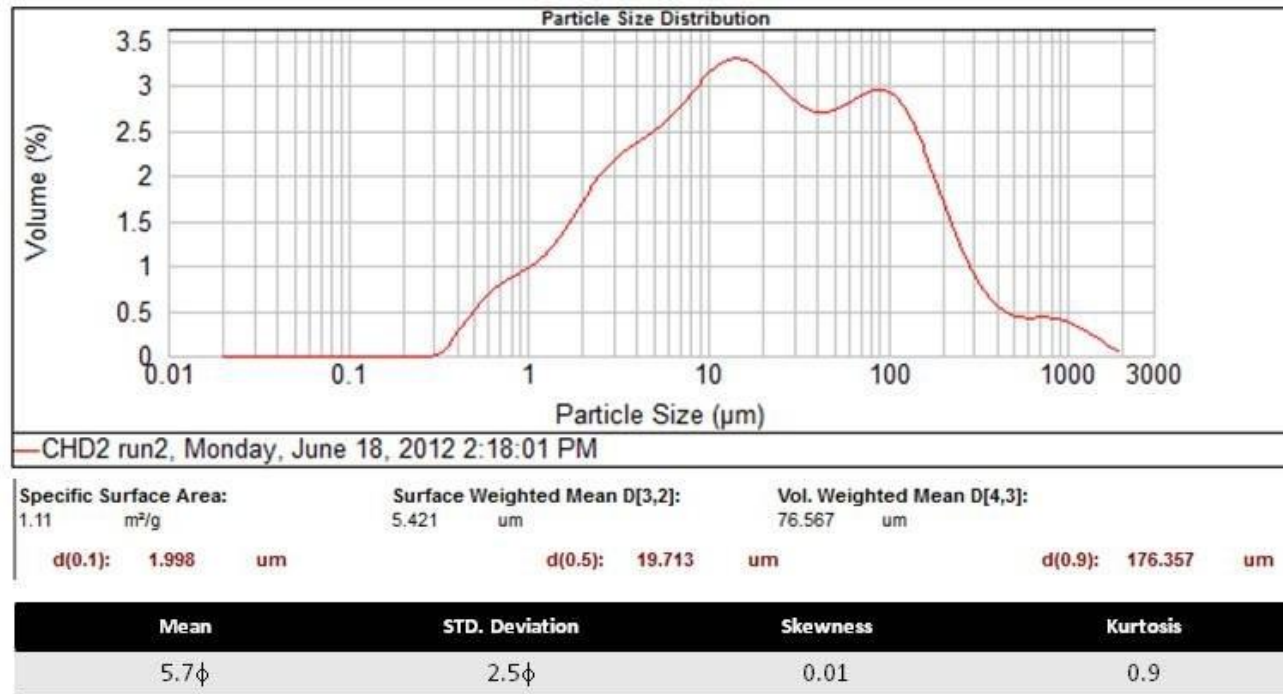


Figure A12: Plot of particle size ( $\mu\text{m}$ ) vs. volume percent (vol. %) and calculated statistical parameters for Sample CHD2.

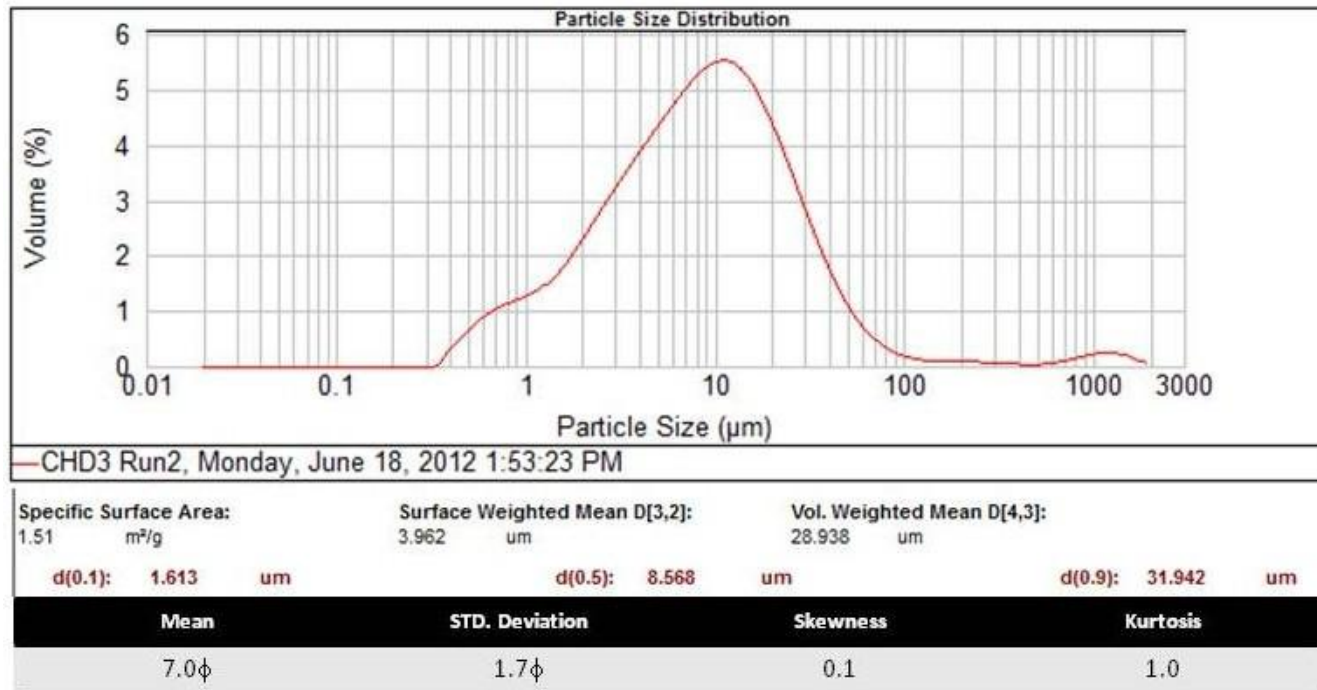


Figure A13: Plot of particle size ( $\mu\text{m}$ ) vs. volume percent (vol. %) and calculated statistical parameters for Sample CHD3.

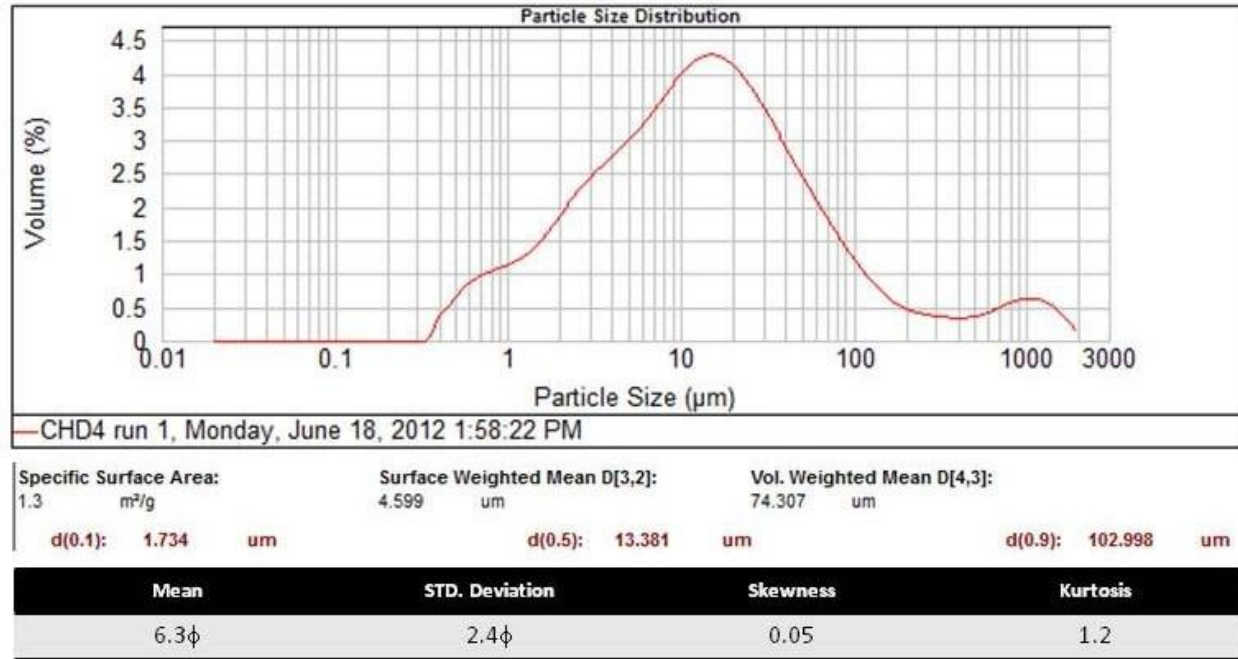


Figure A14: Plot of particle size ( $\mu\text{m}$ ) vs. volume percent (vol. %) and calculated statistical parameters for Sample CHD4.

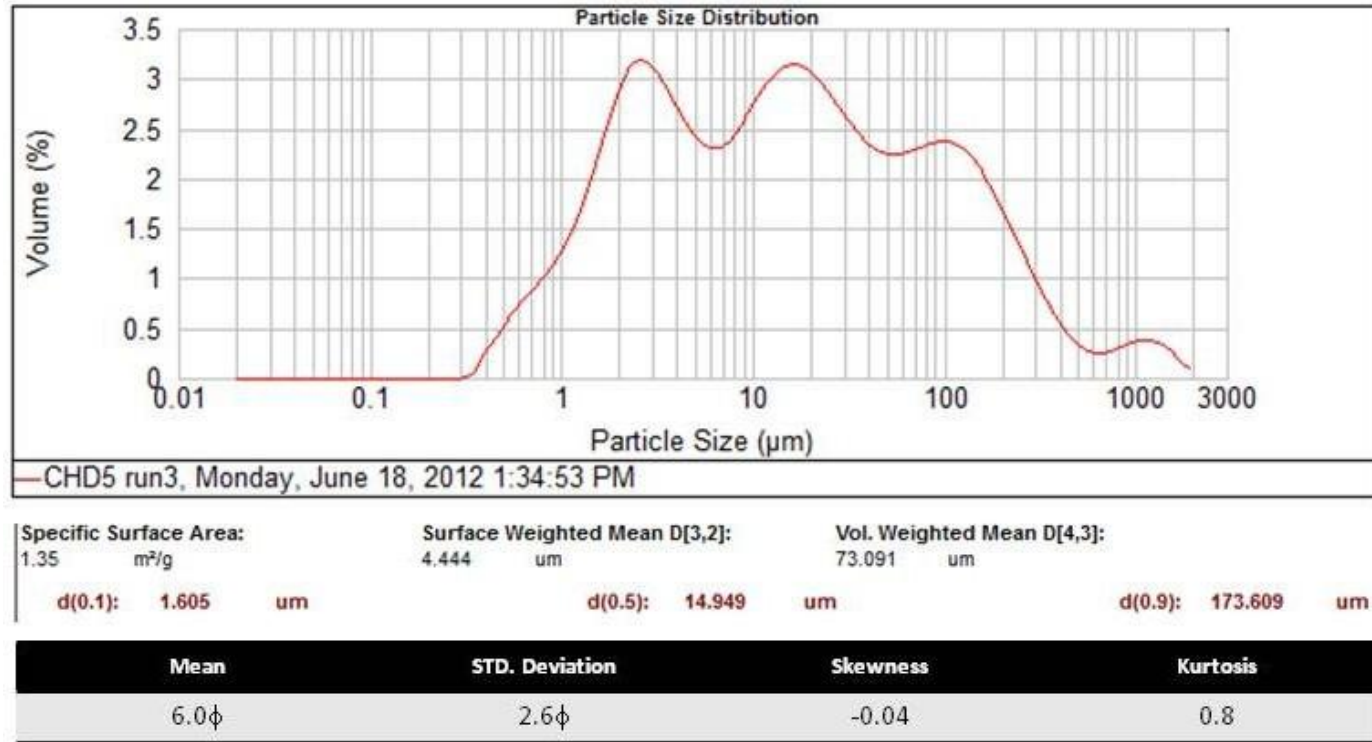


Figure A15: Plot of particle size ( $\mu\text{m}$ ) vs. volume percent (vol. %) and calculated statistical parameters for Sample CHD5.

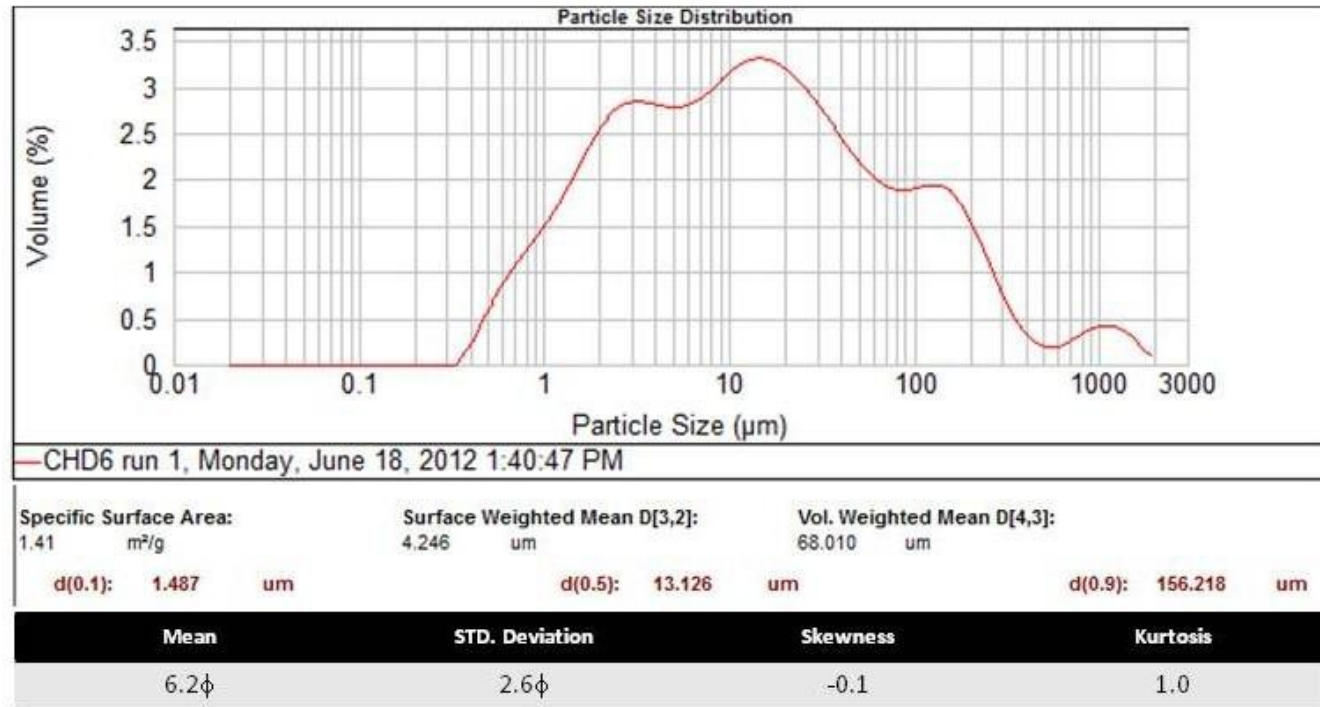


Figure A16: Plot of particle size ( $\mu\text{m}$ ) vs. volume percent (vol. %) and calculated statistical parameters for Sample CHD6.

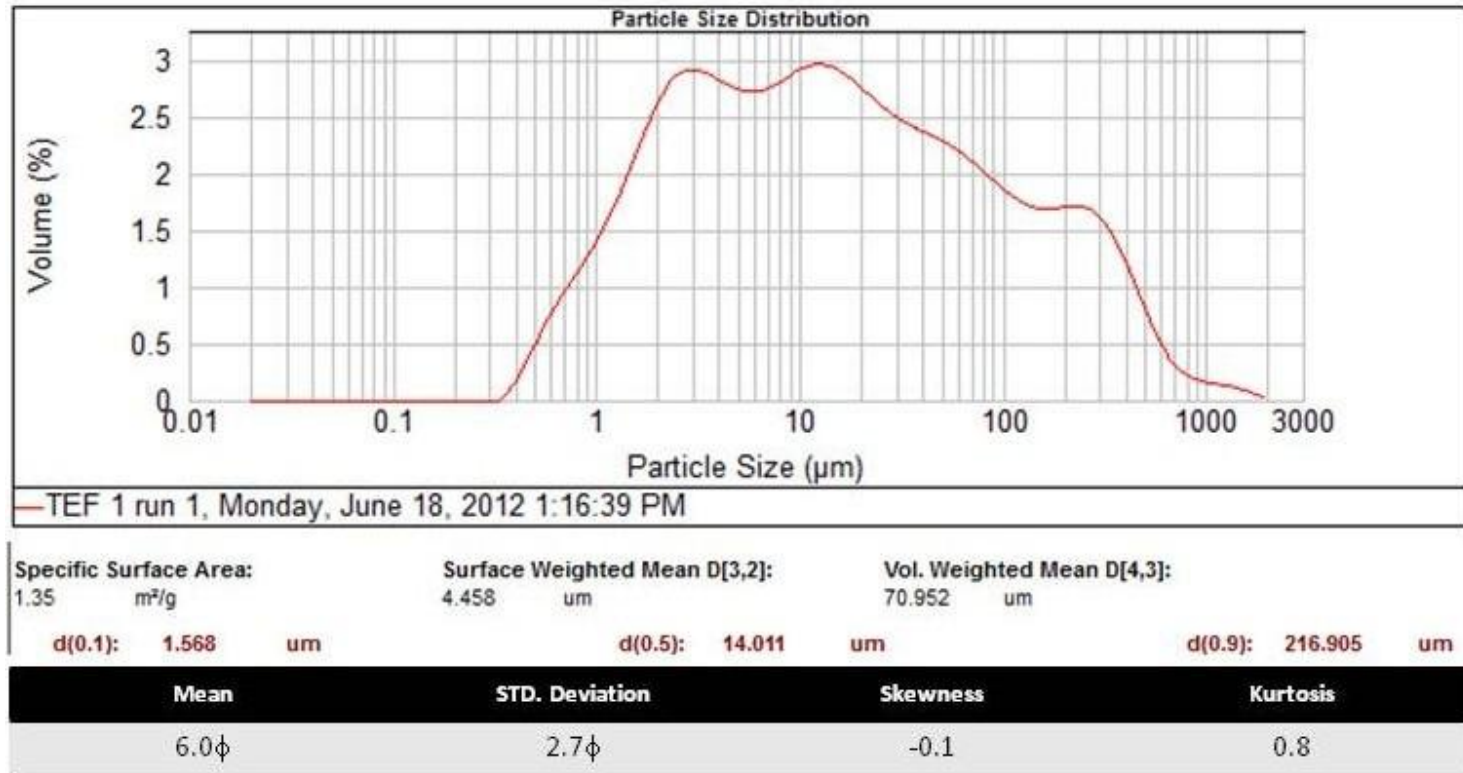


Figure A17: Plot of particle size ( $\mu\text{m}$ ) vs. volume percent (vol. %) and calculated statistical parameters for Sample TEF1.

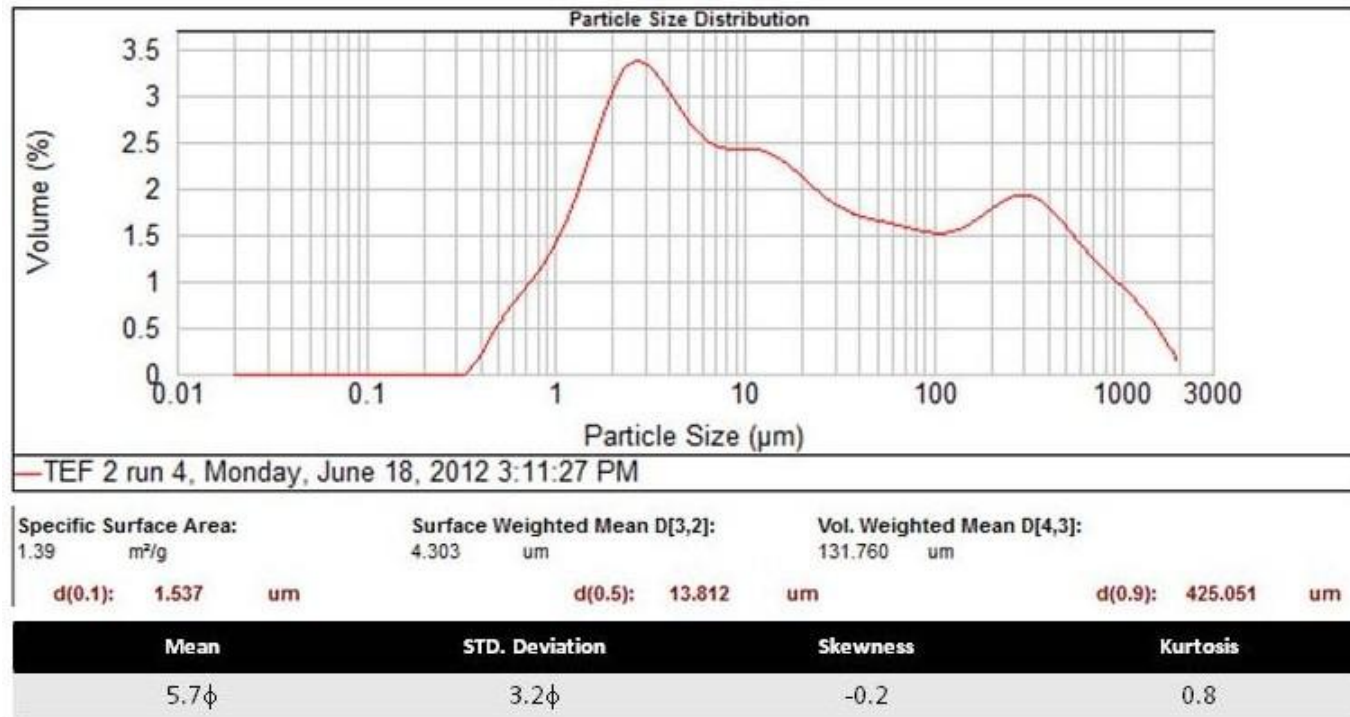


Figure A18: Plot of particle size ( $\mu\text{m}$ ) vs. volume percent (vol. %) and calculated statistical parameters for Sample TEF 2.

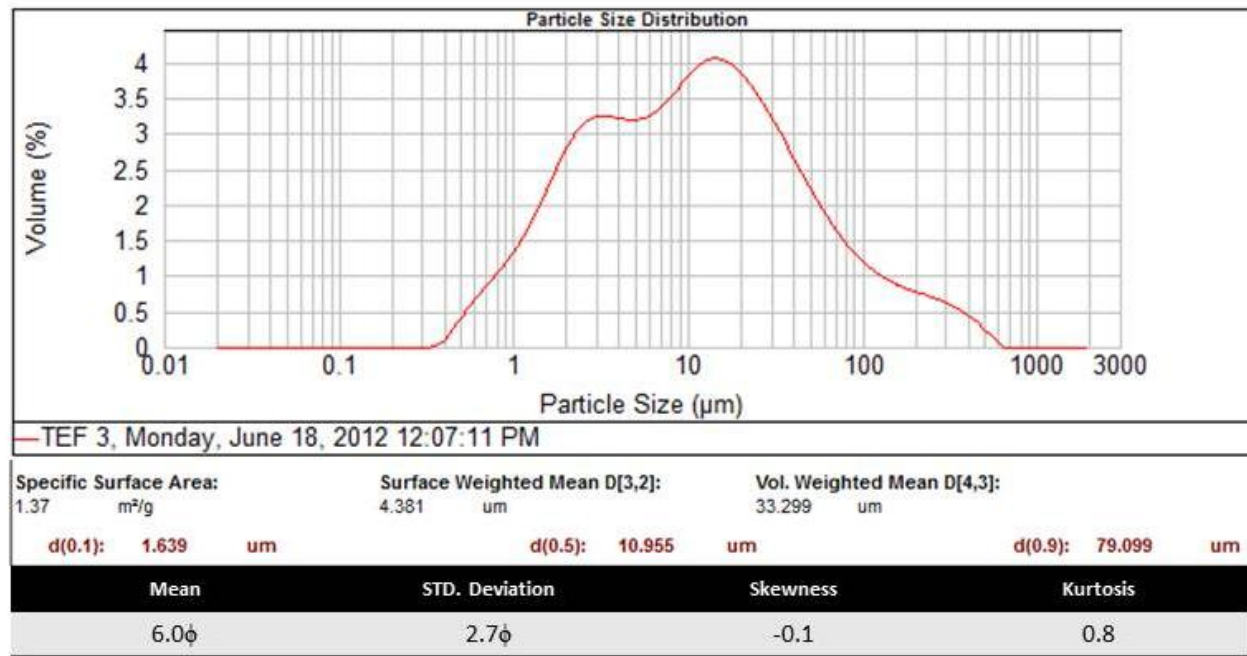


Figure A19: Plot of particle size ( $\mu\text{m}$ ) vs. volume percent (vol. %) and calculated statistical parameters for Sample TEF 3.

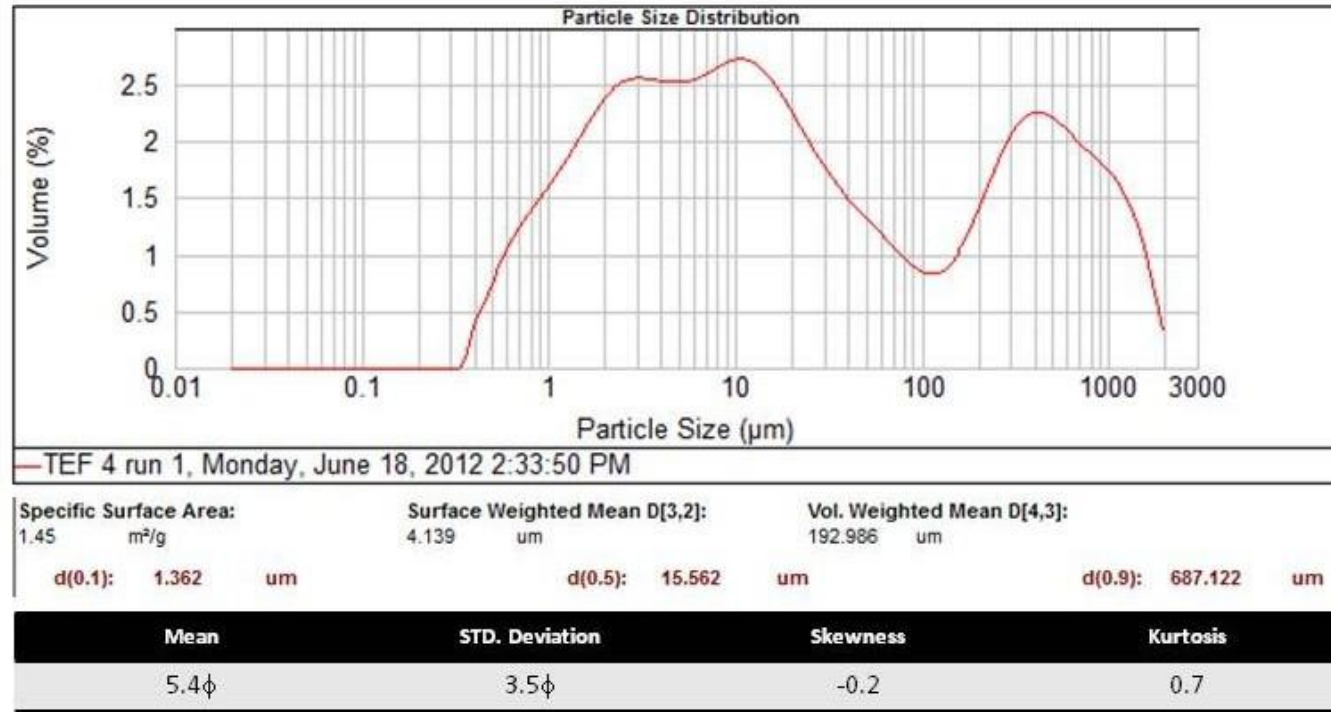


Figure A20: Plot of particle size ( $\mu\text{m}$ ) vs. volume percent (vol. %) and calculated statistical parameters for Sample TEF4.